

FLUMINENSE FEDERAL UNIVERSITY
INSTITUTE OF PHYSICS
GRADUATE PROGRAM IN PHYSICS

Renan Lira Nunes

The cumulant Green's functions method for the Hubbard model

Niterói-RJ-Brazil

2022

RENAN LIRA NUNES

THE CUMULANT GREEN'S FUNCTIONS METHOD FOR THE HUBBARD MODEL

PhD thesis presented to the Graduate Program
in Physics at the Institute of Physics of the Fluminense Federal University as a partial requirement for obtaining the PhD in Physics.

Advisor: Prof. Dr. MARCOS SERGIO FIGUEIRA DA SILVA

Co-advisor: Prof. Dr. JERESON SILVA-VALENCIA

Niterói-RJ-Brazil

2022

Ficha catalográfica automática - SDC/BIF
Gerada com informações fornecidas pelo autor

N972t Nunes, Renan Lira
The cumulant Green's functions method for the Hubbard model
/ Renan Lira Nunes ; Marcos Sergio Figueira da Silva,
orientador ; Jereson Silva-Valencia, coorientador. Niterói,
2022.
76 p. : il.

Tese (doutorado)-Universidade Federal Fluminense, Niterói,
2022.

DOI: <http://dx.doi.org/10.22409/PPGF.2022.d.14425938739>

1. Modelo de Hubbard. 2. Função de Green. 3. Transição
de fase quântica. 4. Diagrama de fase. 5. Produção
intelectual. I. Silva, Marcos Sergio Figueira da, orientador.
II. Silva-Valencia, Jereson, coorientador. III. Universidade
Federal Fluminense. Instituto de Física. IV. Título.

CDD -



INSTITUTO DE FÍSICA
Universidade Federal Fluminense
CURSO DE PÓS-GRADUAÇÃO EM FÍSICA
RUA GAL MILTON TAVARES DE SOUZA, SN
24210-346 – NITERÓI - RIO DE JANEIRO
TEL: (21)2629-5878 - FAX: 2629-5887
E-MAIL: cpg@ if.uff.br

Ata dos trabalhos finais da Comissão Examinadora da tese de doutorado apresentada por **Renan Lira Nunes**. No trigésimo primeiro dia do mês de maio de dois mil e vinte e dois, às quatorze horas, reuniram-se de forma remota, os membros da Comissão Examinadora constituída pelos professores doutores Marcos Sergio Figueira da Silva(IF/UFF), David Möckli (UFRGS), Evandro Vidor Lins de Mello (IF/UFF), Jereson Silva Valencia (UNAL), Maria Carolina de Oliveira Aguiar (UFMG) e Pedro Paulo de Mello Venezuela (IF/UFF); sob a presidência do primeiro, para prova pública de apresentação de tese de doutorado intitulada **“THE CUMULANT GREEN’S FUNCTIONS METHOD FOR THE HUBBARD MODEL”**, tendo em vista as exigências do Regulamento Específico do curso de Física relacionadas com a conclusão do Doutorado em Física pela Universidade Federal Fluminense. A tese foi elaborada sob a orientação do professor Marcos Sergio Figueira da Silva e coorientação do professor Jereson Silva Valencia. Após a exposição do trabalho, o aluno respondeu às questões formuladas pelos integrantes da Comissão Examinadora, que apresentou parecer no sentido de aprová-lo. Para constar, foi lavrada a presente ata, que vai assinada pelos membros da Comissão Examinadora e pelo doutorando.

Niterói, trinta e um de maio de dois mil e vinte e dois.

Dr. Marcos Sergio Figueira da Silva

Marcos Sergio Figueira da Silva

Dr. David Möckli

David Möckli

Dr. Evandro Vidor Lins de Mello

Evandro V. L. Mello

Dr. Jereson Silva Valencia

Jereson Silva Valencia

Dr. Maria Carolina de Oliveira Aguiar

Maria Carolina de O. Aguiar

Dr. Pedro Paulo de Mello Venezuela

Pedro Paulo de Mello Venezuela

Renan Lira Nunes

Renan Lira Nunes

This work is dedicated to my wife
Jeanne Rangel de Castro Nunes.

Acknowledgements

To God, for having guided me in all steps of the walk up here;

To my mother Neide de Brito Lira, who always dreamed of seeing me at a university, for providing the necessary infrastructure for this to happen and for always believing that I could do it;

To my wife Jeanne Rangel de Castro Nunes, for providing an environment of study and work free of worries and tasks whenever necessary, in addition to helping me directly in solving problems sometimes and always comforting me in difficult times;

To my friends, especially Renan Bento and Romulo Martins, for their companionship during hours of study and fun, making university life more pleasant;

To professor Marcos Sergio Figueira da Silva, for his advising during my PhD;

To professor Jereson Silva-Valencia from Universidad Nacional de Colombia, for his co-advising during my PhD and for assisting in developing the exact diagonalization code that is used in this work;

To all other professors at UFF and other institutions, for my academic education.

Abstract

We study the single-band Hubbard model under the action of an external magnetic field using the cumulant Green's functions method [CGFM]. The starting point of the method is to diagonalize a cluster containing N correlated sites ("seed") and employ the cumulants calculated from the cluster solution to obtain the full Green's functions for the lattice. All calculations are done directly, and no self-consistent process is needed. We benchmark the one-dimensional results for the gap, the ground-state energy, and the double occupancy as functions of the electronic correlation U at half-filling obtained from the CGFM against the corresponding exact results of the thermodynamic Bethe ansatz and the quantum transfer matrix methods. The results for the CGFM tend systematically to the exact one as the cluster size increases. The particle-hole symmetry of the density of states is fulfilled. The method can be applied to any parameter space for one, two, or three-dimensional Hubbard Hamiltonians and can also be extended to other strongly correlated models, like the Anderson Hamiltonian, the $t-J$, Kondo, and Coqblin-Schrieffer models.

We also calculate the effects of positive magnetic fields in the occupation numbers, and identify a finite cluster effect (Phase VI) characterized by a partially filled band and negative magnetization ($n_{up} < n_{down}$). This phase survives for clusters containing up to $N = 8$ sites but tends to disappear as the size of the cluster increases. We calculate the phase diagram, including the new cluster phase, using the magnetic field and chemical potential as parameters for $N = 7$ and $N = 8$. We include a simple application to spintronics, where we used the clusters as correlated quantum dots to realize a single-electron transistor when connected to Hubbard leads and calculate the conductance of the transistor.

Keywords: Hubbard model. Green's functions. Cumulant expansion. Mott insulator. Quantum phase transition. Phase diagram.

Resumo

Estudamos o modelo de Hubbard de banda única sob a ação de um campo magnético externo usando o método das funções de Green cumulantes [CGFM]. O ponto de partida do método é diagonalizar um *cluster* contendo N sítios correlacionados (“semente”) e empregar os cumulantes calculados a partir da solução do *cluster* para obter as funções de Green completas para a rede. Todos os cálculos são feitos diretamente, e nenhum processo auto-consistente é necessário. Nós comparamos os resultados unidimensionais para o *gap*, a energia do estado fundamental e a ocupação dupla como funções da correlação eletrônica U em metade do preenchimento obtidos a partir do CGFM com os resultados exatos correspondentes do ansatz de Bethe termodinâmico e da matriz de transferência quântica. Os resultados para o CGFM tendem sistematicamente para o exato à medida que o tamanho do *cluster* aumenta. A simetria partícula-buraco da densidade de estados é satisfeita. O método pode ser aplicado a qualquer espaço de parâmetros para Hamiltonianos de Hubbard uni, bi ou tridimensionais e também pode ser estendido para outros modelos fortemente correlacionados, como o Hamiltoniano de Anderson, os modelos $t - J$, Kondo e Coqblin-Schrieffer.

Também calculamos os efeitos de campos magnéticos positivos nos números de ocupação e identificamos um efeito de *cluster* finito (Fase VI) caracterizado por uma banda parcialmente preenchida e magnetização negativa ($n_{up} < n_{down}$). Esta fase sobrevive para *clusters* contendo até $N = 8$ sítios, mas tende a desaparecer à medida que o tamanho do *cluster* aumenta. Calculamos o diagrama de fases, incluindo a nova fase de *cluster*, usando o campo magnético e o potencial químico como parâmetros para $N = 7$ e $N = 8$. Incluímos uma aplicação simples para spintrônica, onde usamos os *clusters* como pontos quânticos correlacionados para realizar um transistor de um único elétron quando conectado a terminais Hubbard e calculamos a condutância do transistor.

Palavras-chave: Modelo de Hubbard. Funções de Green. Expansão em cumulantes. Isolante de Mott. Transição de fase quântica. Diagrama de fase.

List of Figures

2.1	Density of states for different values of energy ϵ_0 and electronic correlation U	10
2.2	Occupation numbers as functions of the chemical potential μ	11
2.3	Limiting cases for the density of states for different values of chemical potential μ	12
2.4	Ground-state phase diagram at zero temperature in h vs. μ coordinates for the noninteracting case. In terms of the densities and magnetization the four phases are characterized by I: $n = m = 0$; II: $n_{down} = 0, 0 < n_{up} < 1$; III: $n_{down} = 0, n_{up} = 1$; IV: $0 < n < 1, 0 \leq m \leq 1/2$	15
2.5	Results for the Bethe ansatz in the half-filled case for the a) Single-particle gap and the b) Ground-state energy as functions of the correlation U	17
2.6	Results for the Bethe ansatz in the half-filled case for the double occupation number as function of the correlation U	18
2.7	Ground-state phase diagram at zero temperature in h vs. μ coordinates for the interacting case for $u = 1$. In terms of the densities and magnetization the five phases are characterized by I: $n = m = 0$; II: $n_{down} = 0, 0 < n_{up} < 1$; III: $n_{down} = 0, n_{up} = 1$; IV: $0 < n < 1, 0 \leq m \leq 1/2$; V: $n = 1, m \geq 0$	20
3.1	Diagrams that contribute to the one-particle Green's function for near neighbour hopping in a hypercubic lattice from zeroth ($n = 0$) up to fourth ($n = 4$) order, taken from reference [1].	23
3.2	Schematic of the type of the clusters employed as a "seed" to generate cumulants M and from them the Dyson equation to calculate the lattice Green's functions G of the method.	24
3.3	Flowchart of the steps of the CGFM.	26
3.4	Density of states ρ as a function of the frequency $\omega - \mu$ for the half-filling limit, $\epsilon_0 = -U/2, \mu = 0$, for the CGFM for some representative values of ϵ_0 and U using the monomer.	35
3.5	Density of states ρ as a function of the frequency $\omega - \mu$ for the half-filling limit, $\epsilon_0 = -U/2, \mu = 0$, for the CGFM for some representative values of ϵ_0 and U using the dimer.	38
4.1	Numerical value of the residues $r_{i,up}$ of the total atomic GF $g_{up}^{at} = g_{11} + g_{13} + g_{31} + g_{33}$ as functions of the transition energies $u_{i,up}$ for the CGFM for some representative values of $N = 2, 3, 4, 5, 6, 7$	39
4.2	Density of states ρ as a function of the frequency $\omega - \mu$ for the half-filling limit, $\epsilon_0 = -U/2, \mu = 0$, for the CGFM for some representative values of $N = 2, 7$	40

4.3	Single-particle gap Δ as a function of the correlation energy U for the BA, the HF approximation, the VCA [2], and the CGFM for some representative values of $N = 2, 6, 7, 9$	41
4.4	Single-particle gap Δ as a function of the inverse cluster size $1/N$ for the CGFM for a) Even N (2, 4, 6, 8) and b) Odd N (3, 5, 7, 9) for several values of electronic correlation U . The dotted lines represent the quadratic regression of the calculated data points and converge to the exact BA results represented by brown points on the vertical axis.	42
4.5	Double occupation number n_d as a function of the correlation U for the interpolative “exact” result [3], the HF approximation, and the CGFM for some representative values of $N = 2, 5, 6, 7$	43
4.6	Ground-state energy for the lattice E_g as a function of the correlation U for the BA, the HF approximation, and the CGFM for some representative values of $N = 2, 4, 5, 6, 7$	44
4.7	Occupation numbers as functions of the chemical potential μ for the CGFM with $U = 4D$, $N = 7$, magnetic field $h = 0$, and $T = 0.0001D$	45
4.8	Occupation numbers as functions of the chemical potential μ for the CGFM with $U = 4D$, $N = 7$, magnetic field $h = 0$, and $T = 0.1D$	46
4.9	Occupation numbers as functions of the chemical potential μ for the CGFM with $U = 4D$; magnetic field $h = 0.10D/\mu_B$; and a) $N = 5$, b) $N = 6$, c) $N = 7$, d) $N = 8$	47
4.10	Occupation numbers as functions of the chemical potential μ for the CGFM with $U = 4D$; $N = 7$; and magnetic fields a) $h = 0.198D/\mu_B$, b) $h = 0.395D/\mu_B$, c) $h = 0.692D/\mu_B$, d) $h = 0.890D/\mu_B$	48
4.11	Ground-state phase diagram at low temperature in h vs. μ coordinates for the CGFM for $U = 4D$ and $N = 7$, and at zero temperature for the BA for $u = 1$. In terms of the densities and magnetization the six phases are characterized by I: $n = m = 0$; II: $n_{down} = 0, 0 < n_{up} < 1$; III: $n_{down} = 0, n_{up} = 1$; IV: $0 < n < 1, 0 \leq m \leq 1/2$; V: $n = 1, m \geq 0$; VI: $0 < n < 1, -1/2 \leq m \leq 0$	49
4.12	Ground-state phase diagram at low temperature in h vs. μ coordinates for the CGFM for $U = 4D$ and $N = 8$, and at zero temperature for the BA for $u = 1$. In terms of the densities and magnetization the six phases are characterized by I: $n = m = 0$; II: $n_{down} = 0, 0 < n_{up} < 1$; III: $n_{down} = 0, n_{up} = 1$; IV: $0 < n < 1, 0 \leq m \leq 1/2$; V: $n = 1, m \geq 0$; VI: $0 < n < 1, -1/2 \leq m \leq 0$	50
4.13	Schematic view of a correlated 3-site quantum dot immersed in left (L) and right (R) correlated 3-site Hubbard rectangular conduction bands.	51
4.14	Electrical conductance G/G_0 vs. chemical potential μ	52

List of Tables

3.1	Representation of the possible transitions present in the Hubbard Hamiltonian.	25
3.2	Execution times and RAM usage by the code (time / RAM) when run in the workstation mentioned in section 3.2.	33
3.3	Exact solution of the Hubbard model for the monomer.	34
3.4	Energy differences of the possible transitions of the Hubbard monomer.	35
3.5	Exact diagonalization of the Hubbard Hamiltonian for the dimer.	37
4.1	Number of correlated sites N , atomic cluster ground-state energy per site GSE/ N , total cluster spin in the z direction S_z , and charge Q of the atomic cluster employed in the calculations at half-filling. For odd N , the GSE/ N is two-fold degenerated, corresponding to two spin orientations $\pm 1/2$	40
4.2	Spin in the z direction S_z , and charge Q of the atomic cluster ground-state in different regions as the chemical potential μ increases.	45
A.1	Energy differences of the possible transitions of the Hubbard dimer.	61

Contents

Acknowledgements	ix
Abstract	x
Resumo	xi
List of figures	xii
List of tables	xiv
1 Introduction	1
2 The Hubbard model	4
2.1 The Green's functions of Zubarev and the atomic limit	5
2.2 The Hubbard I approximation	7
2.3 The analytical solution for the one-dimensional Hubbard model	13
2.3.1 The noninteracting case - a point of reference	13
2.3.2 The interacting case - the Bethe ansatz [BA] solution	16
3 The cumulant Green's functions method [CGFM]	22
3.1 The method	23
3.2 The numerical code	30
3.3 Using the Hubbard monomer as a "seed"	34
3.4 Using the Hubbard dimer as a "seed"	35
4 Results and discussion for larger clusters	39
4.1 Zero magnetic field	39
4.2 Nonzero magnetic field	47
4.3 A simple application	51
5 Conclusions and Perspectives	53
References	55
Appendix A Atomic Green's functions residues and transition energies for the dimer	59

Chapter 1

Introduction

The Hubbard model was proposed independently in 1963 by Gutzwiller [4], Kanamori [5], and Hubbard [6]. Hubbard worked hard to understand the model and published a series of six papers in the period [1963 – 1967] [6–11], where he developed different approaches for solving it. The Hubbard Hamiltonian is the simplest interacting particle model in a lattice: it extends the tight-binding model, accounting for the electron-electron correlation U between electrons on the same site, neglecting the effects of non-local correlations, multiple orbitals, or higher-order hoppings. It was originally developed to describe the properties of narrow partially filled d band in transition metals. It has been shown that the model describes the relevant collective characteristics of these materials, namely itinerant magnetism and metal-insulating transition. For a pertinent review, see the references [3, 12, 13].

The one-dimensional [1D] Hubbard model was solved exactly in a seminal paper by E. H. Lieb and F. Y. Wu [14], employing the technique of the Bethe ansatz [15]. They showed that it could reduce the Hamiltonian spectral problem to a set of algebraic equations. They calculated analytically the ground-state energy demonstrating that, at half-filling, the model goes through a Mott metal-insulator transition [8, 16] at temperature $T = 0$ and local critical electron correlation $U_c = 0$ [17]. A complete and didactic discussion of the development of the subject can be found in reference [3].

The following fundamental advance in the Bethe ansatz formulation was attained by Takahashi, who employed a particular classification of the Lieb-Wu solutions in terms of a “string hypothesis” [3]. He derived an infinite set of non-linear integral equations at finite temperatures and calculated the Gibbs free energy [18–20]. Those integral equations are known as the thermodynamic Bethe ansatz [TBA] or TBA equations. They are fundamental to the study of low-temperature properties of the model but challenging to implement numerically. One step further was attained by employing a different route than TBA equations, by the development of the quantum transfer matrix [QTM] method [21]. The calculation of the properties of the 1D Hubbard model has been addressed in recent years employing different approaches associated with TBA or QTM methods [22–25].

Another class of approximations, useful in some circumstances, that approximate the many-body wave function as an antisymmetric function of one-body orbitals includes the mean-field Hartree-Fock [HF] approximation, the random phase approximation [RPA] [26], and the configurational interaction

technique [CI] [27]. The latter is based on a linear combination of Hartree-Fock wave functions to restore some broken symmetries of the mean-field approach and recover some features of the exact 1D Bethe ansatz solution [27]. These approximations have several drawbacks, either limiting the effect of quantum many-body correlations, as in the HF approximation, or converging very slowly, as in CI applications.

Cluster methods, which approximate the physics of the infinite system by solving the problem for a corresponding finite cluster, are promising as the interaction part can be treated numerically exact. One type of cluster methods is the direct cluster approach, which uses exact diagonalization to study the effect of short-range correlations for a small isolated cluster. However, phase transitions and long-range order can not occur in a system of finite size. Another type of cluster methods includes the dynamical mean-field theory [DMFT] [28], where the lattice model is mapped onto an impurity model consisting of a correlated site coupled to an infinite number of uncorrelated “bath” sites. The bath must be determined self-consistently. The DMFT directly works in the thermodynamic limit and is able to describe phases with long-range order. However, it fails to incorporate the effects of short-range correlations. This has been the reason for the development of cluster extensions of the DMFT [C-DMFT] [29] that replaces the correlated impurity site by a finite cluster to obtain both short-range correlations and long-range order.

Beyond mean-field approximations, Quantum Monte Carlo [QMC] is a way to directly study the many-body problem [30–32]. The QMC algorithm for clusters is based on the Hirsch and Fye algorithm which was developed to simulate the Anderson impurity problem [33] and was later generalized to solve the C-DMFT [34]. A major advantage of QMC is that there is no restriction on the form of the wave function, hence any insight, as regards the nature of the many-body correlations, can be built into the wave function and tested. Other advantages include the ability to treat relatively large clusters, and that it is numerically exact with small and controllable sources of systematic and statistical error. Its disadvantages include an unpredictable numerical minus sign problem, difficulties to reach low temperatures due to the processing of a large number of Matsubara frequencies that must be considered in the imaginary axis, difficulties in calculating real-frequency results, and the numerical expense of the approach [30–32].

The Hubbard model has been the subject of a tremendous revival of interest in the eighties after the discovery of high temperature (high- T_c) cuprate superconductors and has been considered the most promising model to explain strong correlations. In recent years, numerical simulations on the two-dimensional [2D] Hubbard model show regions on the parameter space that exhibits d -wave superconductivity, antiferromagnetic correlations, stripes, pseudogaps, Fermi liquid, and bad metallic behaviour [13]. However, the connection of these phases with real high- T_c superconductors is not direct.

A new interest in Hubbard model physics came from the fast and efficient experiments of ultracold atoms in optical lattices after achieving the Bose-Einstein condensation. This research area set an ideal platform to verify and explore new physics associated with correlated electronic systems [35–37]. The confinement of fermionic atoms in optical lattices allows the observation of the Mott metal-insulator transition, antiferromagnetic correlations, and spin-charge separation in one-dimensional systems with hundreds of lattice sites [38–42]. Recently, the level of control and flexibility (geometry-lattice) was improved in an eight-site Fermi-Hubbard chain near half-filling achieved with lithium-6 atoms in an optical tweezer array [43], which provides another motivation for the present study.

The present work belongs to a broad class of exact diagonalization [ED] methods that generally start from the diagonalization of a finite number of lattice sites that constitutes a cluster and employs an embedding process to reconstruct the total Hamiltonian [44]. One example of this technique is the variational cluster approach [VCA] [2, 45]. Here, we developed the cumulant Green's functions method [CGFM] for the single-band Hubbard model in the presence of an external magnetic field and published the resulting work in the arXiv repository [46]. The general formalism of the cumulant expansion, as outlined here, has been previously applied to treat the impurity Anderson model [47] and a detailed review can be found in the arXiv repository [48]. Still, it can be generalized to the Anderson or Hubbard lattice models and variants like the $t - J$, Kondo, and Coqblin-Schrieffer models.

This work can be divided into two parts. The first part (chapter 2) is comprised of the study of methods currently used to treat the Hubbard Hamiltonian. The second part (chapters 3 and 4) is comprised of the development of a novel alternative methodology to these methods, the CGFM, and the results obtained from it. Therefore, this work has the following structure:

- In chapter 2, the Hamiltonian of the model is introduced in the presence of an external magnetic field, and a brief discussion of its physical meaning is made. In the sections contained in this chapter, several pre-established methods to treat the model will be presented and discussed, such as the atomic limit, the Hubbard I approximation, the analytical solution for the 1D half-filled case (the Bethe ansatz solution), and the 1D thermodynamic Bethe ansatz [TBA] solution outside of the half-filled case. The 1D results will be used as a benchmark for the CGFM;
- In chapter 3, the core of this thesis, we introduce the basic ideas of the cumulant Green's functions method in four steps: 1. Choice of a cluster of correlated sites to solve exactly employing exact diagonalization [ED] methods; 2. Using the Lehmann representation, we calculate all atomic Green's functions associated with the possible transitions of the Hubbard model; 3. Employing these atomic Green's functions, we obtain the atomic cumulants that will be used as an approximation to 4. Calculate the Green's functions for the lattice. From the Green's functions for the lattice, the density of states, the single-particle gap, the occupation numbers, the ground-state energy, and the ground-state phase diagram will be calculated;
- In chapter 4, we present the results for the method. In section 4.1, we benchmark the single-particle gap, the double occupancy, and the ground-state energy as functions of the electronic correlation obtained from the CGFM against the Bethe ansatz [BA], the Hartree-Fock [HF] approximation, and the variational cluster approach [VCA] and also show the density of states and the occupation numbers at zero magnetic field. In section 4.2, we present a discussion of the effect of the magnetic field on the occupation numbers and present the phase diagram in magnetic field vs. chemical potential coordinates. In section 4.3, we present a simple application of the method to spintronics, where we use the clusters as correlated quantum dots to realize a single-electron transistor when connected to Hubbard leads and calculate the conductance of the system;
- In chapter 5, we discuss the conclusions and perspectives of the work.

Chapter 2

The Hubbard model

The single-band Hubbard model [6] is the simplest many-body Hamiltonian that allows a relevant description of two opposite trends in systems where electronic correlations are essential. The first trend is the electron delocalization that favours metallic behaviour, accounted for by the kinetic energy that describes electrons moving from site to site in the crystal lattice. The second trend is the localization of electrons in atomic sites, favouring the Mott transition [49] and magnetic ordering, accounted for by the local electronic correlation. The single-band Hubbard model in the presence of an arbitrary magnetic field is given by

$$H = H_0 + H_1, \quad (2.1)$$

where H_0 represents the unperturbed local terms

$$H_0 = \sum_i [\epsilon_0(n_{i\uparrow} + n_{i\downarrow}) - h_i m_i] + \frac{U}{2} \sum_{i\sigma} n_{i\sigma} n_{i\bar{\sigma}}, \quad (2.2)$$

and the perturbation H_1 is the kinetic energy

$$H_1 = - \sum_{i \neq j, \sigma} t_{ij} c_{i\sigma}^\dagger c_{j\sigma}. \quad (2.3)$$

The operators $c_{i\sigma}^\dagger$ and $c_{i\sigma}$ represent the creation and annihilation of electrons, respectively, and $n_{i\sigma} = c_{i\sigma}^\dagger c_{i\sigma}$ is the electron number operator. The first term of the unperturbed local Hamiltonian, H_0 , represents the local energy E_0 of the electrons subtracted from the chemical potential μ , ($\epsilon_0 = E_0 - \mu$), here assumed site-independent. The second term is the magnetization defined by $m_i = n_{i\uparrow} - n_{i\downarrow}$, with h_i being the site spin-dependent external magnetic field. The last term represents the local electronic correlation term, characterized by the parameter U , which favors the localization of electrons on the same site. The correlation energy is responsible for the Mott transition exhibited by this Hamiltonian. In the cumulant expansion of the Hubbard model [1] the kinetic energy term, H_1 , is considered the perturbation, where $(-t_{ij})$ corresponds to the electron transfer integral between the i and j sites of the crystal lattice. In the single-band Hubbard model, each site has only one orbital that can be occupied by no electron ($|0\rangle$), a spin up electron ($|\uparrow\rangle$), or a spin down electron ($|\downarrow\rangle$), or by two electrons of opposing spin ($|\uparrow\downarrow\rangle = |d\rangle$).

2.1 The Green's functions of Zubarev and the atomic limit

The method that will be used in this work is based on the Green's functions technique described by Zubarev [50]. The definitions and equations for this technique is introduced below, and the density of states in the atomic limit is discussed.

Let X be any operator. Then

$$\langle X \rangle = Z^{-1} \text{tr} \left[X e^{-\beta(H-\mu N)} \right], \quad (2.4)$$

where $Z = \text{tr} [e^{-\beta(H-\mu N)}]$, H is the Hamiltonian, N is the total number operator, $\beta = \frac{1}{k_B T}$, k_B is the Boltzmann constant, T is the absolute temperature and μ is the chemical potential of the electrons.

Now let $A(t) = e^{iHt} A(0) e^{-iHt}$ (in units where $\hbar = 1$) and $B(t')$ be two operators. The retarded (+) and advanced (-) Green's functions can be defined by

$$\langle\langle A(t); B(t') \rangle\rangle^{(\pm)} = \mp i \theta [\pm(t-t')] \langle [A(t), B(t')]_{\eta} \rangle, \quad (2.5)$$

where $[A, B]_{\eta} = AB - \eta BA$, $\eta = \pm 1$ (depending if the operators are fermionic or bosonic) and $\theta(x)$ is the step function $\theta(x) = 1$ if $x > 0$, 0 otherwise. These Green's functions satisfy the Heisenberg equation of motion [EOM]

$$i \frac{d}{dt} \langle\langle A(t); B(t') \rangle\rangle^{(\pm)} = \delta(t-t') \langle [A(t), B(t')]_{\eta} \rangle + \langle\langle [A(t), H]; B(t') \rangle\rangle^{(\pm)}. \quad (2.6)$$

Since $\langle\langle A(t); B(t') \rangle\rangle^{(\pm)}$ are functions of $t-t'$ only, the Fourier transform

$$\langle\langle A; B \rangle\rangle_E^{(\pm)} = \int_{-\infty}^{\infty} \langle\langle A(t); B(0) \rangle\rangle^{(\pm)} e^{iEt} dt \quad (2.7)$$

can be defined for real E . For the case of the retarded function (+), the integral also converges to complex E since $\text{Im}\{E\} > 0$, then $\langle\langle A; B \rangle\rangle_E^{(+)}$ is a regular function of E in the upper half of the complex plane in E . Similarly, $\langle\langle A; B \rangle\rangle_E^{(-)}$ is a regular function in the lower half of the complex plane in E . So, one can define

$$\langle\langle A; B \rangle\rangle_E = \begin{cases} \langle\langle A; B \rangle\rangle_E^{(+)} & \text{if } \text{Im}\{E\} > 0 \\ \langle\langle A; B \rangle\rangle_E^{(-)} & \text{if } \text{Im}\{E\} < 0 \end{cases}, \quad (2.8)$$

which will be a regular function throughout the complex plane in E with the exception of the real axis.

From (2.6) it can be shown that $\langle\langle A; B \rangle\rangle_E$ satisfies

$$E \langle\langle A; B \rangle\rangle_E = \langle [A, B]_{\eta} \rangle + \langle\langle [A, H]; B \rangle\rangle_E, \quad (2.9)$$

which is the expression that will be used to calculate the Green's functions throughout this work.

Let us go back to the Hubbard Hamiltonian given in equation (2.1) at zero magnetic field. At the atomic limit there is no electron hopping between sites, so $t_{ij} = 0$. Then:

$$H = \sum_{i\sigma} \epsilon_0 c_{i\sigma}^{\dagger} c_{i\sigma} + \frac{U}{2} \sum_{i\sigma} n_{i\sigma} n_{i\bar{\sigma}}. \quad (2.10)$$

Using the equations of motion for the Green's functions of Zubarev [50], one gets for the single-particle GF,

$$\omega \langle\langle A, B \rangle\rangle_{\omega} = \langle [A, B]_{+} \rangle + \langle\langle [A, H]_{-}, B \rangle\rangle_{\omega}. \quad (2.11)$$

If $A = c_{i\sigma}$ and $B = c_{j\sigma}^\dagger$, it follows that

$$\omega G_{ij}^\sigma(\omega) = \omega \left\langle \left\langle c_{i\sigma}; c_{j\sigma}^\dagger \right\rangle \right\rangle_\omega = \left\langle \left[c_{i\sigma}, c_{j\sigma}^\dagger \right]_+ \right\rangle + \left\langle \left[c_{i\sigma}, H \right]_-; c_{j\sigma}^\dagger \right\rangle_\omega. \quad (2.12)$$

Using fermionic commutation ($[A, B]_-$) and anti-commutation ($[A, B]_+$) relations and their properties

$$\begin{aligned} [A, BC]_- &= [A, B]_- C + B [A, C]_-, \\ [A, BC]_+ &= [A, B]_+ C - B [A, C]_-, \\ [c_i^\dagger, c_j]_+ &= \delta_{ij}, \\ [c_i^\dagger, c_j^\dagger]_+ &= 0, \\ [c_i, c_j]_+ &= 0, \end{aligned} \quad (2.13)$$

it follows that

$$\omega G_{ij}^\sigma(\omega) = \delta_{ij} + \left\langle \left\langle (\epsilon_0 c_{i\sigma} + U n_{i\bar{\sigma}} c_{i\sigma}); c_{j\sigma}^\dagger \right\rangle \right\rangle_\omega. \quad (2.14)$$

However,

$$\begin{aligned} \left\langle \left\langle (\epsilon_0 c_{i\sigma} + U n_{i\bar{\sigma}} c_{i\sigma}); c_{j\sigma}^\dagger \right\rangle \right\rangle_\omega &= \epsilon_0 \left\langle \left\langle c_{i\sigma}; c_{j\sigma}^\dagger \right\rangle \right\rangle_\omega + U \left\langle \left\langle n_{i\bar{\sigma}} c_{i\sigma}; c_{j\sigma}^\dagger \right\rangle \right\rangle_\omega \\ &= \epsilon_0 G_{ij}^\sigma(\omega) + U \left\langle \left\langle n_{i\bar{\sigma}} c_{i\sigma}; c_{j\sigma}^\dagger \right\rangle \right\rangle_\omega. \end{aligned} \quad (2.15)$$

Then,

$$(\omega - \epsilon_0) G_{ij}^\sigma(\omega) = \delta_{ij} + U \Gamma_{ij}^\sigma(\omega), \quad (2.16)$$

where $\left\langle \left\langle n_{i\bar{\sigma}} c_{i\sigma}; c_{j\sigma}^\dagger \right\rangle \right\rangle_\omega \equiv \Gamma_{ij}^\sigma(\omega)$ is the Gamma function that defines the next hierarchy of Green's functions:

$$\omega \Gamma_{ij}^\sigma(\omega) = \omega \left\langle \left\langle n_{i\bar{\sigma}} c_{i\sigma}; c_{j\sigma}^\dagger \right\rangle \right\rangle_\omega = \left\langle [n_{i\bar{\sigma}} c_{i\sigma}, c_{j\sigma}^\dagger]_+ \right\rangle + \left\langle \left[n_{i\bar{\sigma}} c_{i\sigma}, H \right]_-; c_{j\sigma}^\dagger \right\rangle_\omega. \quad (2.17)$$

Calculating the commutation relations, it follows that:

$$\omega \Gamma_{ij}^\sigma(\omega) = \delta_{ij} \langle n_{i\bar{\sigma}} \rangle + \epsilon_0 \Gamma_{ij}^\sigma(\omega) + U \Gamma_{ij}^\sigma(\omega). \quad (2.18)$$

Then,

$$\omega \Gamma_{ij}^\sigma(\omega) = \delta_{ij} \frac{\langle n_{i\bar{\sigma}} \rangle}{\omega - \epsilon_0 - U}. \quad (2.19)$$

Substituting the Gamma function in the single-particle Green's functions, one obtains

$$G_{ij}^\sigma(\omega) = \delta_{ij} \left\{ \frac{1 - \langle n_{i\bar{\sigma}} \rangle}{\omega - \epsilon_0} + \frac{\langle n_{i\bar{\sigma}} \rangle}{\omega - \epsilon_0 - U} \right\}. \quad (2.20)$$

The density of states

$$\rho_{ij}^\sigma(\omega) = \frac{1}{\pi} \text{Im} \{ G_{ij}^\sigma(\omega) \}, \quad (2.21)$$

using the fact that the Green's functions can be written as

$$G_{ij}^\sigma(\omega) = \delta_{ij} \left\{ \frac{1 - \langle n_{i\bar{\sigma}} \rangle}{(\omega - \epsilon_0) - i\eta} + \frac{\langle n_{i\bar{\sigma}} \rangle}{(\omega - \epsilon_0 - U) - i\eta} \right\}, \quad (2.22)$$

with infinitesimal η , and using the relation

$$\lim_{\eta \rightarrow 0^+} \left(\frac{1}{x \pm i\eta} \right) = P \left(\frac{1}{x} \right) \mp i\pi \delta(x), \quad (2.23)$$

where P denotes the Cauchy principal part, becomes

$$\rho_\sigma(\omega) = (1 - \langle n_{i\bar{\sigma}} \rangle) \delta(\omega - \epsilon_0) + \langle n_{i\bar{\sigma}} \rangle \delta(\omega - \epsilon_0 - U). \quad (2.24)$$

This result shows that the atomic limit has two energy levels: ϵ_0 and $\epsilon_0 + U$ containing $1 - \langle n_{i\bar{\sigma}} \rangle$ and $\langle n_{i\bar{\sigma}} \rangle$ electrons, respectively. Thus, if electrons are added to the system, the chemical potential μ remains fixed at ϵ_0 until that energy level is filled. The ground-state becomes full when $1 - \langle n_{i\bar{\sigma}} \rangle = \langle n_{i\bar{\sigma}} \rangle$, that is, the occupation $n = \frac{1}{N} \sum_{\sigma,j=1}^N n_{j,\sigma}$ is equal to $n = 1$. Thereafter, if the total number of electrons in the system continues to be increased, the chemical potential jumps to the double occupancy level $\epsilon_0 + U$, when then the occupation number continues to increase until it reaches $n = 2$.

2.2 The Hubbard I approximation

Hubbard obtained an approximate solution for the Hamiltonian (2.1), known as the Hubbard I approximation, in his first work [6] of a series of six. It became important in the physics of strongly correlated systems, as it was the first approximation to obtain the Mott transition [49] in a consistent way. However, this approach has serious fundamental flaws:

- It does not preserve the particle-hole symmetry, manifested in the non-conservation of the area of the sub-bands at half-filling;
- It overestimates the electronic correlation U : for any value of U a gap opens in the density of states, which leads to a Mott transition at $U = 0$;
- It does not adequately describe the loosely coupled limit, where $U/D \ll 1$ with D being half the bandwidth. That is, it does not describe the character of a renormalized Fermi liquid in this limit.

In this section, we will study the correlation problem in the Hamiltonian (2.1) at zero magnetic field for a finite bandwidth using the same method adopted in the previous section. However, this time, some additional terms appear and will have to be treated approximately. From the equation (2.12) from the previous section, we have that

$$\omega G_{ij}^\sigma(\omega) = \omega \left\langle \left\langle c_{i\sigma}; c_{j\sigma}^\dagger \right\rangle \right\rangle_\omega = \left\langle \left\langle [c_{i\sigma}, c_{j\sigma}^\dagger]_+ \right\rangle \right\rangle + \left\langle \left\langle [c_{i\sigma}, H]_-; c_{j\sigma}^\dagger \right\rangle \right\rangle_\omega. \quad (2.25)$$

Using that

$$[c_{i\sigma}, H]_- = \sum_j t_{ij} c_{j\sigma} + U n_{i\bar{\sigma}} c_{i\sigma}, \quad (2.26)$$

$$[n_{i\sigma}, H]_- = \sum_j t_{ij} (c_{i\sigma}^\dagger c_{j\sigma} - c_{j\sigma}^\dagger c_{i\sigma}), \quad (2.27)$$

the equation for $G_{ij}^\sigma(\omega)$ becomes

$$\omega G_{ij}^\sigma(\omega) = \delta_{ij} + \sum_k t_{ik} G_{kj}^\sigma(\omega) + U \Gamma_{ij}^\sigma(\omega), \quad (2.28)$$

where $\Gamma_{ij}^\sigma(\omega)$ is once again defined by (2.17), but satisfies the equation

$$\begin{aligned} \omega\Gamma_{ij}^\sigma(\omega) &= \delta_{ij} \langle n_{i\bar{\sigma}} \rangle + (\epsilon_0 + U)\Gamma_{ij}^\sigma(\omega) + \\ &+ \sum_{k \neq i} t_{ik} \left\langle \left\langle n_{i\bar{\sigma}} c_{k\sigma}; c_{j\sigma}^\dagger \right\rangle \right\rangle_\omega + \\ &+ \sum_{k \neq i} t_{ik} \left\{ \left\langle \left\langle c_{i\bar{\sigma}}^\dagger c_{k\bar{\sigma}} c_{i\sigma}; c_{j\sigma}^\dagger \right\rangle \right\rangle_\omega - \left\langle \left\langle c_{k\bar{\sigma}}^\dagger c_{i\bar{\sigma}} c_{i\sigma}; c_{j\sigma}^\dagger \right\rangle \right\rangle_\omega \right\}. \end{aligned} \quad (2.29)$$

To break the hierarchy of the Green's function equations, an approximate expression will be used in each of the last two terms of the equation (2.29). These approximations are obtained by the methods indicated by Zubarev [50] and are given by

$$\left\langle \left\langle n_{i\bar{\sigma}} c_{k\sigma}; c_{j\sigma}^\dagger \right\rangle \right\rangle_\omega \approx \langle n_{i\bar{\sigma}} \rangle G_{kj}^\sigma(\omega), \quad (2.30)$$

$$\left\langle \left\langle c_{i\bar{\sigma}}^\dagger c_{k\bar{\sigma}} c_{i\sigma}; c_{j\sigma}^\dagger \right\rangle \right\rangle_\omega \approx \langle c_{i\bar{\sigma}}^\dagger c_{k\bar{\sigma}} \rangle G_{ij}^\sigma(\omega), \quad (2.31)$$

$$\left\langle \left\langle c_{k\bar{\sigma}}^\dagger c_{i\bar{\sigma}} c_{i\sigma}; c_{j\sigma}^\dagger \right\rangle \right\rangle_\omega \approx \langle c_{k\bar{\sigma}}^\dagger c_{i\bar{\sigma}} \rangle G_{ij}^\sigma(\omega). \quad (2.32)$$

Substituting these approximations into equation (2.29), one obtains that

$$\omega\Gamma_{ij}^\sigma(\omega) = \delta_{ij} \langle n_{i\bar{\sigma}} \rangle + (\epsilon_0 + U)\Gamma_{ij}^\sigma(\omega) + \langle n_{i\bar{\sigma}} \rangle \sum_{k \neq i} t_{ik} G_{kj}^\sigma(\omega) \quad (2.33)$$

and, therefore,

$$\Gamma_{ij}^\sigma(\omega) = \frac{\langle n_{i\bar{\sigma}} \rangle}{\omega - \epsilon_0 - U} \left\{ \delta_{ij} + \sum_{k \neq i} t_{ik} G_{kj}^\sigma(\omega) \right\}. \quad (2.34)$$

Substituting it in (2.28) we have that

$$\omega G_{ij}^\sigma(\omega) = \epsilon_0 G_{ij}^\sigma(\omega) + \left\{ 1 + \frac{U \langle n_{i\bar{\sigma}} \rangle}{\omega - \epsilon_0 - U} \right\} \left\{ \delta_{ij} + \sum_{k \neq i} t_{ik} G_{kj}^\sigma(\omega) \right\}. \quad (2.35)$$

This equation can be solved using the discrete Fourier transform. Writing

$$G_{ij}^\sigma(\omega) = \frac{1}{N} \sum_{\mathbf{k}} G^\sigma(\mathbf{k}, \omega) e^{i\mathbf{k}(\mathbf{R}_i - \mathbf{R}_j)}, \quad (2.36)$$

we get from equation (2.35) that

$$(\omega - \epsilon_0) G^\sigma(\mathbf{k}, \omega) = \left\{ 1 + \frac{U \langle n_{i\bar{\sigma}} \rangle}{\omega - \epsilon_0 - U} \right\} \left\{ \frac{1}{N} + (\epsilon_{\mathbf{k}} - \epsilon_0) G^\sigma(\mathbf{k}, \omega) \right\}. \quad (2.37)$$

Finally,

$$G^\sigma(\mathbf{k}, \omega) = \frac{1}{N} \frac{\omega - \epsilon_0 - U(1 - \langle n_{i\bar{\sigma}} \rangle)}{(\omega - \epsilon_{\mathbf{k}})(\omega - \epsilon_0 - U) + \langle n_{i\bar{\sigma}} \rangle (\epsilon_0 - \epsilon_{\mathbf{k}})U}, \quad (2.38)$$

which is the Hubbard I approximation to the correlation problem.

The solution given by equation (2.38) will be investigated next. Equation (2.38) is a rational function of ω and may be resolved into partial fractions according to

$$G^\sigma(\mathbf{k}, \omega) = \frac{1}{N} \frac{1}{\epsilon_{\mathbf{k}\sigma}^{(1)} - \epsilon_{\mathbf{k}\sigma}^{(2)}} \left\{ \frac{\epsilon_{\mathbf{k}\sigma}^{(1)} - \epsilon_0 - U(1 - \langle n_{i\bar{\sigma}} \rangle)}{\omega - \epsilon_{\mathbf{k}\sigma}^{(1)}} - \frac{\epsilon_{\mathbf{k}\sigma}^{(2)} - \epsilon_0 - U(1 - \langle n_{i\bar{\sigma}} \rangle)}{\omega - \epsilon_{\mathbf{k}\sigma}^{(2)}} \right\}, \quad (2.39)$$

where $\epsilon_{\mathbf{k}\sigma}^{(1)} < \epsilon_{\mathbf{k}\sigma}^{(2)}$ are the two roots of

$$(\omega - \epsilon_{\mathbf{k}})(\omega - \epsilon_0 - U) + \langle n_{i\bar{\sigma}} \rangle (\epsilon_0 - \epsilon_{\mathbf{k}})U = 0. \quad (2.40)$$

It can be shown that $\epsilon_{\mathbf{k}\sigma}^{(1)} < \epsilon_0 + U(1 - \langle n_{i\bar{\sigma}} \rangle) < \epsilon_{\mathbf{k}\sigma}^{(2)}$, then the Green's functions (2.39) take the form

$$G^\sigma(\mathbf{k}, \omega) = \frac{1}{N} \left\{ \frac{A_{\mathbf{k}\sigma}^{(1)}}{\omega - \epsilon_{\mathbf{k}\sigma}^{(1)}} + \frac{A_{\mathbf{k}\sigma}^{(2)}}{\omega - \epsilon_{\mathbf{k}\sigma}^{(2)}} \right\}, \quad (2.41)$$

with $A_{\mathbf{k}\sigma}^{(1)}, A_{\mathbf{k}\sigma}^{(2)} > 0$.

Summing over the values of the wave vector \mathbf{k} ,

$$G^\sigma(\omega) = \frac{1}{N} \sum_{\mathbf{k}} G^\sigma(\mathbf{k}, \omega) = \frac{1}{N} \left\{ \frac{A^{(1)}}{(\omega - \epsilon^{(1)}) - i\eta} + \frac{A^{(2)}}{(\omega - \epsilon^{(2)}) - i\eta} \right\} \quad (2.42)$$

and again using the relation

$$\lim_{\eta \rightarrow 0} \left[\frac{1}{(\omega - \epsilon) - i\eta} \right] = P \left[\frac{1}{(\omega - \epsilon)} \right] + i\pi\delta(\omega - \epsilon), \quad (2.43)$$

we get

$$\rho(\omega) = \frac{1}{N} \sum_{\mathbf{k}} \text{Im}\{G^\sigma(\mathbf{k}, \omega)\} \quad (2.44)$$

for any distribution.

To facilitate the interpretation of the properties of the solution, we consider a constant, or rectangular, conduction band of bandwidth $2D$ defined by

$$\rho_0 = \begin{cases} \frac{1}{2D}, & \text{for } -D \leq \epsilon - \mu \leq D \\ 0 & \text{, otherwise} \end{cases}, \quad (2.45)$$

where μ is the chemical potential. The bandwidth of real materials is approximately 1 to 5 eV, which roughly scales the parameter $2D$. For a rectangular distribution of width $2D$, the integrated Green's function is as follows:

$$G^\sigma(\omega) = \frac{1}{2D} \int_{-D+\mu}^{D+\mu} d\epsilon G^\sigma(\epsilon, \omega). \quad (2.46)$$

For the Green's functions of our problem,

$$G^\sigma(\epsilon, \omega) = \frac{1}{N} \frac{\omega - \epsilon_0 - U(1 - \langle n_{i\bar{\sigma}} \rangle)}{(\omega - \epsilon)(\omega - \epsilon_0 - U) + \langle n_{i\bar{\sigma}} \rangle (\epsilon_0 - \epsilon)U}, \quad (2.47)$$

making the convenient changes of variables, we get that

$$G^\sigma(\omega) = \frac{1}{2D} \int_{-D+\mu}^{D+\mu} \frac{d\epsilon}{\epsilon - B} = \frac{1}{2D} \ln \left(\frac{-B + D + \mu}{-B - D + \mu} \right), \quad (2.48)$$

where

$$B = \frac{\omega(\omega - \epsilon_0 - U) + \langle n_{i\bar{\sigma}} \rangle U \epsilon_0}{(\omega - \epsilon_0 - U) + \langle n_{i\bar{\sigma}} \rangle U}. \quad (2.49)$$

Here is an important observation: since the GF obtained depends on the occupation numbers $\langle n_{i\bar{\sigma}} \rangle$, these quantities must be calculated self-consistently from the GF given by equation (2.48), which can be done from the relation

$$n = \left(\frac{1}{\pi} \right) \int_{-\infty}^{\infty} dz n_F(z) \text{Im}(G^\sigma(z)), \quad (2.50)$$

which can be obtained from the fluctuation-dissipation theorem [50], where $z = \omega + i\eta$, with η being an infinitesimal quantity and $n_F(z) = (\exp(\beta z) + 1)^{-1}$ is the Fermi distribution.

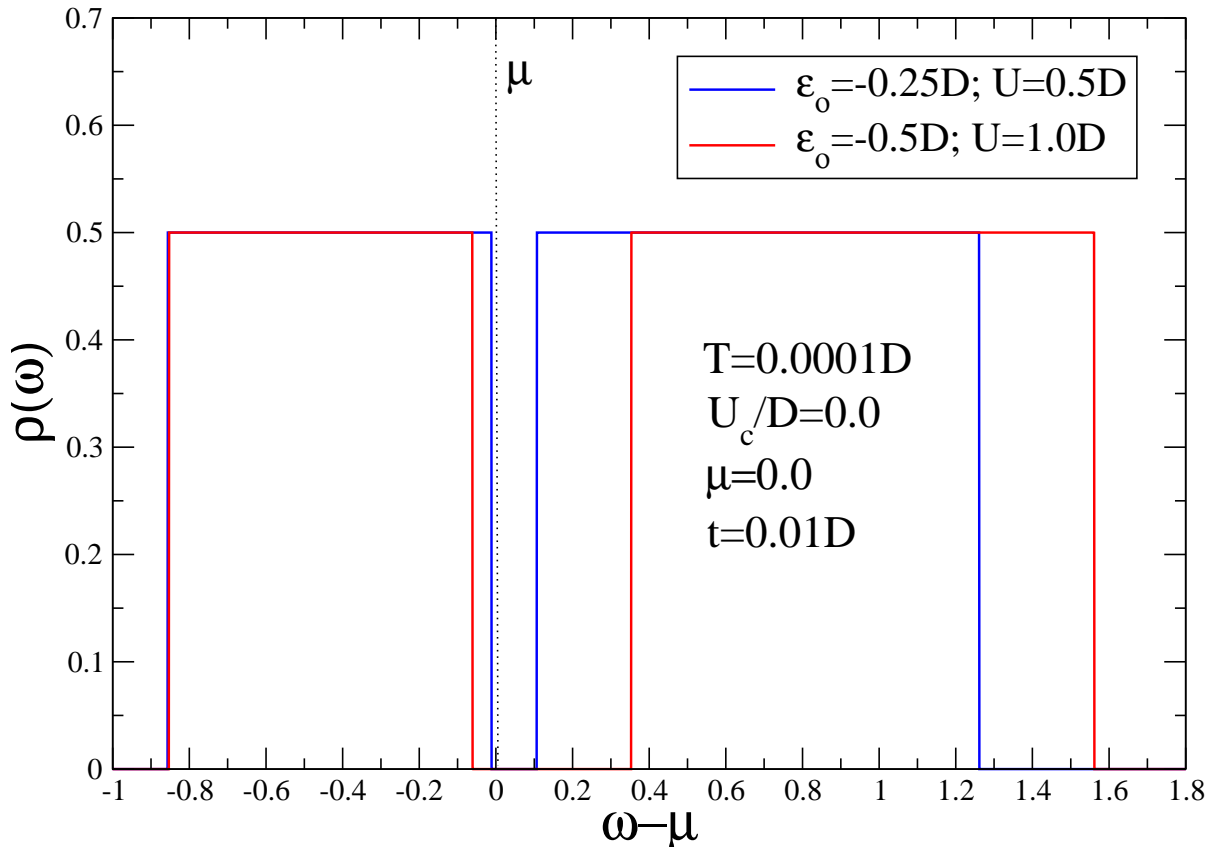


Figure 2.1: Density of states for different values of energy ϵ_0 and electronic correlation U .

There is a very important subtlety in the calculation of the occupation numbers that often goes unnoticed. When we apply the relation (2.50) considering the Hubbard I approximation expressed by the equation (2.48), we obtain an occupation $n = n_s + n_d$, where n_s is the single occupancy and n_d the double occupancy, as the Hubbard I GF includes both processes. To extract the double occupancy from the calculations we must calculate it separately, which is done using the Green's function $\Gamma(\omega)$, calculated in Hubbard's original work [6]. This relationship is given by:

$$\Gamma^\sigma(\omega) = A(B - \epsilon_0)G^\sigma(\omega), \quad (2.51)$$

where

$$A = \frac{\langle n_{i\bar{\sigma}} \rangle}{(\omega - \epsilon_0 - U)}. \quad (2.52)$$

Thus, with the Γ function, we can calculate the double occupancy from the relation:

$$n_d = \left(\frac{1}{\pi}\right) \int_{-\infty}^{\infty} dz n_F(z) \text{Im}(\Gamma^\sigma(z)). \quad (2.53)$$

Thus, having obtained the double occupation number n_d , the single occupation number n_s is obtained from the relation $n_s = n - n_d$. Finally, the number of unoccupied states n_{vac} is obtained by equation (2.50), but with the Fermi distribution function n_F replaced by $(1 - n_F)$. Having calculated all the occupation numbers we can obtain the completeness relation $C = n_{vac} + n_s + n_d = 1$, which is satisfied by the Hubbard I approximation.

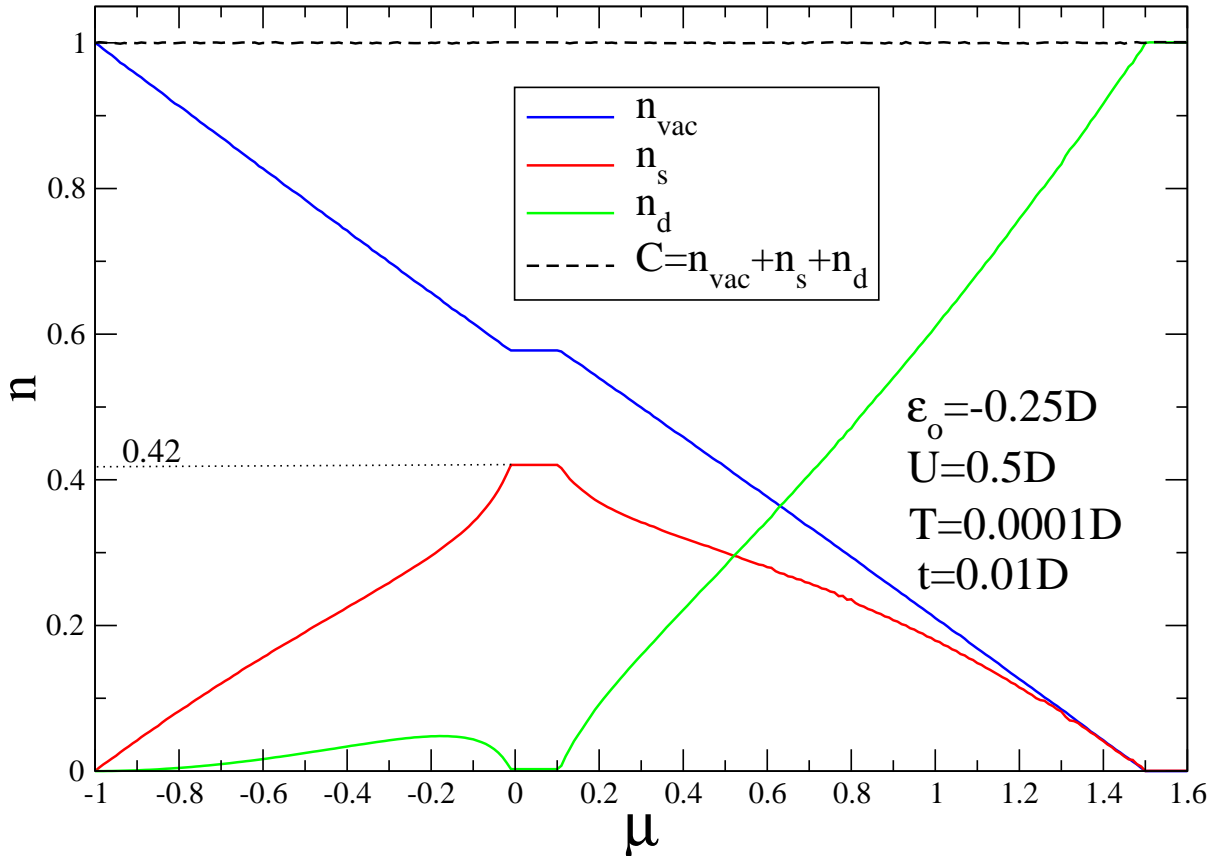


Figure 2.2: Occupation numbers as functions of the chemical potential μ .

In figure 2.1 we represent the density of states for two different values of energy ϵ_0 and electronic correlation U at half-filling. The interesting point is that the total area of the density of states is always equal to unity for any parameter space, whether at half-filling or not. This is the correct result, however, the areas of the sub-bands are not conserved and at half-filling, they are different from 0.5. We calculated the area of the lower Hubbard sub-band for both cases, which is associated with the single occupancy, and the results are 0.42 for $\epsilon_0 = -0.25D$ and $U = 0.5D$, and 0.39 for $\epsilon_0 = -0.5D$ and $U = 1.0D$. Another important point here is that the Hubbard I approximation overestimates the electronic correlation and the Mott transition occurs for any electronic correlation U greater than zero. No matter how small this value is, a gap opens in the density of states. Thus, we can say that the critical value of U where the Mott transition occurs in the Hubbard I approximation is $U_c = 0$. Our first motivation for this work is to get this value correctly for the model.

In figure 2.2 we represent the occupation numbers as functions of the chemical potential μ . For μ far below the level $\epsilon_0 = -0.25D$, the Hubbard bands are completely unoccupied and this is reflected in the numbers of unoccupied states $n_{vac} = 1$. As μ grows, the number of unoccupied states decreases and the number of single occupied states n_s (here including electrons with spin up and down) increases. However, the lower Hubbard sub-band is completely filled when $n_s = 0.42$, and reaches a constant value as μ keeps increasing near $\mu = 0$. We can also observe that there are a small number of doubly occupied states in the region corresponding to the lower Hubbard sub-band. From the moment μ leaves the gap,

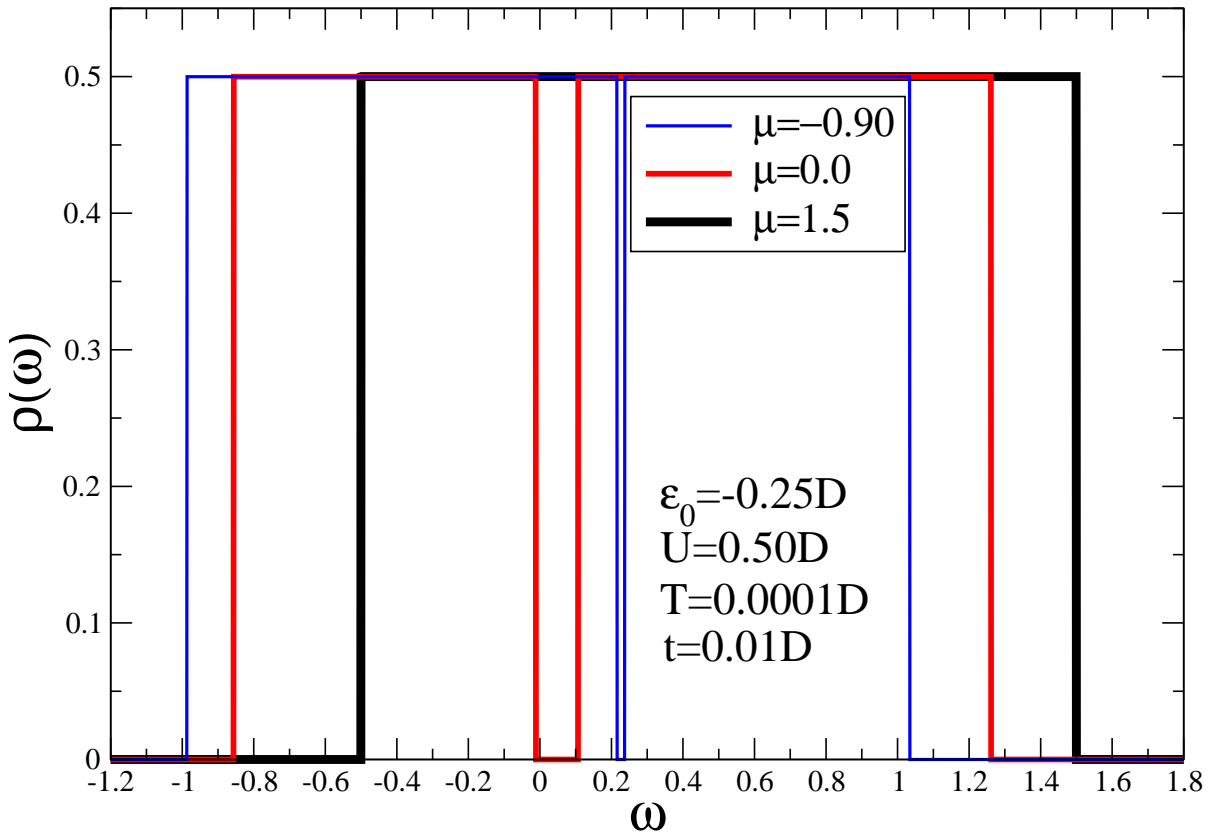


Figure 2.3: Limiting cases for the density of states for different values of chemical potential μ .

the double occupancy states grow monotonically until reaching their maximum value $n_d = 1$ while the unoccupied and single occupancy states tend to zero. Another point to be observed in the graph is that the completeness relationship is satisfied by the Hubbard I approximation. Thus, we see that this approximation presents some positive aspects, mainly regarding the threshold values for the occupation numbers, which are correctly described.

In figure 2.3 we analyze the limiting cases for the density of states for different values of chemical potential μ . In the first case, we represent the density of states for $\mu = -0.90$, which corresponds to the case where the band is practically empty, which leads to the electronic correlation having no effects due to the absence of electrons. This way, the gap in the density of states tends to close and for smaller values of the chemical potential the gap effectively closes, thus recovering the empty band limit. In the second case, we represent the density of states for $\mu = 0.0$, which is the usual half-filled case with a gap in the density of states. Finally, we consider the case with $\mu = 1.5$, with the band completely filled with doubly occupied states and the gap does not exist due to the collapse of the Hubbard lower sub-band, but now we have a highly correlated system. This result of the Hubbard I approximation is interesting because it shows that we can have an insulator or a highly correlated metal depending on the value of the chemical potential μ , simply by increasing the number of charge carriers in the system, which can be achieved by doping.

In his third work, Hubbard significantly improved his first decoupling, introduced two new corrections to the Green's functions chain, and obtained the Hubbard III approximation, which alleviates

some of the issues presented by the Hubbard I approximation. In particular, the correlation is no longer overestimated, and the Mott transition happens for $U_c = \sqrt{3}D$. However, the renormalized Fermi liquid character is not recovered by Hubbard III (the dynamical mean-field theory [DMFT], for example, can recover this property).

2.3 The analytical solution for the one-dimensional Hubbard model

In this section, we study the thermodynamic limit of the ground-state properties of the one-dimensional Hubbard model. We focus on the calculation of the electron density, magnetization, single-particle gap and the ground-state energy. We obtain the ground-state phase diagram as function of the magnetic field and the chemical potential.

2.3.1 The noninteracting case - a point of reference

Before approaching the general case, let us consider the noninteracting case ($U = 0$) at zero magnetic field described by a tight-binding Hamiltonian

$$H_1 = \sum_{ij\sigma} t_{ij} c_{i\sigma}^\dagger c_{j\sigma}. \quad (2.54)$$

For practical reasons, let us consider only nearest neighbour hopping. Then, the Hamiltonian takes the form

$$H_1 = -t \sum_{\langle i,j \rangle \sigma} \left(c_{i\sigma}^\dagger c_{j\sigma} + c_{j\sigma}^\dagger c_{i\sigma} \right). \quad (2.55)$$

Zero temperature properties can be determined by diagonalizing the Hamiltonian going to momentum space using a Fourier transformation

$$c_{k\sigma}^\dagger = \frac{1}{\sqrt{L}} \sum_{j=1}^L e^{-ikj} c_{j\sigma}^\dagger, \quad (2.56)$$

where L is the number of sites in the lattice and the momenta are quantized by $k = \frac{2\pi n}{L}$; $n = -\frac{L}{2}, \dots, \frac{L}{2} - 1$. The Hamiltonian in momentum space is then

$$H_1 = \sum_{k\sigma} \epsilon_k c_{k\sigma}^\dagger c_{k\sigma} = \sum_{k\sigma} (-2t \cos k) n_{k\sigma}. \quad (2.57)$$

where ϵ_k is the single-particle energy of spin- σ electrons.

If the number of electrons N is equal to number of sites L , each allowed state k can be occupied by two opposite spins. Then, the ground-state of H_0 is constructed by filling the lower half of the band dispersion ($\epsilon_k < 0$ or $-\pi/2 < k < \pi/2$). Since half the band is filled, this is called the half-filled case. The ground-state of the half-filled case is an eigenstate of the Hamiltonian and to get the ground-state energy we must sum over all occupied states in the first Brillouin zone. Then, the ground-state energy of the noninteracting system can be obtained as

$$E_g = \sum_{|\mathbf{k}| < \pi/2, \sigma} \epsilon_{\mathbf{k}} n_{\mathbf{k}\sigma}. \quad (2.58)$$

In the thermodynamic limit, using the fact that the electron density

$$n_{\mathbf{k}\sigma} = \sum_{\sigma} \int_{-\pi/2}^{\pi/2} dk \rho_{\mathbf{k}\sigma}, \quad (2.59)$$

and using a constant density of spin up and spin down electrons $\rho_{\mathbf{k}\sigma} = 1/2\pi$, the expression becomes

$$E_g = \int_{-\pi/2}^{\pi/2} dk \frac{1}{2\pi} 2(-2t \cos k) = -\frac{4t}{\pi}. \quad (2.60)$$

This half-filled state represents a metal, since there are available states immediately nearby an electron in the highest energy state, given that the dispersion relation is continuous. Therefore, there is no single-particle gap. This band picture always represents a metallic system when the number of electrons per unit cell is odd (one in this case). There are situations in which this prediction of the band theory fails and they will be studied in the interacting case.

Still in the noninteracting case, let us account for the chemical potential and external magnetic field in the single-particle energy such that

$$\epsilon_{k\sigma} = -2t \cos k - \mu_{\sigma}, \quad (2.61)$$

where $\mu_{\uparrow} = \mu + h$, $\mu_{\downarrow} = \mu - h$ and h is the external magnetic field in units of the inverse Bohr magneton $1/\mu_B$. In the ground-state, the band for spin σ is filled in the interval $[-k_{F\sigma}, k_{F\sigma}]$

$$k_{F\sigma} = \begin{cases} 0 & \text{if } \mu_{\sigma} \leq -2 \\ \arccos(-\mu_{\sigma}/2) & \text{if } -2 < \mu_{\sigma} < 2 \\ \pi & \text{if } \mu_{\sigma} \geq 2. \end{cases} \quad (2.62)$$

The electron density and magnetization per site are given by

$$n = \sum_{\sigma} \int_{-k_{F\sigma}}^{k_{F\sigma}} dk \rho_{k\sigma} = \frac{1}{\pi} \sum_{\sigma} k_{F\sigma}, \quad (2.63)$$

$$m = \frac{1}{2} \left[\int_{-k_{F\uparrow}}^{k_{F\uparrow}} dk \rho_{k\uparrow} - \int_{-k_{F\downarrow}}^{k_{F\downarrow}} dk \rho_{k\downarrow} \right] = \frac{1}{2\pi} [k_{F\uparrow} - k_{F\downarrow}], \quad (2.64)$$

where we consider the densities of spin up and spin down electrons constant $\rho_{k\sigma} = 1/2\pi$. The ground-state energy for this case is then

$$E_g = \sum_{\sigma} \int_{-k_{F\sigma}}^{k_{F\sigma}} dk \rho_{k\sigma} \epsilon_{k\sigma} = \frac{1}{\pi} \sum_{\sigma} (-2t \sin(k_{F\sigma}) - \mu_{\sigma}), \quad (2.65)$$

which falls into the previous case when $\mu = 0$ and $h = 0$.

To investigate the phase diagram, we focus on the case where $\mu < 0$ (the case for $\mu > 0$ is symmetrical) and we set $t = 1$. Considering the ground-state composed of a spin up band and a spin down band, there are four possibilities:

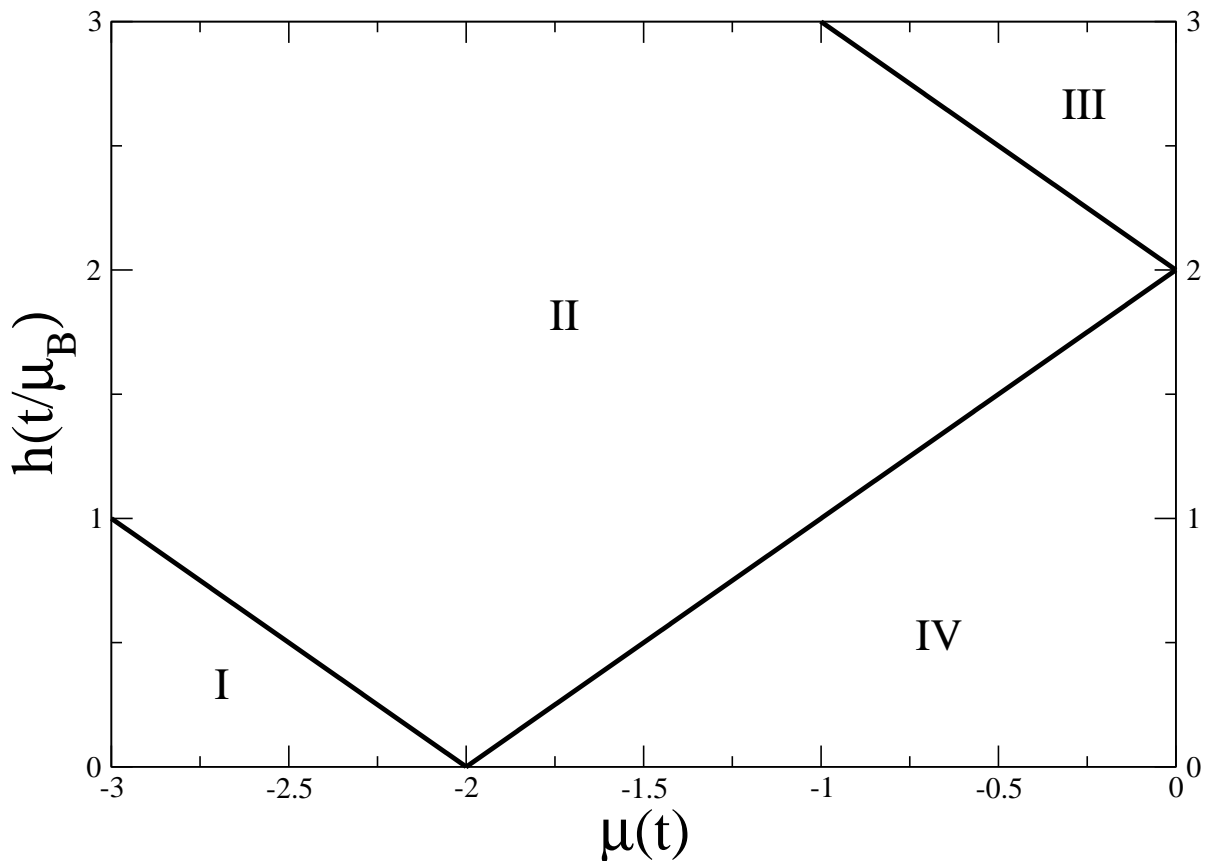


Figure 2.4: Ground-state phase diagram at zero temperature in h vs. μ coordinates for the noninteracting case. In terms of the densities and magnetization the four phases are characterized by I: $n = m = 0$; II: $n_{down} = 0, 0 < n_{up} < 1$; III: $n_{down} = 0, n_{up} = 1$; IV: $0 < n < 1, 0 \leq m \leq 1/2$.

- Phase I - Vacuum - $k_{F\sigma} = 0, n = 0, m = 0$. Both bands are empty and the ground-state is the empty lattice. Both electron density and magnetization are zero. Using equation (2.62), the chemical potential must be

$$\mu \leq -2 - h. \quad (2.66)$$

- Phase II - Partially filled and spin polarized band - $k_{F\downarrow} = 0, 0 < k_{F\uparrow} < \pi, 0 < n < 1, m = n/2$. The spin down band is empty and the spin up band is partially filled. The electron density is between zero and one and the magnetization is half the electron density. Then

$$n = 2m = 2 \frac{1}{2\pi} [k_{F\uparrow} - 0] = \frac{1}{\pi} \arccos \left(-\frac{\mu + h}{2} \right). \quad (2.67)$$

According to equation (2.62), the chemical potential must be

$$\mu > -2 - h, \quad \mu < 2 - h, \quad \mu < -2 + h. \quad (2.68)$$

- Phase III - Half filled and spin polarized band - $k_{F\downarrow} = 0, 0 < k_{F\uparrow} = \pi, n = 1, m = 1/2$. The spin down band is empty and the spin up band is completely filled. The electron density is one and the magnetization is $1/2$.

- Phase IV - Partially filled and magnetized band - $0 < k_{F\sigma} < \pi$, $0 < n < 1$, $0 \leq m < n/2$. Both bands are partially filled. The electron density is between zero and one and the magnetization is between zero and 1/2.

$$n = \frac{1}{\pi} \left[\arccos \left(-\frac{\mu + h}{2} \right) + \arccos \left(-\frac{\mu - h}{2} \right) \right], \quad (2.69)$$

$$m = \frac{1}{2\pi} \left[\arccos \left(-\frac{\mu + h}{2} \right) - \arccos \left(-\frac{\mu - h}{2} \right) \right]. \quad (2.70)$$

The phase diagram containing the four phases mentioned above can be seen in figure 2.4.

2.3.2 The interacting case - the Bethe ansatz [BA] solution

The solution of the stationary Schrödinger equation for the one-dimensional Hubbard model can be reduced to a set of algebraic equations, which is tractable in the thermodynamic limit. These equations were first obtained by E. H. Lieb and F. Y. Wu [14,51], based on a method called the nested (coordinate) Bethe ansatz, and they describe the ground-state of the model by a system of integral equations for root densities. The process to obtain these integral equations and to obtain the properties of the solution from these equations is rather extensive and out of the scope of this thesis. However, the main aspects and results of this solution will be discussed in this section as they will be used as a benchmark in chapter 3.

We begin at zero magnetic field. As obtained by Lieb and Wu [14,51], the ground-state energy E_g (of $H + \mu N$) can be calculated exactly by means of the Bethe ansatz at half-filling. For $E_0 - \mu = -U/2$, the model has particle-hole symmetry and the band is half-filled. If L denotes the number of sites, it follows that the ground-state energy per site at half-filling is

$$E_g/L = -4t \int_0^\infty dx \frac{J_0(x)J_1(x)}{x[1 + \exp(xU/2t)]}, \quad (2.71)$$

where $J_0(x)$ and $J_1(x)$ are Bessel functions of the first kind. Also, the exact expression for the gap in the DOS at half-filling is given by [14, 51, 52]

$$\Delta = \frac{16t^2}{U} \int_1^\infty dx \frac{\sqrt{x^2 - 1}}{\sinh(2\pi tx/U)}. \quad (2.72)$$

There is a gap for any $U > 0$. The critical correlation for the Mott transition is $U_c = 0$. Another result is the interpolative formula for the double occupation n_d at half-filling [53]

$$n_d = \frac{1 + c_1 U}{4(1 + c_2 U + c_3 U^2 + c_4 U^3)}, \quad (2.73)$$

where $c_1 = 2.445$, $c_2 = 2.581$, $c_3 = 0.090$, and $c_4 = 0.220$ for 1D. This formula also works for 2D and 3D, with different coefficients [53]. These results for the ground-state energy, the gap and the double occupation are valid at the $T = 0$ limit.

Figures 2.5 a) and 2.5 b) show the results for the Bethe ansatz in the half-filled case for the single-particle gap and the ground-state energy as functions of the correlation U , respectively. One can see in figure 2.5 b) that the ground-state energy for $U = 0$ agrees with the result for the noninteracting case, equation (2.60), when $t = 1$, where $E_g = -4/\pi = -1.2732$. Figure 2.6 shows the result for the double occupation number.

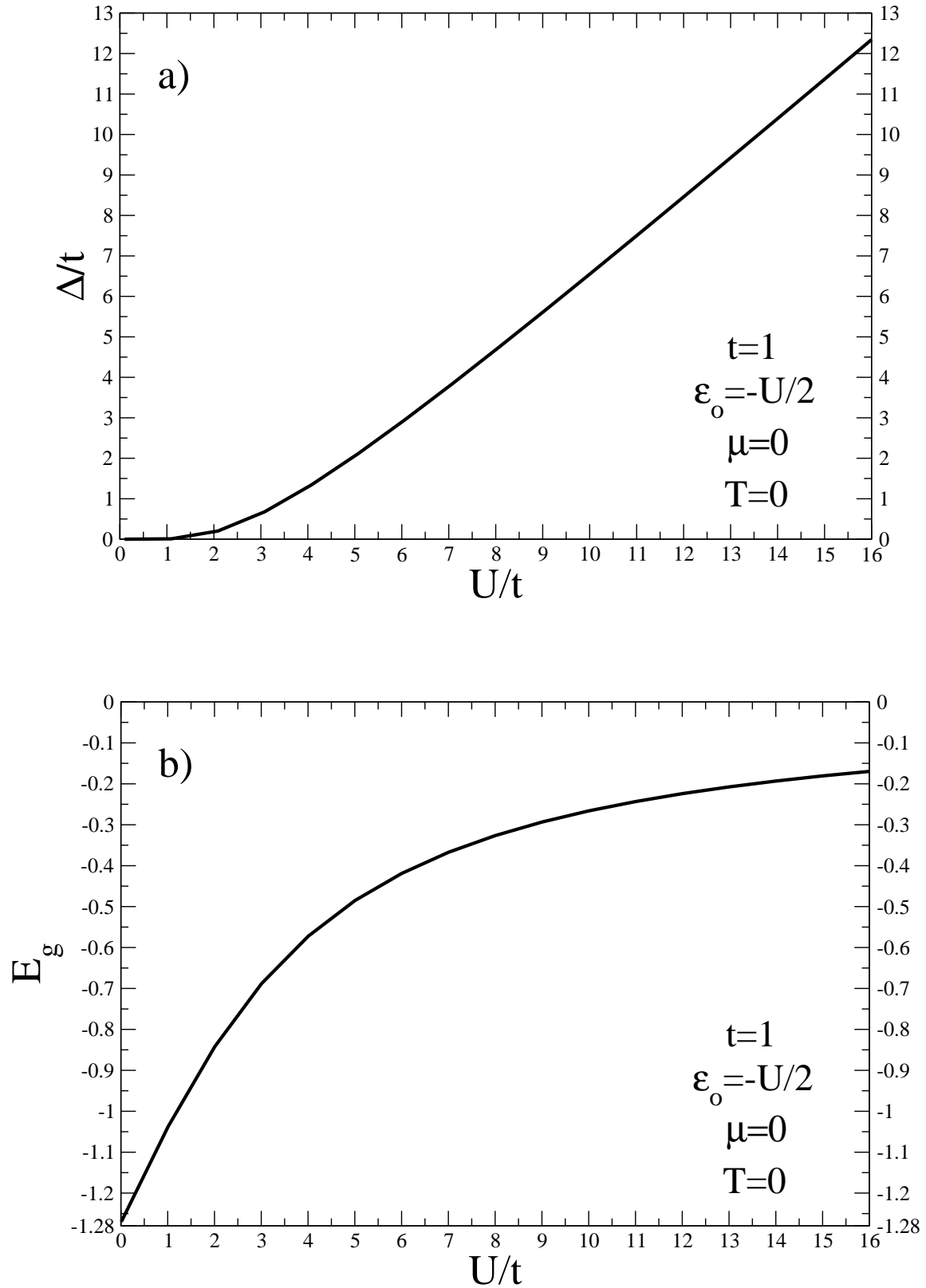


Figure 2.5: Results for the Bethe ansatz in the half-filled case for the a) Single-particle gap and the b) Ground-state energy as functions of the correlation U .

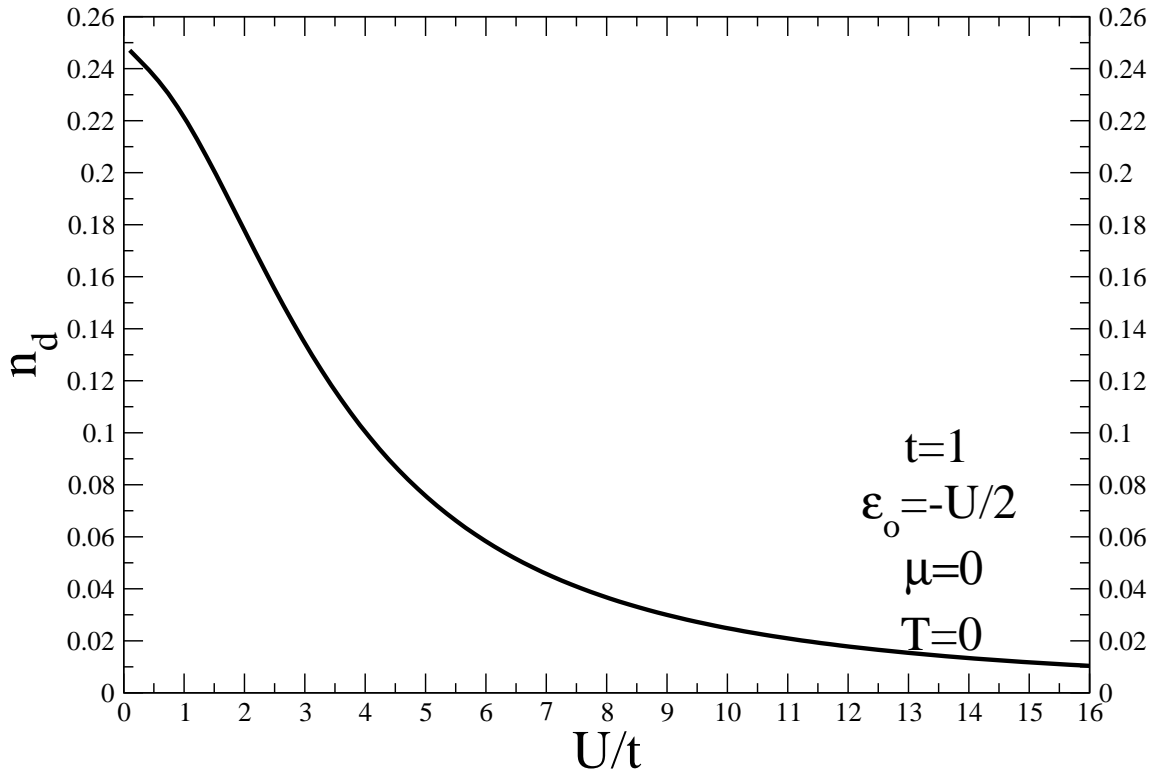


Figure 2.6: Results for the Bethe ansatz in the half-filled case for the double occupation number as function of the correlation U .

In order to study the behaviour of the electron density, magnetization, and the ground-state phase diagram of the interacting case outside of the half-filled case, we need to introduce the integral equations describing the root densities of the ground-state. At the $T = 0$ limit they are [14, 51]

$$\rho(k) = \frac{1}{2\pi} + \cos k \int_{-A}^A d\lambda a_1(\sin k - \lambda) \sigma(\lambda), \quad (2.74)$$

$$\sigma(\lambda) = \int_{-Q}^Q dk a_1(\lambda - \sin k) \rho(k) - \int_{-A}^A d\lambda' a_2(\lambda - \lambda') \sigma(\lambda'), \quad (2.75)$$

where

$$a_l(x) = \frac{1}{2\pi} \frac{2lu}{(lu)^2 + x'^2}, \quad u = \frac{U}{4t}. \quad (2.76)$$

For a system containing N electrons of which M are spin down electrons, the integrated densities yield the total number of electrons per site and the number of spin down electrons per site, respectively, as

$$\int_{-Q}^Q dk \rho(k) = \frac{N}{L}, \quad \int_{-A}^A d\lambda \sigma(\lambda) = \frac{M}{L} = \frac{N_{down}}{L}. \quad (2.77)$$

The parameters Q and A fix the electron density n and magnetization per site m via

$$n = \frac{N}{L} = \int_{-Q}^Q dk \rho(k), \quad m = \frac{N - 2M}{2L} = \frac{1}{2} \left[\int_{-Q}^Q dk \rho(k) - 2 \int_{-A}^A d\lambda \sigma(\lambda) \right], \quad (2.78)$$

and the ground-state free energy per site is given by

$$f = e - \mu n - 2hm = \int_{-Q}^Q dk (-2t \cos k - \mu - 2u - h) \rho(k) + 2h \int_{-A}^A d\lambda \sigma(\lambda) + u, \quad (2.79)$$

where the energy per site is $e = -2t \cos k - \mu_\sigma - 2u$, $\mu_\uparrow = \mu + h$, $\mu_\downarrow = \mu - h$, and h is the external magnetic field. The dressed energies satisfy the system of integral equations

$$\bar{\kappa}(k) = -2t \cos k - \mu - 2u - h + \int_{-A}^A d\lambda a_1(\sin k - \lambda) \epsilon(\lambda), \quad (2.80)$$

$$\epsilon(\lambda) = 2h + \int_{-Q}^Q dk \cos k a_1(\sin k - \lambda) \bar{\kappa}(k) - \int_{-A}^A d\lambda' a_2(\lambda - \lambda') \epsilon(\lambda'). \quad (2.81)$$

They play an important role in understanding the phase diagram. Other than fixing the electron density and magnetization, the integration boundaries are the points at which the dressed energies change sign. As functions of the chemical potential and magnetic field, they are determined by the conditions

$$\bar{\kappa}(\pm Q) = 0, \quad \epsilon(\pm A) = 0. \quad (2.82)$$

The different phases of the system are most easily identifiable considering the integration boundaries Q and A as control parameters. First, when $Q = 0$, $A = 0$ and this corresponds to an empty system, where $N = 0$. Second, one can see, by using equation (2.74) and using the fact that $\int_{-\pi}^{\pi} dk \cos k f(\sin k) = 2 \int_0^{\pi} dk \cos k f(\sin k) = 0$, that when $Q = \pi$ the system is half-filled where there is one electron per site, $N/L = 1$. Third, when $A = \infty$, using equations (2.74), (4.2) and (2.77), $M/L = \int_{-\infty}^{\infty} d\lambda \sigma(\lambda) = 1/2 \int_{-Q}^Q dk \rho(k) = N/2L$ and the magnetization $m = (N - 2M)/2L$ is equal to zero. Fourth, for $A = 0$, the ground-state is fully magnetized as $M = 0$ by (2.77). Using these results in the case where $\mu < 0$ (the case for $\mu > 0$ is symmetrical) and $t = 1$, we can observe the following five different phases:

- Phase I - Vacuum - $Q = 0$, $A = 0$, $n = 0$, $m = 0$. Both bands are empty and the ground-state is the empty lattice. Both electron density and magnetization are zero. According to equation (2.79), the chemical potential must be

$$\mu \leq \mu_0(h) = -2 - 2u - h. \quad (2.83)$$

- Phase II - Partially filled and spin polarized band - $0 \leq Q \leq \pi$, $A = 0$, $0 < n < 1$, $m = n/2$. The spin down band is empty and the spin up band is partially filled. According to equation (2.77), μ , h and Q are related via

$$\cos Q = -1/2(\mu + h + 2u) \quad (2.84)$$

and the magnetic field satisfies the relation

$$h \leq h_u = 2 - \mu - 2u. \quad (2.85)$$

Also, the magnetic field must be greater than the critical value

$$h \geq h_c = \frac{2u}{\pi} \int_0^Q dk \cos k \frac{\cos k - \cos Q}{u^2 + (\sin k)^2}. \quad (2.86)$$

The electron density is between zero and one and is given by

$$n = \frac{1}{\pi} \arccos \left(1 - \frac{\mu - \mu_0(h)}{2} \right). \quad (2.87)$$

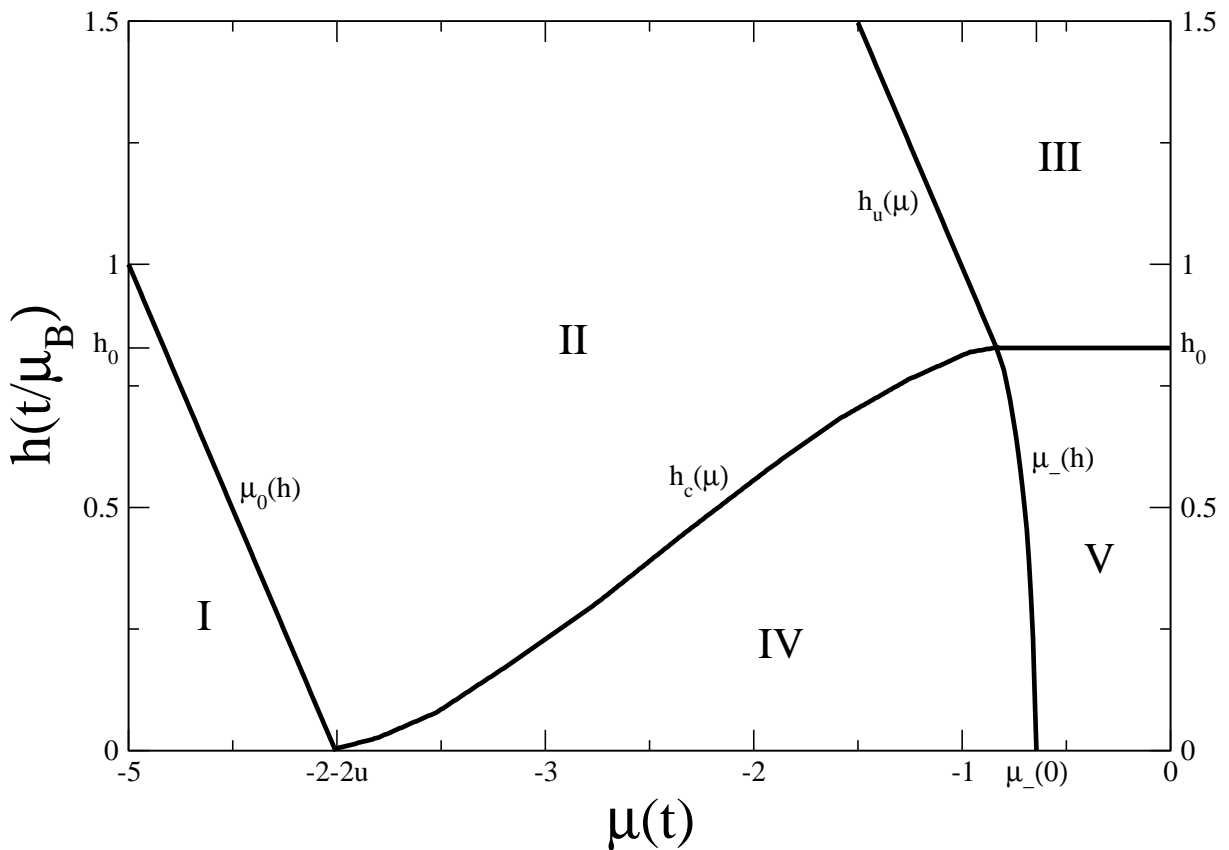


Figure 2.7: Ground-state phase diagram at zero temperature in h vs. μ coordinates for the interacting case for $u = 1$. In terms of the densities and magnetization the five phases are characterized by I: $n = m = 0$; II: $n_{down} = 0$, $0 < n_{up} < 1$; III: $n_{down} = 0$, $n_{up} = 1$; IV: $0 < n < 1$, $0 \leq m \leq 1/2$; V: $n = 1$, $m \geq 0$.

- Phase III - Half-filled and spin polarized band - $Q = \pi$, $A = 0$, $n = 1$, $m = 1/2$. The spin down band is empty and the spin up band is completely filled. The electron density is one and the magnetization is $1/2$. The integral equations for the dressed energies can be solved explicitly

$$\bar{\kappa}(k) = -2 \cos k - \mu - 2u - h, \quad (2.88)$$

$$\epsilon(\lambda) = 2h - 4 \operatorname{Re}(\sqrt{1 - (\lambda - iu)^2}) + 4u. \quad (2.89)$$

The requirements $\bar{\kappa}(k) \leq 0$ and $\epsilon(\lambda) \geq 0$ imply that

$$h \geq h_0(u) = 2\sqrt{1 + u^2} - 2u, \quad (2.90)$$

$$\mu \geq 2 - 2u - h. \quad (2.91)$$

- Phase IV - Partially filled and magnetized band - $0 < Q < \pi$ and $0 < A \leq \infty$, $0 < n < 1$, $0 \leq m < n/2$. Both bands are partially filled. The electron density is between zero and one and the magnetization is between zero and $1/2$. Generally, the integral equations can only be solved numerically in this region.

- Phase V - Half-filled and partially magnetized band - $Q = \pi$ and $0 < A \leq \infty$, $n = 1$, $m \geq 0$. The system is half-filled. The electron density is one and the magnetization is greater than zero. For $h > 0$, the boundary between phases IV and V is determined by the condition $\bar{\kappa}(\pm\pi) = 0$. For $h = 0$, which corresponds to $A = \infty$, the integral equations can be solved by Fourier transformation. The chemical potential μ_- separating the two phases is given by

$$\mu_-(h = 0) = 2 - 2u - 2 \int_0^\infty \frac{d\omega}{\omega} \frac{J_1(\omega) e^{-\omega u}}{\cosh(\omega u)}. \quad (2.92)$$

The phase diagram containing the five phases mentioned above can be seen in figure 2.7 for $u = 1$. A few important data points are: $h_0 = 0.828$, $\mu_-(0) = -0.643$, $-2 - 2u = -4$, and the quadruple point separating phases II, III, IV and V is the point $(x, y) = (-0.828, 0.828)$. The main result here is Phase V, which is not present in the noninteracting case. Throughout this phase the electron density n is equal to one, but the chemical potential μ varies. Therefore, the chemical potential is not an invertible function of the electron density. This is a remarkable result: for a given magnetic field h , as soon as the system is half-filled, it is not possible to add any more electrons in the ground-state by a small increase of the chemical potential. This can only happen if all possible eigenstates of the Hamiltonian with an additional electron are separated from the ground-state by a finite energy gap. This indicates that Phase V represents an insulating phase for the one-dimensional Hubbard model for any $u > 0$. Since this insulating phase is driven by the electronic correlation, its nature is unconventional and different from usual band insulators. Even before these results were obtained, Mott theorized that this phase was a result of electron-electron interactions splitting the conduction band into two bands, that became known latter as upper and lower Hubbard bands, separated by an energy gap [49] and, for that, such insulators are known as Mott insulators.

Chapter 3

The cumulant Green's functions method [CGFM]

The cumulant expansion of the Hubbard model was introduced by Hubbard [10,11] and applied to the infinite dimension limit by Metzner [1]. Metzner considered the local terms of eq. (2.2) as the unperturbed Hamiltonian and the kinetic energy, eq. (2.3), as a perturbation. The perturbation expansion was set up at Matsubara finite temperature T representation, employing the grand-canonical ensemble.

The single-particle temperature dependent Green's functions are defined by

$$G_{ij\sigma}(\tau) = - \left\langle \mathcal{T}[c_{i\sigma}(\tau), c_{j\sigma}^\dagger(0)] \right\rangle, \quad (3.1)$$

where \mathcal{T} represents the temporal ordering operator and the "time" τ is defined in the interval $[-\beta, \beta]$, where $\beta = 1/k_B T$, with k_B being the Boltzmann constant.

The Green's functions diagrammatic expansion for the single-band Hubbard model [1, 10, 11, 54] can be written in terms of Feynman diagrams. The relevant diagrams for a bipartite lattice are represented up to the fourth order in reference [1] and in figure 3.1. The analysis of these diagrams shows that they are formed by irreducible parts connected by hopping lines (irreducible parts are those diagrams that cannot be divided into two pieces by cutting a single hopping line). Due to this structure, in the limit of infinite dimension, the entire perturbative series can be formally added up in the temperature Matsubara representation, as shown in reference [1], resulting in a Dyson equation

$$G_{\mathbf{k}\sigma}(i\omega_n) = M_\sigma(i\omega_n) + M_\sigma(i\omega_n)\epsilon_{\mathbf{k}}G_{\mathbf{k}\sigma}(i\omega_n), \quad (3.2)$$

where $\omega_n = (2n+1)\pi k_B T$ with $n = \pm 1, \pm 2, \dots$ correspond to Matsubara frequencies along the imaginary axis, and $\epsilon_{\mathbf{k}}$ is the dispersion relation. $M_\sigma(i\omega_n)$ represents the irreducible cumulants corresponding to the single-particle Green's functions (3.1). In the infinite dimension limit, these cumulants do not depend on the wave vector \mathbf{k} ; they only depend on the Matsubara frequencies, which implies a huge simplification in the calculations, and the formal solution of (3.2) can be written as:

$$G_{\mathbf{k}\sigma}(i\omega_n) = \frac{M_\sigma(i\omega_n)}{1 - \epsilon_{\mathbf{k}}M_\sigma(i\omega_n)} = \frac{1}{M_\sigma^{-1}(i\omega_n) - \epsilon_{\mathbf{k}}}. \quad (3.3)$$

In terms of the self-energy Σ , as commonly used in the Dynamical Mean-Field Theory [DMFT],

$$M_{\sigma}^{-1}(i\omega_n) = i\omega_n + \mu - \Sigma(\sigma, i\omega_n). \quad (3.4)$$

There are other approaches, such as the cellular DMFT [C-DMFT] [29], that consider the spatial dependence of the self-energy.

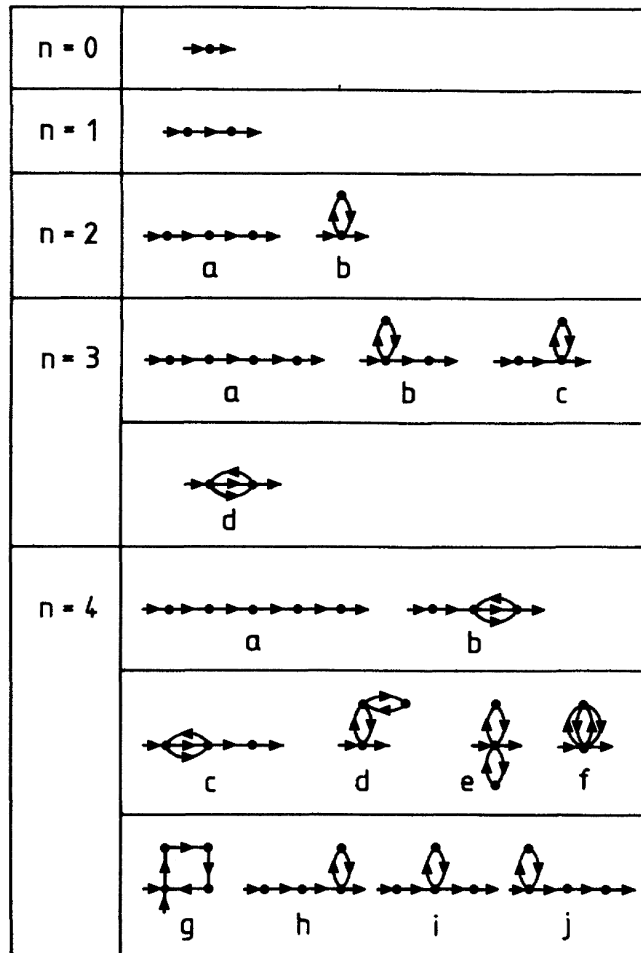


Figure 3.1: Diagrams that contribute to the one-particle Green's function for near neighbour hopping in a hypercubic lattice from zeroth ($n = 0$) up to fourth ($n = 4$) order, taken from reference [1].

3.1 The method

In this work, we only consider the 1D Hubbard model, and will benchmark the results obtained against the available solutions [14, 22–25, 51–53]. In the first step of the calculation, we employ exact diagonalization techniques to calculate the eigenvalues and eigenvectors of a linear cluster of N correlated sites. Due to computational limitations, we diagonalize matrices up to $N = 9$. We show that the results obtained with $N = 7, 8$, compared to the exact results [14, 51–53], produce excellent approximations for the gap in the density of states, double occupation number, and ground-state energy for the lattice as functions of the correlation. The results obtained for the occupation numbers as functions of the chemical potential, and the phase diagrams agree well with the results from the TBA and the QTM method [24].

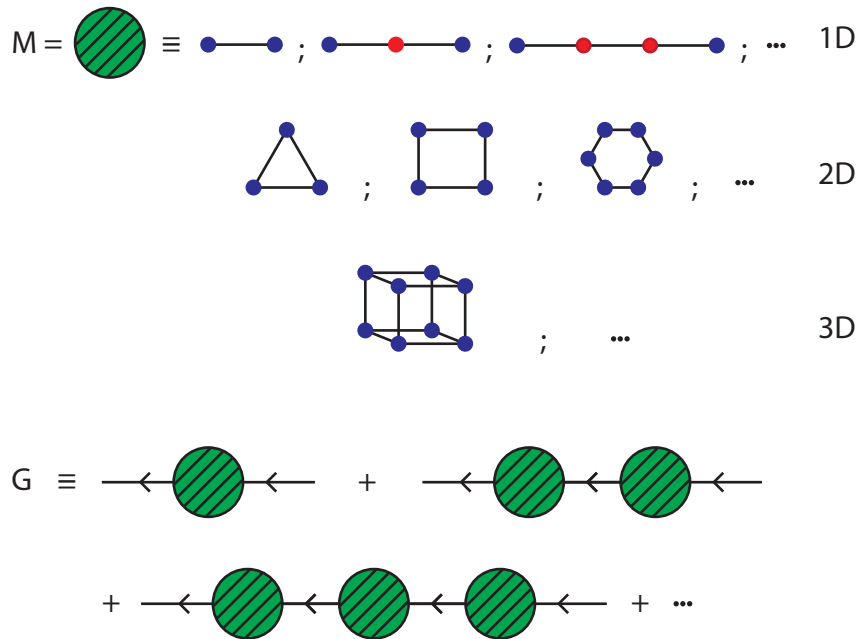


Figure 3.2: Schematic of the type of the clusters employed as a “seed” to generate cumulants M and from them the Dyson equation to calculate the lattice Green’s functions G of the method.

Fig. 3.2 presents a schematic representation of the clusters employed in the calculations. In the linear chains, the differently coloured sites indicate non-equivalent correlated sites, characterized by the number of neighbours and proximity to the edge of the chain. In this case, we should perform an average of the cumulants of those sites. However, all sites are equivalent in two or three-dimensional clusters and no averages need to be performed.

The first step of the method is to choose a cluster of atoms (“seed”) and diagonalize it to obtain its eigenvalues and eigenvectors. In an earlier work, the exact solution of the Anderson dimer [47] was employed as the “seed”. In this work we will use the exact solution of correlated clusters containing two or more sites modeled by the single-band one-dimensional Hubbard Hamiltonian as “seeds”. In the ED cluster calculations we use the hopping $t = 1$ as the energy unit. The local energy E_0 of the electrons is subtracted from the chemical potential in the presence of an external magnetic field h resulting in $\epsilon_0 = E_0 - \mu_\sigma$, with $\mu_\uparrow = \mu + h$, and $\mu_\downarrow = \mu - h$. It represents an important technical programming detail because we define the energies and the effects of the particle filling through the chemical potential and magnetic fields on the cluster eigenenergies. We do not need to consider those effects again during the embedding process of the cluster inside the lattice. The method is sufficiently general, allowing the choice of more sophisticated “seeds” than 1D as schematically represented in Fig. 3.2. We can also use “seeds” of 2D or 3D shapes to take into account the geometry of the lattice and the richness of interactions present in 2D and 3D systems.

The second step of the method is to use the eigenvalues and the eigenvectors obtained to calculate the cluster atomic Green’s functions employing the Lehmann representation. This calculation represents an additional difficulty over traditional ED calculations, but allows to take into account in a controllable way all atomic transitions inside the cluster of correlated sites used as a “seed” to generate the cumulants.

Table 3.1: Representation of the possible transitions present in the Hubbard Hamiltonian.

I_x	1	2	3	4
$\alpha = (b, a)$	$(0, \uparrow)$	$(0, \downarrow)$	(\downarrow, d)	(\uparrow, d)
g^{at}	g_{11}	g_{33}	g_{13}	g_{31}
$I_x = 1, 3$	$(0, \uparrow)$	(\downarrow, d)	$(0, \uparrow)$ and (\downarrow, d)	(\downarrow, d) and $(0, \uparrow)$
g^{at}	g_{22}	g_{44}	g_{24}	g_{42}
$I_x = 2, 4$	$(0, \downarrow)$	(\uparrow, d)	$(0, \downarrow)$ and (\uparrow, d)	(\uparrow, d) and $(0, \downarrow)$

(Top row) $\alpha = (b, a)$, a represents the initial state and b the final state. $I_x = 1, 3$ destroy one electron with spin up and $I_x = 2, 4$ destroy one electron with spin down. We use $\sigma = \uparrow$ and $\sigma = \downarrow$ to represent the up and down spins, respectively. The double occupation state is represented by the label d . (Middle and bottom rows) Atomic Green's functions associated to the processes $I_x = 1, 3$ and $I_x = 2, 4$.

Employing the spectral representation (Lehmann representation) [50], we obtain

$$g_{\sigma}^{at}(i\omega_s) = -e^{\beta\Omega} \sum_{n,r,r'} \frac{\exp(-\beta\varepsilon_{n-1,r}) + \exp(-\beta\varepsilon_{n,r'})}{i\omega_s + \varepsilon_{n-1,r} - \varepsilon_{n,r'}} \times \langle n-1, r | c_{i\sigma} | n, r' \rangle \langle n, r' | c_{i\sigma}^{\dagger} | n-1, r \rangle, \quad (3.5)$$

where Ω is the grand canonical potential, with $\beta = 1/k_B T$, and the eigenvectors $|n, r\rangle$ and eigenvalues $\varepsilon_{n,r}$ correspond to the complete solution of Hamiltonian of the atomic cluster. The atomic Green's functions can be rewritten as:

$$g_{\sigma}^{at}(i\omega_s) = e^{\beta\Omega} \sum_i \frac{r_{i,\sigma}}{i\omega_s - u_{i,\sigma}}, \quad (3.6)$$

where $r_{i,\sigma}$ are the residues and $u_{i,\sigma}$ the poles of the atomic Green's functions.

We should calculate the atomic Green's functions in matrix form, considering the electron spin destruction (creation) in the allowed atomic transitions. Here, n to $n \pm 1$ electrons, indicates the total number of electrons of the considered state as indicated in Table 3.1. This procedure is a central point of the method, differentiating it from other ED approaches like the VCA [2, 44, 45]. The focus of the calculation is on the possible atomic transitions within the atomic cluster.

We define the atomic Green's functions g_{11} , g_{33} , g_{13} and g_{31} associated with transitions that destroy a spin up electron and the functions g_{22} , g_{44} , g_{24} and g_{42} , associated with transitions that destroy a spin down electron, as detailed in table 3.1 (the superscript "at" is not used on the matrix components for simplicity). Also, according to table 3.1, it can be seen that the functions g_{11} and g_{22} are associated with states that initially contain a single electron, whereas g_{33} and g_{44} are associated with states that initially contain two electrons and g_{13} , g_{31} , g_{24} and g_{42} are the crossed GFs and are associated to the simultaneous destruction of electrons in states of single and double occupations. The atomic Green's functions associated with all of the allowed transitions within the cluster of correlated sites considered are calculated, separated, and indexed.

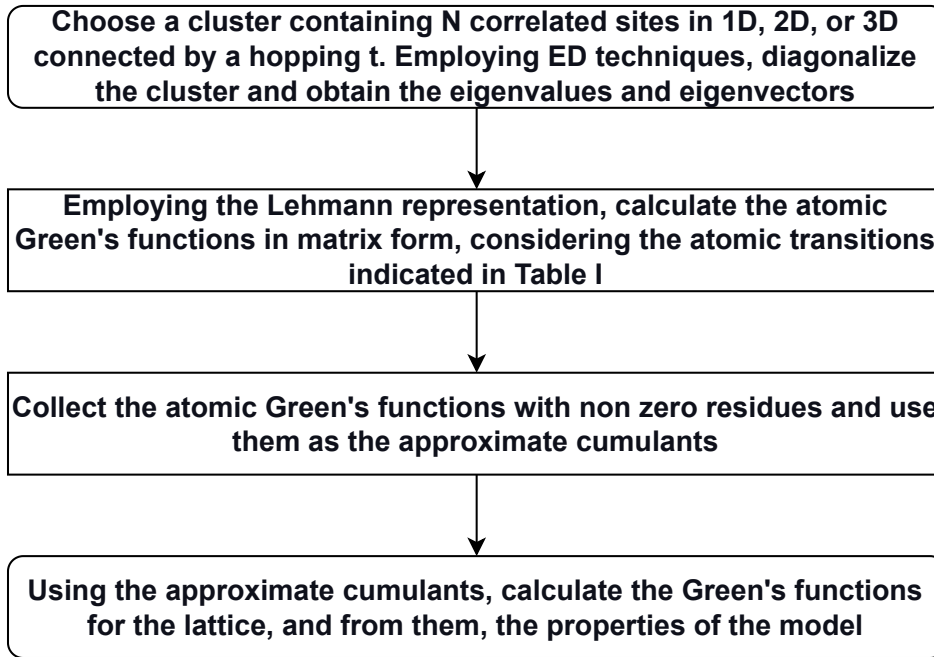


Figure 3.3: Flowchart of the steps of the CGFM.

Thus, one can write the atomic Green's functions as

$$\mathbf{g}_\sigma^{\text{at}}(i\omega) = \begin{pmatrix} g_{11} & g_{13} & 0 & 0 \\ g_{31} & g_{33} & 0 & 0 \\ 0 & 0 & g_{22} & g_{24} \\ 0 & 0 & g_{42} & g_{44} \end{pmatrix}. \quad (3.7)$$

Equation (3.7) presents itself in a diagonal block form because the selection rules do not allow transitions with spin inversion, and the spins up and down are disconnected.

In the third step of the method, we collect the atomic Green's functions (3.7) associated with the possible atomic transitions with residues different from zero and use them as the approximate atomic cumulants. They belong to the most straightforward class of cumulants that are connected by two Fermi-Dirac lines, as discussed by Hubbard in his fifth paper about cumulant expansions of the Hubbard model [10]:

$$\mathbf{m}_\sigma^{\text{at}}(i\omega) = \begin{pmatrix} m_{11} & m_{13} & 0 & 0 \\ m_{31} & m_{33} & 0 & 0 \\ 0 & 0 & m_{22} & m_{24} \\ 0 & 0 & m_{42} & m_{44} \end{pmatrix} = \begin{pmatrix} g_{11} & g_{13} & 0 & 0 \\ g_{31} & g_{33} & 0 & 0 \\ 0 & 0 & g_{22} & g_{24} \\ 0 & 0 & g_{42} & g_{44} \end{pmatrix}. \quad (3.8)$$

Finally, in the fourth step of the method, we use the atomic cumulants of eq. (3.8) as approximations to the formally exact cumulants $M_\sigma(i\omega_n)$ to calculate the Green's functions for the lattice $G_{\mathbf{k}\sigma}(i\omega_n)$, and from them, the dynamical properties of the model: the density of states, single-particle gap, ground-state energy, occupation numbers, phase diagram and other properties. A flowchart of the steps of the method is presented in Fig. 3.3.

Due to the nature of the method, there will always be the simple structure represented by a 4x4 deblocked matrix (3.7) for the atomic Green's functions and the atomic cumulants (3.8), regardless of the size or dimension of the atomic cluster used in the calculation. Using the same matrix form introduced in eq. (3.7) before and carrying out the analytical continuation of the cumulant Green's functions, eq. (3.3), to the real frequency axis, the Green's functions for the lattice become

$$\mathbf{G}_{\mathbf{k}\sigma}(\omega) = \mathbf{M}_\sigma(\omega) \cdot [\mathbf{I} - \mathbf{W}_{\mathbf{k}\sigma} \cdot \mathbf{M}_\sigma(\omega)]^{-1}. \quad (3.9)$$

Defining the exact cumulants and Green's functions for the lattice as

$$\mathbf{M}_\uparrow(\omega) = \begin{pmatrix} M_{11} & M_{13} \\ M_{31} & M_{33} \end{pmatrix}, \quad \mathbf{M}_\downarrow(\omega) = \begin{pmatrix} M_{22} & M_{24} \\ M_{42} & M_{44} \end{pmatrix}, \quad (3.10)$$

$$\mathbf{G}_{\mathbf{k}\uparrow}(\omega) = \begin{pmatrix} G_{11} & G_{13} \\ G_{31} & G_{33} \end{pmatrix}, \quad \mathbf{G}_{\mathbf{k}\downarrow}(\omega) = \begin{pmatrix} G_{22} & G_{24} \\ G_{42} & G_{44} \end{pmatrix}, \quad (3.11)$$

one obtains the exact Green's functions $\mathbf{G}_{\mathbf{k}\sigma}(\omega)$ by performing the matrix inversion in eq. (3.9):

$$\mathbf{G}_{\mathbf{k}\uparrow}(\omega) = \begin{pmatrix} M_{11} & M_{13} \\ M_{31} & M_{33} \end{pmatrix} \cdot \left[\begin{pmatrix} 1 & 0 \\ 0 & 1 \end{pmatrix} - \mathbf{W}_{\mathbf{k}\uparrow} \cdot \begin{pmatrix} M_{11} & M_{13} \\ M_{31} & M_{33} \end{pmatrix} \right]^{-1}, \quad (3.12)$$

and

$$\mathbf{G}_{\mathbf{k}\downarrow}(\omega) = \begin{pmatrix} M_{22} & M_{24} \\ M_{42} & M_{44} \end{pmatrix} \cdot \left[\begin{pmatrix} 1 & 0 \\ 0 & 1 \end{pmatrix} - \mathbf{W}_{\mathbf{k}\downarrow} \cdot \begin{pmatrix} M_{22} & M_{24} \\ M_{42} & M_{44} \end{pmatrix} \right]^{-1}, \quad (3.13)$$

with

$$\mathbf{W}_{\mathbf{k}\sigma} = \epsilon_{\mathbf{k}} \cdot \begin{pmatrix} 1 & -1 \\ -1 & 1 \end{pmatrix}. \quad (3.14)$$

Performing the calculations, it follows that

$$\mathbf{G}_{\mathbf{k}\uparrow}(\omega) = \frac{1}{1 - \epsilon_{\mathbf{k}}\Gamma_{13}} \left[\begin{pmatrix} M_{11} & M_{13} \\ M_{31} & M_{33} \end{pmatrix} - \epsilon_{\mathbf{k}}\Theta_{13} \begin{pmatrix} 1 & -1 \\ -1 & 1 \end{pmatrix} \right], \quad (3.15)$$

and

$$\mathbf{G}_{\mathbf{k}\downarrow}(\omega) = \frac{1}{1 - \epsilon_{\mathbf{k}}\Gamma_{24}} \left[\begin{pmatrix} M_{22} & M_{24} \\ M_{42} & M_{44} \end{pmatrix} - \epsilon_{\mathbf{k}}\Theta_{24} \begin{pmatrix} 1 & -1 \\ -1 & 1 \end{pmatrix} \right], \quad (3.16)$$

where $\Theta_{13} = M_{11}M_{33} - M_{13}M_{31}$, $\Gamma_{13} = M_{11} + M_{13} + M_{31} + M_{33}$, $\Theta_{24} = M_{22}M_{44} - M_{24}M_{42}$ and $\Gamma_{24} = M_{22} + M_{24} + M_{42} + M_{44}$. For simplicity, all the results of this work were calculated considering an uncorrelated rectangular conduction band of bandwidth 2D defined by

$$\rho_0(E_{\mathbf{k}\sigma}) = \begin{cases} \frac{1}{2D}, & \text{for } -D \leq E_{\mathbf{k}\sigma} \leq D \\ 0, & \text{otherwise} \end{cases}, \quad (3.17)$$

where the parameter 2D is roughly scaled by the bandwidth of real materials, which is approximately 1 to 5 eV. The corresponding GF is given by

$$G_\sigma^0(\omega) = \frac{1}{2D} \ln \left(\frac{\omega + D}{\omega - D} \right). \quad (3.18)$$

Integrating $\mathbf{G}_{\mathbf{k}\uparrow}(\omega)$ over the rectangular band, the total spin up Green's function $G_{\uparrow}(\omega)$ is given by

$$\begin{aligned} G_{\uparrow}(\omega) &= G_{11}(\omega) + G_{13}(\omega) + G_{31}(\omega) + G_{33}(\omega) \\ &= \frac{1}{2D} \ln \left(\frac{1 + D\Gamma_{13}}{1 - D\Gamma_{13}} \right), \end{aligned} \quad (3.19)$$

where

$$G_{11}(\omega) = \frac{\Theta_{13}}{\Gamma_{13}} + \left[M_{11} - \frac{\Theta_{13}}{\Gamma_{13}} \right] \frac{1}{2D\Gamma_{13}} \ln \left(\frac{1 + D\Gamma_{13}}{1 - D\Gamma_{13}} \right), \quad (3.20)$$

$$G_{13}(\omega) = -\frac{\Theta_{13}}{\Gamma_{13}} + \left[M_{13} + \frac{\Theta_{13}}{\Gamma_{13}} \right] \frac{1}{2D\Gamma_{13}} \ln \left(\frac{1 + D\Gamma_{13}}{1 - D\Gamma_{13}} \right), \quad (3.21)$$

$$G_{31}(\omega) = -\frac{\Theta_{13}}{\Gamma_{13}} + \left[M_{31} + \frac{\Theta_{13}}{\Gamma_{13}} \right] \frac{1}{2D\Gamma_{13}} \ln \left(\frac{1 + D\Gamma_{13}}{1 - D\Gamma_{13}} \right), \quad (3.22)$$

$$G_{33}(\omega) = \frac{\Theta_{13}}{\Gamma_{13}} + \left[M_{33} - \frac{\Theta_{13}}{\Gamma_{13}} \right] \frac{1}{2D\Gamma_{13}} \ln \left(\frac{1 + D\Gamma_{13}}{1 - D\Gamma_{13}} \right). \quad (3.23)$$

The results are analogous if the total spin down Green's function $G_{\downarrow}(\omega)$ is used instead,

$$\begin{aligned} G_{\downarrow}(\omega) &= G_{22}(\omega) + G_{24}(\omega) + G_{42}(\omega) + G_{44}(\omega) \\ &= \frac{1}{2D} \ln \left(\frac{1 + D\Gamma_{24}}{1 - D\Gamma_{24}} \right), \end{aligned} \quad (3.24)$$

where

$$G_{22}(\omega) = \frac{\Theta_{24}}{\Gamma_{24}} + \left[M_{22} - \frac{\Theta_{24}}{\Gamma_{24}} \right] \frac{1}{2D\Gamma_{24}} \ln \left(\frac{1 + D\Gamma_{24}}{1 - D\Gamma_{24}} \right), \quad (3.25)$$

$$G_{24}(\omega) = -\frac{\Theta_{24}}{\Gamma_{24}} + \left[M_{24} + \frac{\Theta_{24}}{\Gamma_{24}} \right] \frac{1}{2D\Gamma_{24}} \ln \left(\frac{1 + D\Gamma_{24}}{1 - D\Gamma_{24}} \right), \quad (3.26)$$

$$G_{42}(\omega) = -\frac{\Theta_{24}}{\Gamma_{24}} + \left[M_{42} + \frac{\Theta_{24}}{\Gamma_{24}} \right] \frac{1}{2D\Gamma_{24}} \ln \left(\frac{1 + D\Gamma_{24}}{1 - D\Gamma_{24}} \right), \quad (3.27)$$

$$G_{44}(\omega) = \frac{\Theta_{24}}{\Gamma_{24}} + \left[M_{44} - \frac{\Theta_{24}}{\Gamma_{24}} \right] \frac{1}{2D\Gamma_{24}} \ln \left(\frac{1 + D\Gamma_{24}}{1 - D\Gamma_{24}} \right). \quad (3.28)$$

The total Green's function is given by

$$G_{\sigma}(\omega) = G_{\uparrow}(\omega) + G_{\downarrow}(\omega). \quad (3.29)$$

Following the standard procedure (substituting ω by $\omega + i\eta$, taking the limit as $\eta \rightarrow 0^+$), the DOS can be written as

$$\rho_{\sigma}(\omega) = \frac{1}{\pi} \text{Im}\{G_{\sigma}(\omega)\}. \quad (3.30)$$

In principle, eq. (3.9) and all Green's functions obtained from it are exact in the infinite dimension limit. However, as the full lattice cumulants $\mathbf{M}_{\sigma}(\omega)$, eq. (3.10), are unknown, the atomic cumulants $\mathbf{m}_{\sigma}^{\text{at}}(\omega)$ obtained from eq. (3.8) as the solution of a cluster containing N correlated sites are used as approximations for $\mathbf{M}_{\sigma}(\omega)$ to calculate the Green's functions for the lattice, equations (3.19) to (3.29). The method shows its full potential here because we can use exact diagonalization to solve an increasing cluster of Hubbard correlated sites, and from these solutions, it is possible to build better approximations that are increasingly closer to the exact solution of the problem.

The cluster solutions satisfy the completeness relation per spin of the Hubbard model given by

$$comp^\sigma = n_{vac}^\sigma + n_{up}^\sigma + n_{down}^\sigma + n_d^\sigma = 1, \quad (3.31)$$

where $\sigma = (\uparrow; \downarrow)$, with $\sigma = \uparrow$ representing the transitions associated with $I_x = 1, 3$, and $\sigma = \downarrow$ those associated with $I_x = 2, 4$ (see Table 3.1). The first term of the sum is the vacuum occupation number, the second and third terms are the spin up and spin down occupation numbers, respectively, and the last term is the double occupation number. The different averages can be calculated employing the Green's functions $G_{11}(\omega)$ and $G_{33}(\omega)$, associated with the processes $I_x = 1, 3$, defined by eqs. (3.20) and (3.23):

$$n_{vac}^\uparrow = \left(\frac{1}{\pi}\right) \int_{-\infty}^{\infty} d\omega \text{Im}(G_{11})(1 - n_F), \quad (3.32)$$

$$n_{up}^\uparrow = \left(\frac{1}{\pi}\right) \int_{-\infty}^{\infty} d\omega \text{Im}(G_{11})n_F, \quad (3.33)$$

$$n_{down}^\uparrow = \left(\frac{1}{\pi}\right) \int_{-\infty}^{\infty} d\omega \text{Im}(G_{33})(1 - n_F), \quad (3.34)$$

$$n_d^\uparrow = \left(\frac{1}{\pi}\right) \int_{-\infty}^{\infty} d\omega \text{Im}(G_{33})n_F, \quad (3.35)$$

where $n_F(x) = 1/[1 + \exp(\beta x)]$ is the Fermi-Dirac distribution. Similarly, we can employ the Green's functions G_{22} and G_{44} , associated with the processes $I_x = 2, 4$, defined by eqs. (3.25) and (3.28) to calculate the corresponding occupation numbers:

$$n_{vac}^\downarrow = \left(\frac{1}{\pi}\right) \int_{-\infty}^{\infty} d\omega \text{Im}(G_{22})(1 - n_F), \quad (3.36)$$

$$n_{down}^\downarrow = \left(\frac{1}{\pi}\right) \int_{-\infty}^{\infty} d\omega \text{Im}(G_{22})n_F, \quad (3.37)$$

$$n_{up}^\downarrow = \left(\frac{1}{\pi}\right) \int_{-\infty}^{\infty} d\omega \text{Im}(G_{44})(1 - n_F), \quad (3.38)$$

$$n_d^\downarrow = \left(\frac{1}{\pi}\right) \int_{-\infty}^{\infty} d\omega \text{Im}(G_{44})n_F. \quad (3.39)$$

The completeness relation and the full occupation numbers are then

$$comp = (comp^\uparrow + comp^\downarrow)/2, \quad (3.40)$$

$$n_{vac} = (n_{vac}^\uparrow + n_{vac}^\downarrow)/2, \quad (3.41)$$

$$n_{up} = (n_{up}^\uparrow + n_{up}^\downarrow)/2, \quad (3.42)$$

$$n_{down} = (n_{down}^\uparrow + n_{down}^\downarrow)/2, \quad (3.43)$$

$$n_d = (n_d^\uparrow + n_d^\downarrow)/2. \quad (3.44)$$

The electron density per lattice site n (electron concentration or band filling) is defined as

$$n = \frac{N_e}{N} = n_{up} + n_{down} + 2n_d, \quad (3.45)$$

where N_e is the number of electrons and N is the number of sites. The factor 2 in front of n_d refers to the number of electrons inside of the double occupied state. The maximum number of electrons per site is $n = 2$, and the limiting cases $n = 0$ and $n = 1$ correspond to empty and half-filled bands, respectively.

Once the occupation numbers were calculated, the ground-state energy for the lattice $E_g(U)$ of the single-band Hubbard Hamiltonian (2.1) can be obtained. In general, it is given by [55]

$$E_g(U) = E_g(U = 0) + \int_0^U \sum_i \langle n_{i\uparrow} n_{i\downarrow} \rangle_{U'} dU', \quad (3.46)$$

where $E_g(U = 0)$ is the ground-state energy for the lattice of the noninteracting system, and the term $\langle n_{i\uparrow} n_{i\downarrow} \rangle_{U'}$ is the average occupation number of doubly occupied states at interaction strength U' . The noninteracting ground-state energy was calculated in a previous section (equation(2.60)) and is equal to

$$E_g(U = 0) = \int_{-\pi/2}^{\pi/2} dk \frac{1}{2\pi} 2(-2t \cos k) = -\frac{4t}{\pi}. \quad (3.47)$$

Therefore, the ground-state energy for the lattice $E_g(U)$ becomes

$$E_g(U) = -\frac{4t}{\pi} + \int_0^U \sum_i \langle n_{i\uparrow} n_{i\downarrow} \rangle_{U'} dU'. \quad (3.48)$$

The term $\langle n_{i\uparrow} n_{i\downarrow} \rangle_{U'}$ can be calculated by means of the CGFM, using equations (3.35), (3.39), and (3.44). Thus, the ground-state energy for the lattice is:

$$E_g(U) = -\frac{4t}{\pi} + \int_0^U n_d(U') dU'. \quad (3.49)$$

3.2 The numerical code

To implement the CGFM for the single-band one-dimensional Hubbard model, a numerical code has been developed in a joint effort using standard Fortran 95. It was the most time-consuming part of the work. The complexity of the code resides in the calculation and treatment of the large number of residues $r_{i,\sigma}$ resulting from the method and using them to calculate the atomic Green's functions, equation (3.6). The code was prepared to work for any temperature and any parameter range of the model, and we intend to make it available to the general public in the future.

The starting point is to define the states (and operators) for a single site (a monomer). Using Dirac notation, the possible states for the monomer are $|\downarrow\rangle$, $|0\rangle$, $|\uparrow\downarrow\rangle$, and $|\uparrow\rangle$, where we will define that $|\uparrow\downarrow\rangle = c_{\uparrow}^{\dagger} c_{\downarrow}^{\dagger} |0\rangle$ and, therefore, $c_{\downarrow}^{\dagger} |\uparrow\rangle = -|\uparrow\downarrow\rangle$. Using these four states, we can define the initial Hamiltonian as a diagonal 4x4 matrix that has the following increasing quantum numbers for spin S_z and number of particles n ($S_z; n$):

$$\begin{array}{c} \langle \downarrow | \\ \langle 0 | \\ \langle \uparrow\downarrow | \\ \langle \uparrow | \end{array} \begin{pmatrix} |\downarrow\rangle & |0\rangle & |\uparrow\downarrow\rangle & |\uparrow\rangle \\ \left(-\frac{1}{2}; 1 \right) & & & \\ & (0; 0) & & \\ & & (0; 2) & \\ & & & \left(\frac{1}{2}; 1 \right) \end{pmatrix}. \quad (3.50)$$

The operators c_{\uparrow}^{\dagger} , c_{\downarrow}^{\dagger} , $n_{\uparrow} n_{\downarrow}$, $m = n_{\uparrow} - n_{\downarrow}$, and $n_{\uparrow} + n_{\downarrow}$ are also 4x4 matrices defined as

$$c_{\uparrow}^{\dagger} = \begin{array}{c} | \downarrow \rangle \\ | 0 \rangle \\ \langle \uparrow \downarrow | \\ \langle \uparrow | \end{array} \begin{array}{c} | \downarrow \rangle \\ | 0 \rangle \\ | \uparrow \downarrow \rangle \\ | \uparrow \rangle \end{array} \begin{pmatrix} 0 & 0 & 0 & 0 \\ 0 & 0 & 0 & 0 \\ 1 & 0 & 0 & 0 \\ 0 & 1 & 0 & 0 \end{pmatrix} ; \quad c_{\downarrow}^{\dagger} = \begin{array}{c} | \downarrow \rangle \\ | 0 \rangle \\ \langle \uparrow \downarrow | \\ \langle \uparrow | \end{array} \begin{array}{c} | \downarrow \rangle \\ | 0 \rangle \\ | \uparrow \downarrow \rangle \\ | \uparrow \rangle \end{array} \begin{pmatrix} 0 & 1 & 0 & 0 \\ 0 & 0 & 0 & 0 \\ 0 & 0 & 0 & -1 \\ 0 & 0 & 0 & 0 \end{pmatrix} ; \quad (3.51)$$

$$n_{\uparrow} n_{\downarrow} = \begin{array}{c} | \downarrow \rangle \\ | 0 \rangle \\ \langle \uparrow \downarrow | \\ \langle \uparrow | \end{array} \begin{array}{c} | \downarrow \rangle \\ | 0 \rangle \\ | \uparrow \downarrow \rangle \\ | \uparrow \rangle \end{array} \begin{pmatrix} 0 & 0 & 0 & 0 \\ 0 & 0 & 0 & 0 \\ 0 & 0 & 1 & 0 \\ 0 & 0 & 0 & 0 \end{pmatrix} ; \quad m = \begin{array}{c} | \downarrow \rangle \\ | 0 \rangle \\ \langle \uparrow \downarrow | \\ \langle \uparrow | \end{array} \begin{array}{c} | \downarrow \rangle \\ | 0 \rangle \\ | \uparrow \downarrow \rangle \\ | \uparrow \rangle \end{array} \begin{pmatrix} -1 & 0 & 0 & 0 \\ 0 & 0 & 0 & 0 \\ 0 & 0 & 0 & 0 \\ 0 & 0 & 0 & 1 \end{pmatrix} ; \quad (3.52)$$

$$n_{\uparrow} + n_{\downarrow} = \begin{array}{c} | \downarrow \rangle \\ | 0 \rangle \\ \langle \uparrow \downarrow | \\ \langle \uparrow | \end{array} \begin{array}{c} | \downarrow \rangle \\ | 0 \rangle \\ | \uparrow \downarrow \rangle \\ | \uparrow \rangle \end{array} \begin{pmatrix} 1 & 0 & 0 & 0 \\ 0 & 0 & 0 & 0 \\ 0 & 0 & 2 & 0 \\ 0 & 0 & 0 & 1 \end{pmatrix} . \quad (3.53)$$

We can perform the expansion of the vector space (and the operators) by performing tensor products between two single-site states (and operators). It will generate the states (and the operators) for two sites. By performing tensor products between two-site states (and operators) and single-site states (and operators) we can generate the three-site vector space (and operators). We must continue performing the tensor products of the previous states (and operators) with single-site states (and operators) up to the point where the space (and the operators) have the appropriate dimension for the number of correlated sites N used as parameter. After each expansion of the vector space, the states are organized by increasing S_z and, then, n , as in the first step. It is important to keep track of the quantum numbers, as they will be used later to identify the possible transitions of the cluster.

The next step is to calculate the elements of the Hamiltonian, using the operators calculated in the previous step:

$$H = \epsilon_0(n_{\uparrow} + n_{\downarrow}) - h(m) + \frac{U}{2}(n_{\uparrow}n_{\downarrow} + n_{\downarrow}n_{\uparrow}) - t(c_{\uparrow}^{\dagger}c_{\uparrow} + c_{\downarrow}^{\dagger}c_{\downarrow}), \quad (3.54)$$

where the matrix operators are calculated for the appropriate sites and ϵ_0 , h , $\frac{U}{2}$, and t are the input parameters along the number of sites N . The result is a $4^N \times 4^N$ matrix that presents itself in block diagonal form as consequence of organizing the states and operators using quantum numbers S_z and n .

After the Hamiltonian has been constructed in its matrix form, we employ the routine DSYEVR from the Linear Algebra PACKage (LAPACK) to diagonalize it. Up to this point, this is the standard procedure for exact diagonalization methods. The following steps differentiate the code from standard ED as a consequence of the novel method developed.

From the diagonalization of the Hamiltonian, a series of eigenstates with their respective eigenvalues and quantum numbers S_z and n are obtained. Due to the selection rules regarding the number of particles and spin, to calculate the atomic residues $r_{i,\sigma}$ given in equations (3.5) and (3.6), one does not need to calculate every possible transition from state i to j , since only transitions that increase or decrease the number of particles by one and the spin by half are allowed. Other than that, transitions that change the number of particles by creating or destroying a spin down electron are separated from transitions that do so by creating or destroying a spin up electron, as indicated in equation (3.5). Indexing and separating states using the quantum numbers facilitates the task of identifying blocks of the Hamiltonian that have states that can transition to other blocks. For the monomer, for example, equation (3.50), the state in the second block can transition to the states in the first and fourth blocks, while the states in the first and fourth blocks can only transition to the state in the third block. Besides that, the transition from the state in the second block to the state in the first block creates a spin down electron, while the transition to the state in the fourth block creates a spin up electron and these transitions are separated.

Once the spin up and spin down residues have been calculated, the spin up and spin down atomic Green's functions, equation (3.7), can be calculated using the energy differences $u_{i,\sigma}$ associated with the residues. From the atomic GF, the atomic cumulants, equation (3.8), are obtained. The atomic cumulants are used as approximations for the full cumulants to calculate the GF for the lattice using equation (3.29). Using the GF for the lattice, the properties of the model, such as the density of states, single-particle gap, occupation numbers, and ground-state energy can be calculated by the subroutines.

The simplified general structure of the numerical code can be found below:

PROGRAM AMHUBBARD

GROUND

calculates the ground-state energy using the CGFM, from equation (3.49)

DENSI

calculates the GF for the lattice, DOS, and gap using the CGFM, from equations (3.19) to (3.30)

ATOMIC

calculates the atomic solution

STRUCTURE

constructs the vector space and operators by iteratively adding correlated sites

HAM

calculates the Hamiltonian in matrix form and diagonalizes it using the routine DSYEVR

RESIDUES

calculates the spin up and spin down residues, from equation (3.6)

GREEN

calculates the atomic GF and atomic cumulants, from equations (3.5) and (3.8)

OCCUP

calculates the occupation numbers using the CGFM, from equations (3.32) to (3.39)

END PROGRAM

Table 3.2: Execution times and RAM usage by the code (time / RAM) when run in the workstation mentioned in section 3.2.

N	Single-particle gap (single data point)	Occupation numbers (six data points)	Ground-state energy (single data point)
6	3 s / 0.07 GB	5 s / 0.11 GB	2 min 2 s / 2.40 GB
7	2 min 50 s / 1.00 GB	5 min 42 s / 2.00 GB	3 h 28 min / 53.50 GB
8	2 h 10 min / 7.15 GB	10 h 20 min / 40.00 GB	-
9	12 d / 150 GB	-	-

The dash represents calculations that were not made in this work due to computational limitations.

The code runs very quickly and requires very little amount of RAM for $N = 2, 3, 4, 5$ and can be run on any modern desktop or laptop. It is advised to use a workstation for $N = 6$, and it is necessary for $N = 7$ or greater. The workstation used in this work has the following specifications:

- Motherboard: ASUS PRIME TRX40-PRO;
- Processor: AMD Ryzen Threadripper 3960X 24-Core (48 threads) 3.8 GHz (4.5 GHz Boost);
- RAM: 192 GB (6 x 32 GB DIMMs) (188.6 GB usable) ECC DDR4 3200 Mhz;
- Storage: Samsung 970 EVO Plus 1 TB NVMe SSD (PCIe Gen 3.0 x4);
- OS: Ubuntu 20.04.2 LTS with GFortran, LAPACK, and BLAS packages and 238.4 GB of SWAP.

A few actions were taken to speed up execution time: subroutines GROUND and OCCUP were turned off to calculate the gap; the spin down solution was turned off to calculate the gap, n_d , and E_g for $h = 0$ and $\mu = 0$, since they are identical for spin up and spin down; only $\mu \leq 0$ was explicitly considered because the occupation numbers are symmetrical, $n_{up}(-\mu) = n_{up}(\mu)$, $n_{down}(-\mu) = n_{down}(\mu)$, $n_{vac}(-\mu) = n_d(\mu)$, $n_d(-\mu) = n_{vac}(\mu)$. The execution times and RAM usage by the code can be found in table 3.2 for a single data point in the case of the single-particle gap and the ground-state energy, and for six simultaneous data points for the six occupation numbers (n_{vac} , n_{up} , n_{down} , n_d , $comp$, and n).

Each graph for the occupation numbers at a certain magnetic field defines a horizontal slice of the phase diagram, as they show the values of chemical potential where the system transitions between phases. However, we do not need to calculate the whole occupation number graphs to obtain the phase diagram because we know that the boundaries of the phase diagram are located in a small interval of chemical potential near the TBA result. This reduces the amount of data points that need to be calculated and, therefore, the time to get the full phase diagram. To get the phase diagrams for $N = 7$ and $N = 8$, for instance, we calculated a set of five data points around a specific chemical potential of the TBA result for the six occupation numbers to obtain each data point for the phase diagram. These results are independent of each other, and several data points can be calculated at the same time. Each data point in the phase diagram takes approximately 29 minutes for $N = 7$, and approximately 52 hours for $N = 8$.

3.3 Using the Hubbard monomer as a “seed”

First, we will apply the cumulant Green’s functions method to the atomic limit of the Hubbard model at zero magnetic field and use it as the “seed” for the cumulant expansion. This is useful to better understand how the method works. Using this limit, we will analyze how the solution changes as more sites are added.

Using Dirac notation, the possible states for the monomer are $|0\rangle$, $|\uparrow\rangle$, $|\downarrow\rangle$ and $|\uparrow\downarrow\rangle$. The states of the system can be seen in table 3.3 alongside their energies. Using this information, we identify the possible transitions of the system and the energies associated with them, which can be seen in table 3.4. In addition to this, we also separate the Green’s functions according to the S_z component of the total spin that is modified in the transitions, as summarized in table 3.1. Therefore, we can write the atomic Green’s functions for the monomer in the same way as the equation (3.7), but the components g_{13} , g_{31} , g_{24} and g_{42} are zero. Then, it follows that:

$$g_{\sigma}^{at}(\omega) = \begin{pmatrix} g_{11} & 0 & 0 & 0 \\ 0 & g_{33} & 0 & 0 \\ 0 & 0 & g_{22} & 0 \\ 0 & 0 & 0 & g_{44} \end{pmatrix}, \quad (3.55)$$

where the Green’s functions g^{at} follow the same definition as equations (3.5) and (3.6). Employing the cumulant expansion, we obtain for spin up

$$\begin{aligned} m_{11} &= g_{11}; \\ m_{13} &= 0; \\ m_{31} &= 0; \\ m_{33} &= g_{33}; \end{aligned} \quad (3.56)$$

and the Green’s functions for the lattice become

$$G_{\uparrow}(\omega) = \frac{1}{2D} \ln \left(\frac{1 + D\Gamma_{13}}{1 - D\Gamma_{13}} \right), \quad (3.57)$$

where $\Gamma_{13} = m_{11} + m_{33}$. The calculations are analogous for spin down.

Figure 3.4 shows the density of states for two example electronic correlations for this solution with $t = 1$. It is worth noting that the particle-hole symmetry was recovered and that the gap increases as the electronic correlation U increases.

Table 3.3: Exact solution of the Hubbard model for the monomer.

State	Eigenvector $ n, r\rangle$	Eigenvalue E_i	n	S_z
1 = $ 0\rangle$	$ 0, 1\rangle = 0\rangle$	$E_1 = 0$	0	0
2 = $ \uparrow\rangle$	$ 1, 1\rangle = \uparrow\rangle$	$E_2 = \epsilon_0$	1	$\frac{1}{2}$
3 = $ \downarrow\rangle$	$ 1, 2\rangle = \downarrow\rangle$	$E_3 = \epsilon_0$	1	$-\frac{1}{2}$
4 = $ \uparrow\downarrow\rangle$	$ 2, 1\rangle = \uparrow\downarrow\rangle$	$E_4 = 2\epsilon_0 + U$	2	0

The four eigenvectors $|n, r\rangle$ have energies E_i ; where n is the number of electrons, r is the state of the monomer with n electrons, and S_z is the component of the total spin in the z direction.

Table 3.4: Energy differences of the possible transitions of the Hubbard monomer.

Energy difference	Transition
$u_1 = \epsilon_0$	$E_{1,2} = E_{1,3}$
$u_2 = \epsilon_0 + U$	$E_{2,4} = E_{3,4}$

Energy differences of the possible transitions of the Hubbard monomer, where $E_{i,j}$ represents the transition from state i to state j .

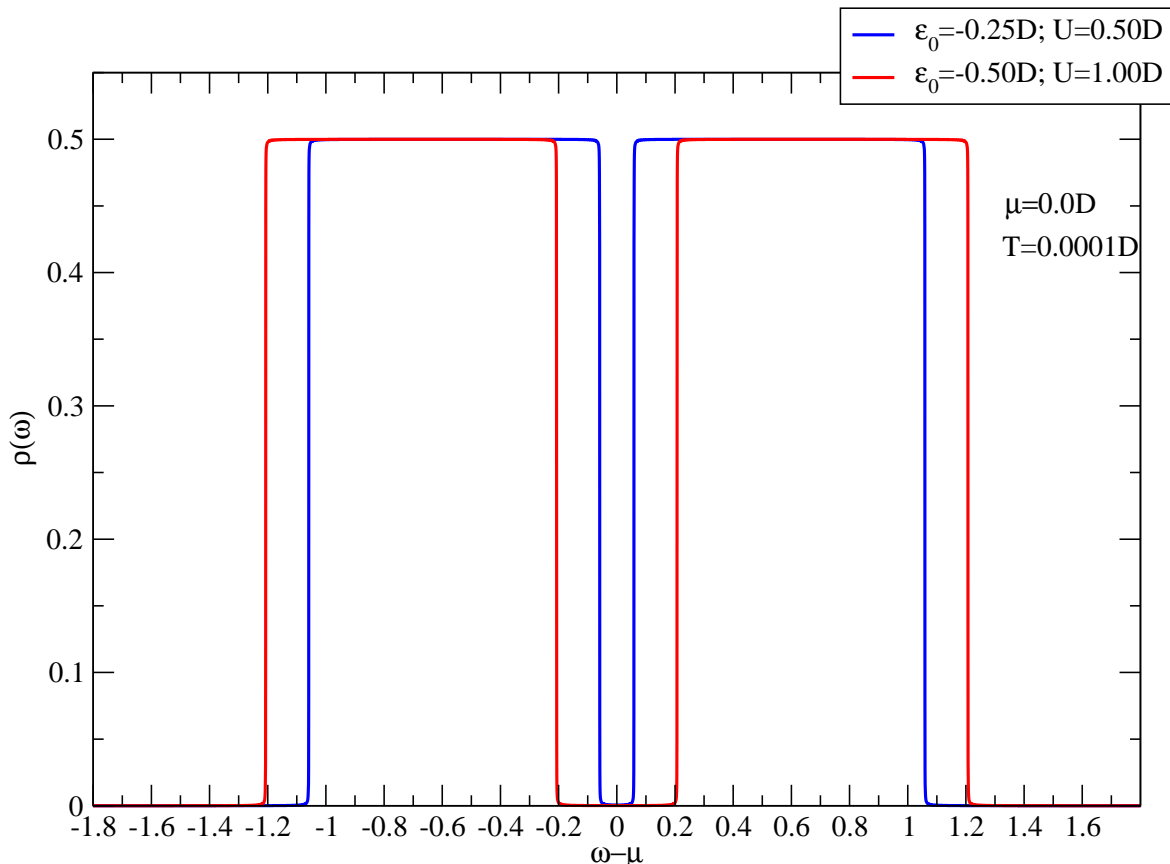


Figure 3.4: Density of states ρ as a function of the frequency $\omega - \mu$ for the half-filling limit, $\epsilon_0 = -U/2$, $\mu = 0$, for the CGFM for some representative values of ϵ_0 and U using the monomer.

3.4 Using the Hubbard dimer as a “seed”

In this section, the Hubbard model for two sites, also known as the Hubbard molecule or the Hubbard dimer, is studied at zero magnetic field. This problem deals with a non-trivial interacting electronic system that has an exact analytical solution. The Hamiltonian used to model this problem is:

$$H = \epsilon_0 \sum_{i=1,2} \sum_{\sigma} c_{i\sigma}^{\dagger} c_{i\sigma} - t \sum_{\substack{i \neq j \\ i,j=1,2}} \sum_{\sigma} c_{i\sigma}^{\dagger} c_{j\sigma} + \frac{U}{2} \sum_{i=1,2} \sum_{\sigma\sigma'} c_{i\sigma}^{\dagger} c_{i\sigma'}^{\dagger} c_{i\sigma'} c_{i\sigma}, \quad (3.58)$$

where t is the hopping; 1 and 2 denote the sites; σ and σ' represent spin up (σ or \uparrow) and spin down ($\bar{\sigma}$ or \downarrow); U denotes the Coulombian interaction between electrons at the same site; ϵ_0 is the local energy of an electron; c and c^{\dagger} are the annihilation and creation operators, respectively.

Performing the summations over all indexes, the Hamiltonian becomes:

$$\begin{aligned}
H = & -tc_{1\sigma}^\dagger c_{2\sigma} - tc_{1\bar{\sigma}}^\dagger c_{2\bar{\sigma}} - tc_{2\sigma}^\dagger c_{1\sigma} - tc_{2\bar{\sigma}}^\dagger c_{1\bar{\sigma}} + \\
& + Uc_{1\sigma}^\dagger c_{1\bar{\sigma}}^\dagger c_{1\bar{\sigma}} c_{1\sigma} + Uc_{2\sigma}^\dagger c_{2\bar{\sigma}}^\dagger c_{2\bar{\sigma}} c_{2\sigma} + \\
& + \epsilon_0 c_{1\sigma}^\dagger c_{1\sigma} + \epsilon_0 c_{2\sigma}^\dagger c_{2\sigma} + \epsilon_0 c_{1\bar{\sigma}}^\dagger c_{1\bar{\sigma}} + \epsilon_0 c_{2\bar{\sigma}}^\dagger c_{2\bar{\sigma}}.
\end{aligned} \tag{3.59}$$

Using Dirac notation, the possible states of sites 1 and 2 are $|0\rangle$, $|\uparrow\rangle$, $|\downarrow\rangle$ and $|\uparrow\downarrow\rangle$. Therefore, when treating two sites, the following Fock space is generated:

States containing 0 electron: $|0, 0\rangle$.

States containing 1 electron: $|\uparrow, 0\rangle; |0, \uparrow\rangle; |\downarrow, 0\rangle; |0, \downarrow\rangle$.

States containing 2 electrons: $|\uparrow, \uparrow\rangle; |\downarrow, \downarrow\rangle; |\uparrow, \downarrow\rangle; |\downarrow, \uparrow\rangle; |\uparrow\downarrow, 0\rangle; |0, \uparrow\downarrow\rangle$.

States containing 3 electrons: $|\uparrow, \uparrow\downarrow\rangle; |\uparrow\downarrow, \uparrow\rangle; |\downarrow, \uparrow\downarrow\rangle; |\uparrow\downarrow, \downarrow\rangle$.

States containing 4 electrons: $|\uparrow\downarrow, \uparrow\downarrow\rangle$.

Projecting the Hamiltonian given in equation (3.59) in the Fock space above, the matrix elements are calculated as follows:

$$H_{mn} = \langle \psi_m | H | \psi_n \rangle, \tag{3.60}$$

where ψ_m and ψ_n represent the states of the dimer and H is the Hamiltonian operator given in (3.59). This procedure gives rise to a 16 x 16 matrix that has a block diagonal structure originating from the conservation of the spin in the z direction S_z for a given number of particles n , facilitating the diagonalization process. The matrix blocks obtained from the calculation of the matrix elements are:

Block for states with 0 electron:

$$\begin{pmatrix} 0 \end{pmatrix}.$$

Block for states with 1 electron:

$$\begin{pmatrix} \epsilon_0 & -t & 0 & 0 \\ -t & \epsilon_0 & 0 & 0 \\ 0 & 0 & \epsilon_0 & -t \\ 0 & 0 & -t & \epsilon_0 \end{pmatrix}.$$

Block for states with 2 electrons:

$$\begin{pmatrix} 2\epsilon_0 & 0 & 0 & 0 & 0 & 0 \\ 0 & 2\epsilon_0 & 0 & 0 & 0 & 0 \\ 0 & 0 & 2\epsilon_0 & 0 & -t & -t \\ 0 & 0 & 0 & 2\epsilon_0 & t & t \\ 0 & 0 & -t & t & 2\epsilon_0 + U & 0 \\ 0 & 0 & -t & t & 0 & 2\epsilon_0 + U \end{pmatrix}.$$

Block for states with 3 electrons:

$$\begin{pmatrix} 3\epsilon_0 + U & -t & 0 & 0 \\ -t & 3\epsilon_0 + U & 0 & 0 \\ 0 & 0 & 3\epsilon_0 + U & -t \\ 0 & 0 & -t & 3\epsilon_0 + U \end{pmatrix}.$$

Block for states with 4 electrons:

$$\begin{pmatrix} 4\epsilon_0 + 2U \end{pmatrix}.$$

Table 3.5: Exact diagonalization of the Hubbard Hamiltonian for the dimer.

States	Eigenvectors $ n, r\rangle$	Eigenvalues E_i	n	S_z
1 = $ 0, 0\rangle$	$ 0, 1\rangle = 0, 0\rangle$	$E_1 = 0$	0	0
2 = $ \uparrow, 0\rangle$	$ 1, 1\rangle = \frac{1}{\sqrt{2}} (\uparrow, 0\rangle - 0, \uparrow\rangle)$	$E_2 = \epsilon_0 + t$	1	$+\frac{1}{2}$
3 = $ \downarrow, 0\rangle$	$ 1, 2\rangle = \frac{1}{\sqrt{2}} (\downarrow, 0\rangle - 0, \downarrow\rangle)$	$E_3 = \epsilon_0 + t$	1	$-\frac{1}{2}$
4 = $ 0, \uparrow\rangle$	$ 1, 3\rangle = \frac{1}{\sqrt{2}} (\uparrow, 0\rangle + 0, \uparrow\rangle)$	$E_4 = \epsilon_0 - t$	1	$+\frac{1}{2}$
5 = $ 0, \downarrow\rangle$	$ 1, 4\rangle = \frac{1}{\sqrt{2}} (\downarrow, 0\rangle + 0, \downarrow\rangle)$	$E_5 = \epsilon_0 - t$	1	$-\frac{1}{2}$
6 = $ \uparrow, \uparrow\rangle$	$ 2, 1\rangle = \uparrow, \uparrow\rangle$	$E_6 = 2\epsilon_0$	2	+1
7 = $ \downarrow, \downarrow\rangle$	$ 2, 2\rangle = \downarrow, \downarrow\rangle$	$E_7 = 2\epsilon_0$	2	-1
8 = $ \uparrow, \downarrow\rangle$	$ 2, 3\rangle = \frac{1}{\sqrt{2}} (\uparrow, \downarrow\rangle + \downarrow, \uparrow\rangle)$	$E_8 = 2\epsilon_0$	2	0
9 = $ \downarrow, \uparrow\rangle$	$ 2, 4\rangle = \frac{1}{\sqrt{2}} (0, \uparrow\downarrow\rangle - \uparrow\downarrow, 0\rangle)$	$E_9 = 2\epsilon_0 + U$	2	0
10 = $ \uparrow\downarrow, 0\rangle$	$ 2, 5\rangle = \frac{1}{b} (0, \uparrow\downarrow\rangle + \uparrow\downarrow, 0\rangle) + \frac{4t}{b(c+U)} (\downarrow, \uparrow\rangle - \uparrow, \downarrow\rangle)$	$E_{10} = 2\epsilon_0 + \frac{U+c}{2}$	2	0
11 = $ 0, \uparrow\downarrow\rangle$	$ 2, 6\rangle = \frac{1}{a} (0, \uparrow\downarrow\rangle + \uparrow\downarrow, 0\rangle) + \frac{4t}{a(c-U)} (\uparrow, \downarrow\rangle - \downarrow, \uparrow\rangle)$	$E_{11} = 2\epsilon_0 + \frac{U-c}{2}$	2	0
12 = $ \uparrow\downarrow, \uparrow\rangle$	$ 3, 1\rangle = \frac{1}{\sqrt{2}} (\uparrow, \uparrow\downarrow\rangle + \uparrow\downarrow, \uparrow\rangle)$	$E_{12} = 3\epsilon_0 + U - t$	3	$+\frac{1}{2}$
13 = $ \uparrow\downarrow, \downarrow\rangle$	$ 3, 2\rangle = \frac{1}{\sqrt{2}} (\downarrow, \uparrow\downarrow\rangle + \uparrow\downarrow, \downarrow\rangle)$	$E_{13} = 3\epsilon_0 + U - t$	3	$-\frac{1}{2}$
14 = $ \uparrow, \uparrow\downarrow\rangle$	$ 3, 3\rangle = \frac{1}{\sqrt{2}} (\uparrow, \uparrow\downarrow\rangle - \uparrow\downarrow, \uparrow\rangle)$	$E_{14} = 3\epsilon_0 + U + t$	3	$+\frac{1}{2}$
15 = $ \downarrow, \uparrow\downarrow\rangle$	$ 3, 4\rangle = \frac{1}{\sqrt{2}} (\downarrow, \uparrow\downarrow\rangle - \uparrow\downarrow, \downarrow\rangle)$	$E_{15} = 3\epsilon_0 + U + t$	3	$-\frac{1}{2}$
16 = $ \uparrow\downarrow, \uparrow\downarrow\rangle$	$ 4, 1\rangle = \uparrow\downarrow, \uparrow\downarrow\rangle$	$E_{16} = 4\epsilon_0 + 2U$	4	0

The sixteen eigenvectors $|n, r\rangle$ have energies E_i ; where n is the number of electrons, r is the index of the state with n electrons and S_z is the spin in the z direction. The abbreviations $a = \sqrt{2 \left(\left(\frac{16t^2}{(c-U)^2} \right) + 1 \right)}$, $b = \sqrt{2 \left(\left(\frac{16t^2}{(c+U)^2} \right) + 1 \right)}$ and $c = \sqrt{16t^2 + U^2}$ were used.

Next, the eigenvectors and eigenvalues of the matrix blocks were calculated, as well as the number of particles n and the spin in the z -direction S_z for each state. The results can be found in table 3.5.

Using the data presented in table 3.5, all possible transitions of the dimer were identified and the atomic Green's functions residues $r_{i,\sigma}$ along with their respective energy differences $u_{i,\sigma}$ were calculated. They can be found in appendix A.

With this data at hand, the procedure described in chapter 3 can be followed to obtain the atomic Green's functions. After that, the procedure to calculate the Green's functions for the lattice and to calculate the dynamic properties of the model can be followed.

Figure 3.5 shows the density of states for two example electronic correlations for this solution with $t = 1$. It is worth noting that the particle-hole symmetry was recovered and that the gap increases as the electronic correlation U increases. The resulting particle-hole symmetry of the DOS for $\mu = 0$ is a feature of the model not recovered by the Hubbard I approximation, as shown in section 2.2, and is a strong result of the CGFM. It can also be seen that, because of the small number of sites used, there is a strong atomic signature in the resulting DOS.

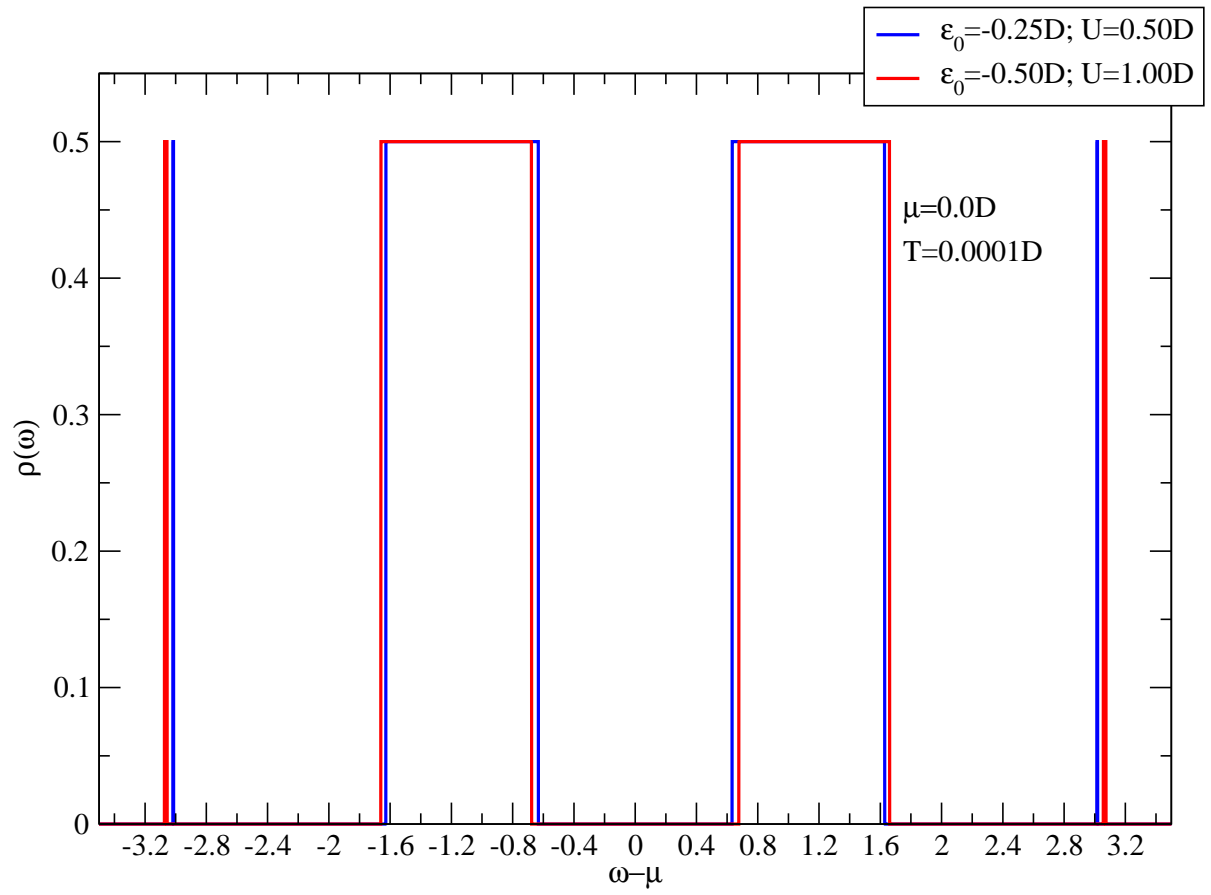


Figure 3.5: Density of states ρ as a function of the frequency $\omega - \mu$ for the half-filling limit, $\epsilon_0 = -U/2$, $\mu = 0$, for the CGFM for some representative values of ϵ_0 and U using the dimer.

Chapter 4

Results and discussion for larger clusters

4.1 Zero magnetic field

In the following results, we use the temperature $T = 0.0001D$, correlation $U = 4D$, magnetic field $h = 0$, and cluster hopping $t = 1$ unless written otherwise. As stated previously, $2D \approx 1$ to 5 eV. Since $1 \text{ eV} \approx 11605 \text{ K}$, $T = 0.0001D \approx 0.6$ to 3 K . To connect the energy scale of the calculations to the scale of real systems, we could take advantage of some physical properties of the model, such as maxima in specific heat or susceptibilities or minimum in thermopower. In Fig. 4.1 we represent the residues $r_{i,up}$ of the total atomic GF $g_{up}^{at} = g_{11} + g_{13} + g_{31} + g_{33}$ as functions of the transition energies $u_{i,up}$ for the half-filled limit, $\epsilon_0 = -U/2$, $\mu = 0$, and $N = 2, 3, 4, 5, 6, 7$. The residues exhibit the characteristic mirror symmetry of the one-dimensional Hubbard model [24]. The striking point here is that as the cluster size increases, the number of atomic residues increases very rapidly (for $N = 2$, we have 4 $r_{i,up}$; for $N = 3$, 8 $r_{i,up}$; for $N = 4$, 32 $r_{i,up}$; and for $N = 7$, 1322 $r_{i,up}$) while their weight decreases very rapidly. It is worth pointing out that the clusters containing $N = 7$ or $N = 8$ correlated sites present the best benefit-cost ratio.

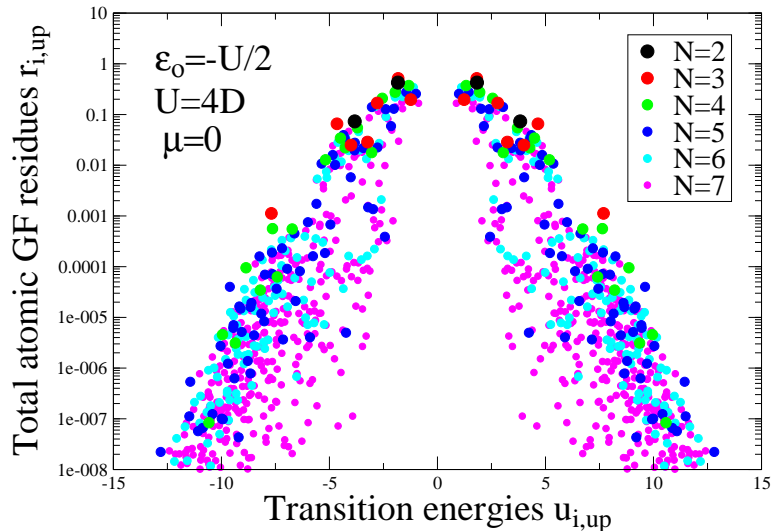


Figure 4.1: Numerical value of the residues $r_{i,up}$ of the total atomic GF $g_{up}^{at} = g_{11} + g_{13} + g_{31} + g_{33}$ as functions of the transition energies $u_{i,up}$ for the CGFM for some representative values of $N = 2, 3, 4, 5, 6, 7$.

Table 4.1: Number of correlated sites N , atomic cluster ground-state energy per site GSE/N , total cluster spin in the z direction S_z , and charge Q of the atomic cluster employed in the calculations at half-filling. For odd N , the GSE/N is two-fold degenerated, corresponding to two spin orientations $\pm 1/2$.

N	2	3	4	5	6	7	8	9
GSE/N	-2.415	-2.413	-2.488	-2.484	-2.515	-2.511	-2.530	-2.527
S_z	0	$\pm 1/2$						
Q	2	3	4	5	6	7	8	9

For even N , the total cluster spin is $S_z = 0$, and the atomic cluster ground-state is nondegenerate; whereas for odd N , $S_z = \pm 1/2$ and the GSE/N is double-degenerate as indicated in Table 4.1. Even though clusters with even and odd N have different properties, the GSE/N present an unusual behaviour; they are close together in pairs (2, 3; 4, 5; 6, 7; and 8, 9) and converge in pairs as N increases. Both cluster solutions, when used as “seeds” to generate the Green’s functions for the lattice, are consistent with the Lieb theorem [56], the GSE/N of the model are nondegenerate apart from the trivial spin degeneracy and have a total spin $S_{tot} = ||S_{z,up}| - |S_{z,down}||$. It should be noted that the ground-state of the cluster does not directly determine the properties of the corresponding infinite system. The cumulants obtained from the clusters of correlated sites are used in the CGFM as bricks to construct the infinite system that can exhibit properties not present in the cluster, such as long-range magnetic order or even superconductivity.

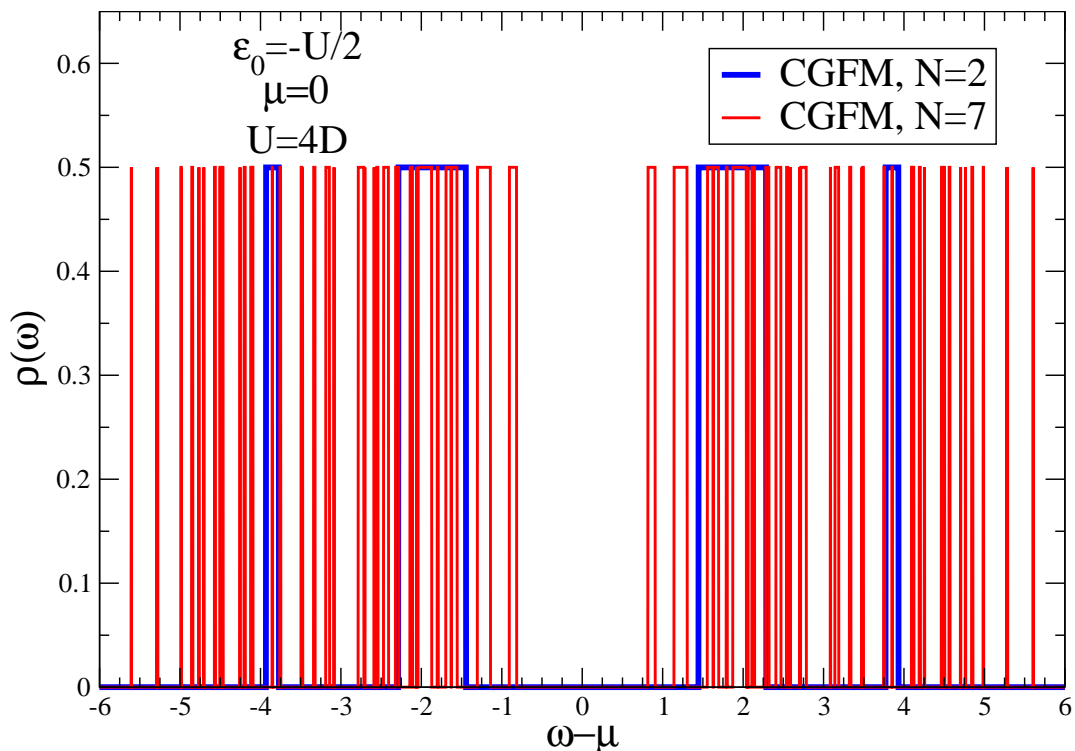


Figure 4.2: Density of states ρ as a function of the frequency $\omega - \mu$ for the half-filling limit, $\epsilon_0 = -U/2$, $\mu = 0$, for the CGFM for some representative values of $N = 2, 7$.

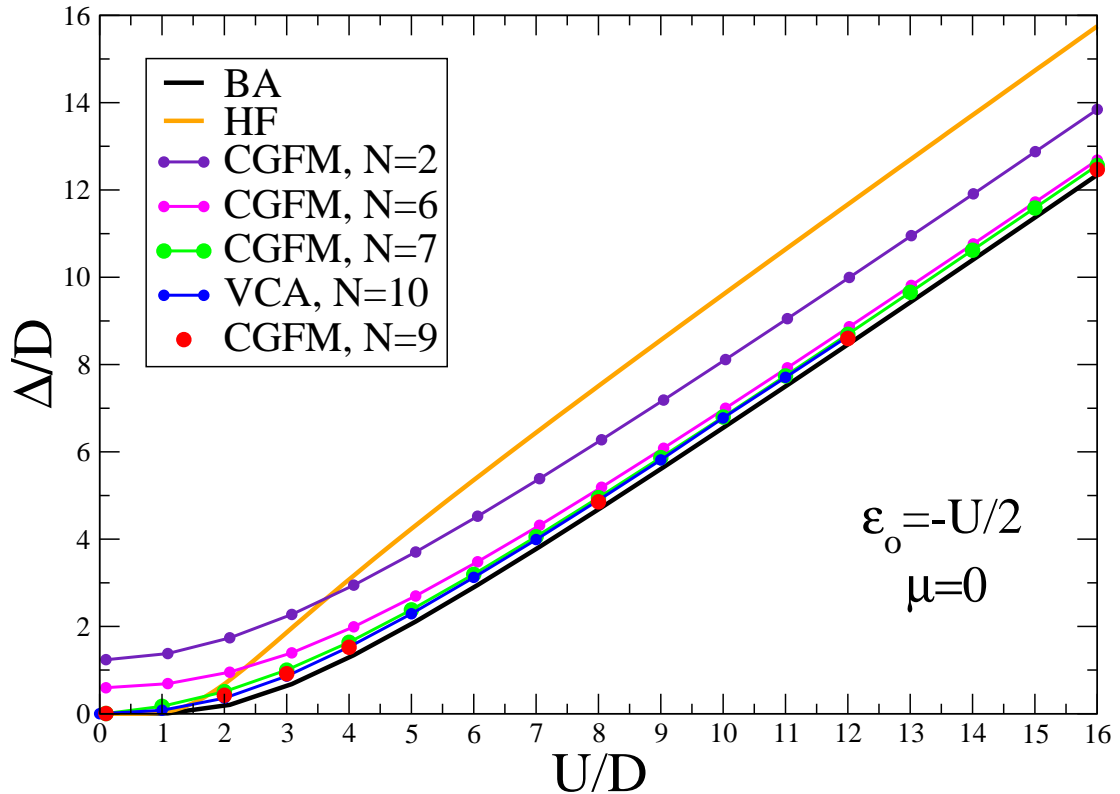


Figure 4.3: Single-particle gap Δ as a function of the correlation energy U for the BA, the HF approximation, the VCA [2], and the CGFM for some representative values of $N = 2, 6, 7, 9$.

In figure 4.2, we plot the DOS as a function of the frequency $\omega - \mu$ for the half-filling limit, $\epsilon_0 = -U/2$, $\mu = 0$, and $N = 2$ and $N = 7$. The figure presents a discontinuous shape, with regions of different widths separated by gaps, which is a consequence of the atomic cluster employed as a “seed” to calculate the density of states of the lattice. As the size of the cluster increases, the DOS tends to become denser and fills all the gaps for N sufficiently large. The gap decreases as the cluster size increases and tends to the BA exact result as indicated in Figs. 4.3 and 4.4. It is also worth noting that the particle-hole symmetry is fulfilled for all values of N .

In Fig. 4.3 we present the gap Δ in the DOS at half-filling, $\epsilon_0 = -U/2$, $\mu = 0$, for different cluster sizes, as a function of the electronic correlation U . The exact BA results, eq. (2.72), show that there is no gap for $U = 0$, which is a requirement not satisfied by even N , as indicated in the figure for $N = 2, 6$. However, this requirement is satisfied for odd N , as indicated in the figure for $N = 7, 9$. The results of the CGFM are consistent with other ED approaches [2] (see the one referred to as the direct approach) and much better than the Hartree Fock [HF] approximation. As the cluster size increases, the gap gets closer to the BA. We also include in the figure, for the sake of comparison, the result of the variational cluster approach [VCA] [2] for $N = 10$ sites. The results obtained by the VCA for a chain containing $N = 10$ sites almost agree with the corresponding $N = 7$ CGFM and entirely agree with the $N = 9$ CGFM. However, a good workstation runs the CGFM code in a reasonable time for $N = 7$ or $N = 8$, whereas the VCA needs more computational power due to the self-consistent calculation for the hopping embodied in the method.

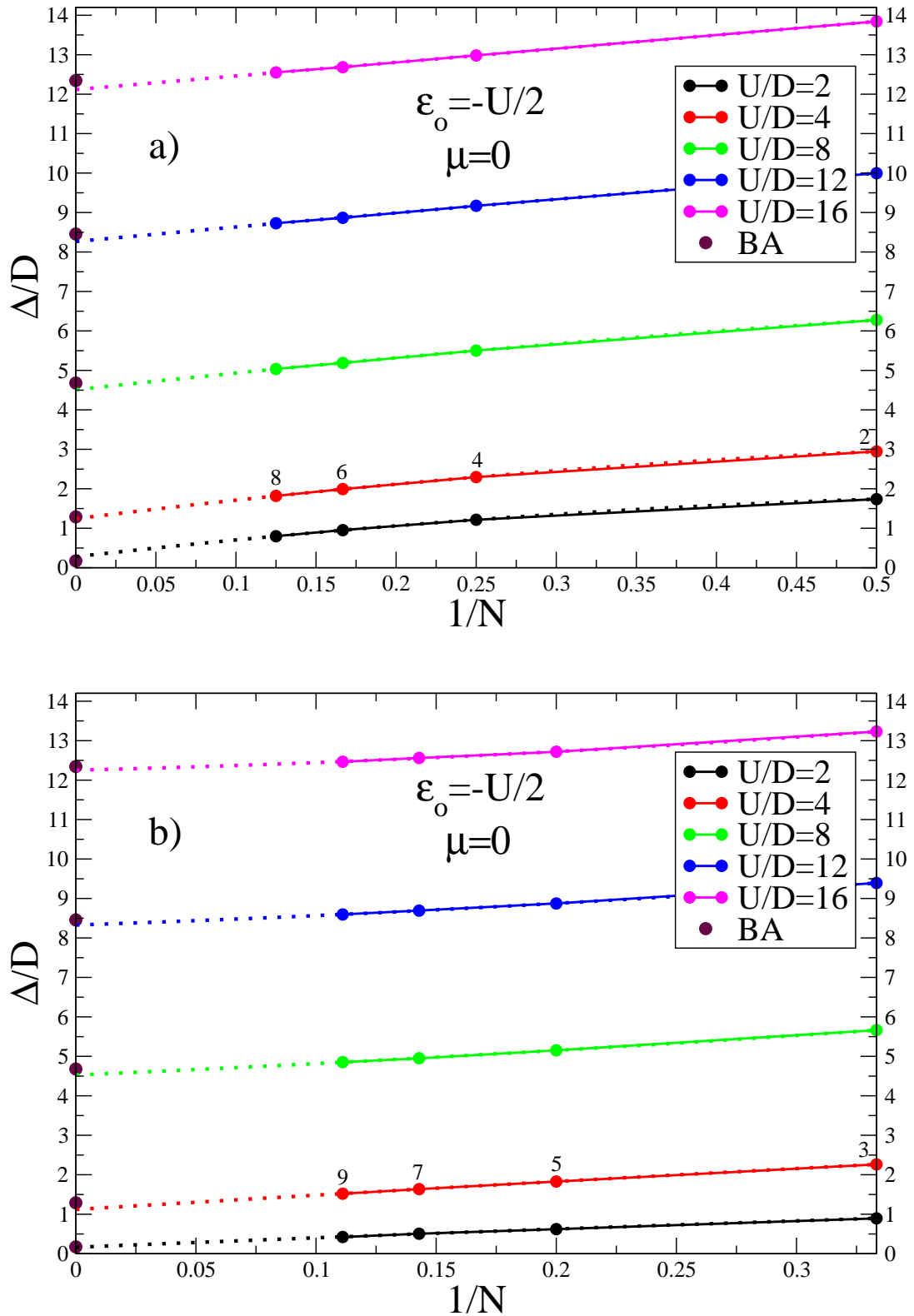


Figure 4.4: Single-particle gap Δ as a function of the inverse cluster size $1/N$ for the CGFM for a) Even N (2, 4, 6, 8) and b) Odd N (3, 5, 7, 9) for several values of electronic correlation U . The dotted lines represent the quadratic regression of the calculated data points and converge to the exact BA results represented by brown points on the vertical axis.

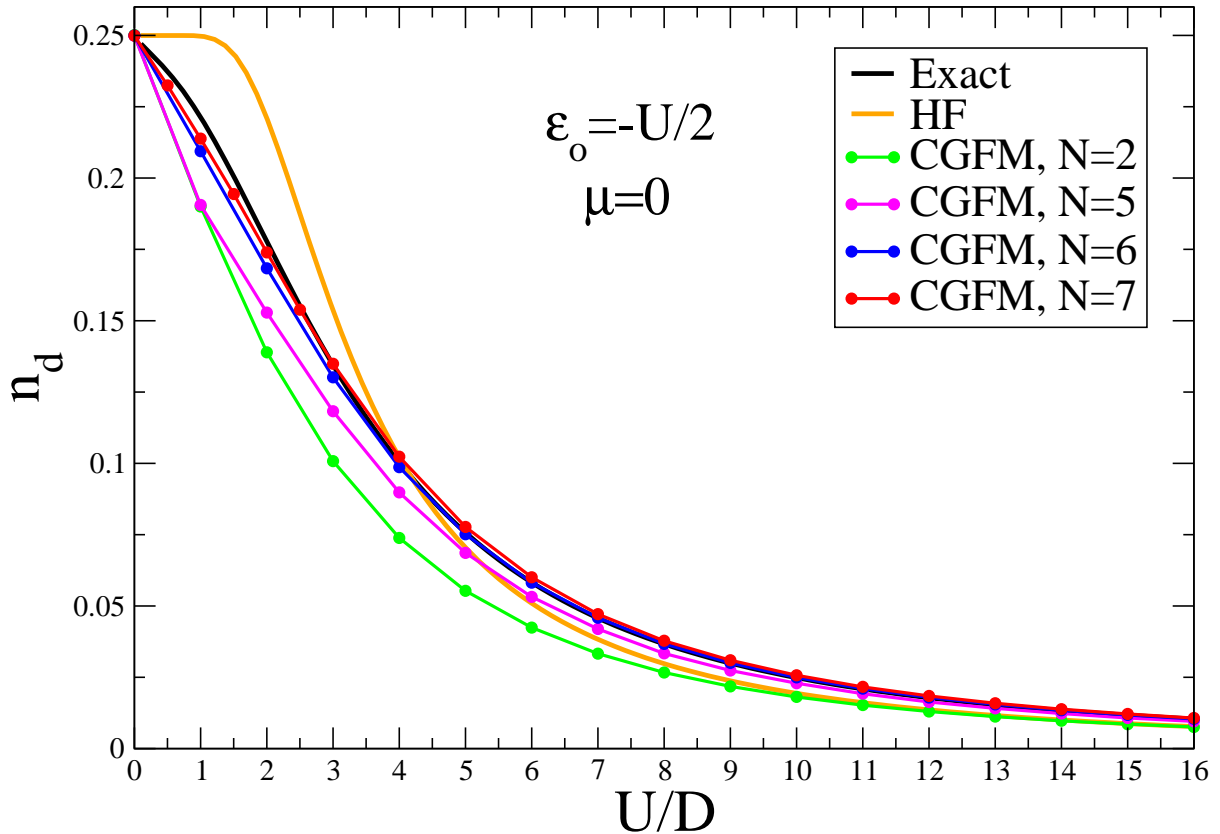


Figure 4.5: Double occupation number n_d as a function of the correlation U for the interpolative “exact” result [3], the HF approximation, and the CGFM for some representative values of $N = 2, 5, 6, 7$.

In Figs. 4.4 a), b) we plot the single-particle gap as a function of the inverse cluster size, $1/N$, for even and odd values of N for half-filling, $\epsilon_0 = -U/2$, $\mu = 0$. Since the results present a change in curvature as a function of $1/N$, as indicated in both figures, we performed a quadratic regression to obtain the converged values. The figures indicate that the gap obtained from even or odd N , by increasing the atomic cluster size, converge well to the exact BA result represented in the vertical axis by brown points. The results for the gap for large cluster sizes tend to be insensitive to even or odd N . On the other hand, for other properties of the model associated with the external magnetic field, the results of odd clusters present some unexpected effects that will be discussed in section 4.2.

Figure 4.5 shows the double occupation number n_d as a function of the correlation U for an interpolative “exact” result obtained by the formula, eq. (2.73) [3]; the HF approximation and the CGFM with $N = 2, 5, 6, 7$ for the half-filled limit, $\epsilon_0 = -U/2$, $\mu = 0$. The mean-field HF results do not agree well with the interpolative “exact” result. However, we include it here only to call the attention that the CGFM, contrary to HF, goes to the interpolative result as the number of the correlated sites inside the cluster increases. The CGFM results show that the $N = 7$ curve agrees well with the interpolative curve, and only for small U they present a slight deviation. To gather a more precise result in this region, we need to employ the calculations for larger clusters.

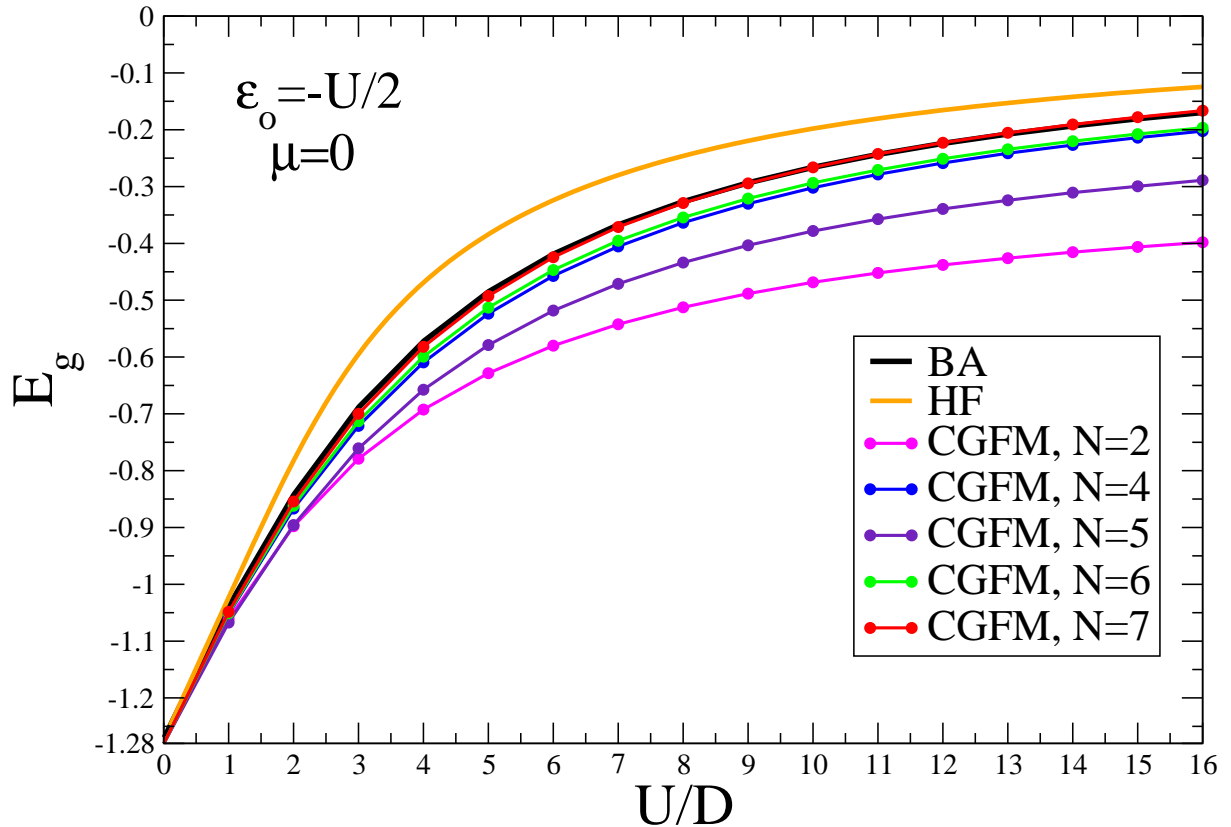


Figure 4.6: Ground-state energy for the lattice E_g as a function of the correlation U for the BA, the HF approximation, and the CGFM for some representative values of $N = 2, 4, 5, 6, 7$.

Employing the results for n_d for different values of U and using eq. (3.49) we calculate the ground-state energy for the lattice E_g as a function of U , as plotted in Fig. 4.6. The exact result is known from the Bethe ansatz formulation, and it was obtained using eq. (2.71). The HF result systematically deviates from the exact result and only agrees at small values of U . On the other hand, the CGFM for $N = 2, 4, 5, 6, 7$ approaches the exact result as N increases, and for $N = 7$, the agreement with the Bethe ansatz is exceptional. We conclude that the CGFM for $N = 7$ or even $N = 8$ constitutes a reliable and easy method to treat the one-dimensional Hubbard model. Even if it is possible to improve the results using clusters with $N > 7, 8$, the computational efforts become increasingly high, and for applications to the one-dimensional Hubbard model, like in quantum dot systems [57], the $N = 7, 8$ CGFM constitutes a good way to take into account the strong correlations in a systematic way.

In Fig. 4.7 we plot the occupation numbers as functions of the chemical potential μ considering the atomic cluster with $N = 7$ correlated sites and the correlation energy $U = 4D$. One of the strengths of the CGFM is to discriminate the partial occupation numbers for each spin. We can follow their behaviour as the chemical potential goes from small to large occupation density n , which allows a detailed study of the phase transitions present in the model. The figure shows that the completeness relation per spin, eq. (3.31), is satisfied for any value of the chemical potential μ .

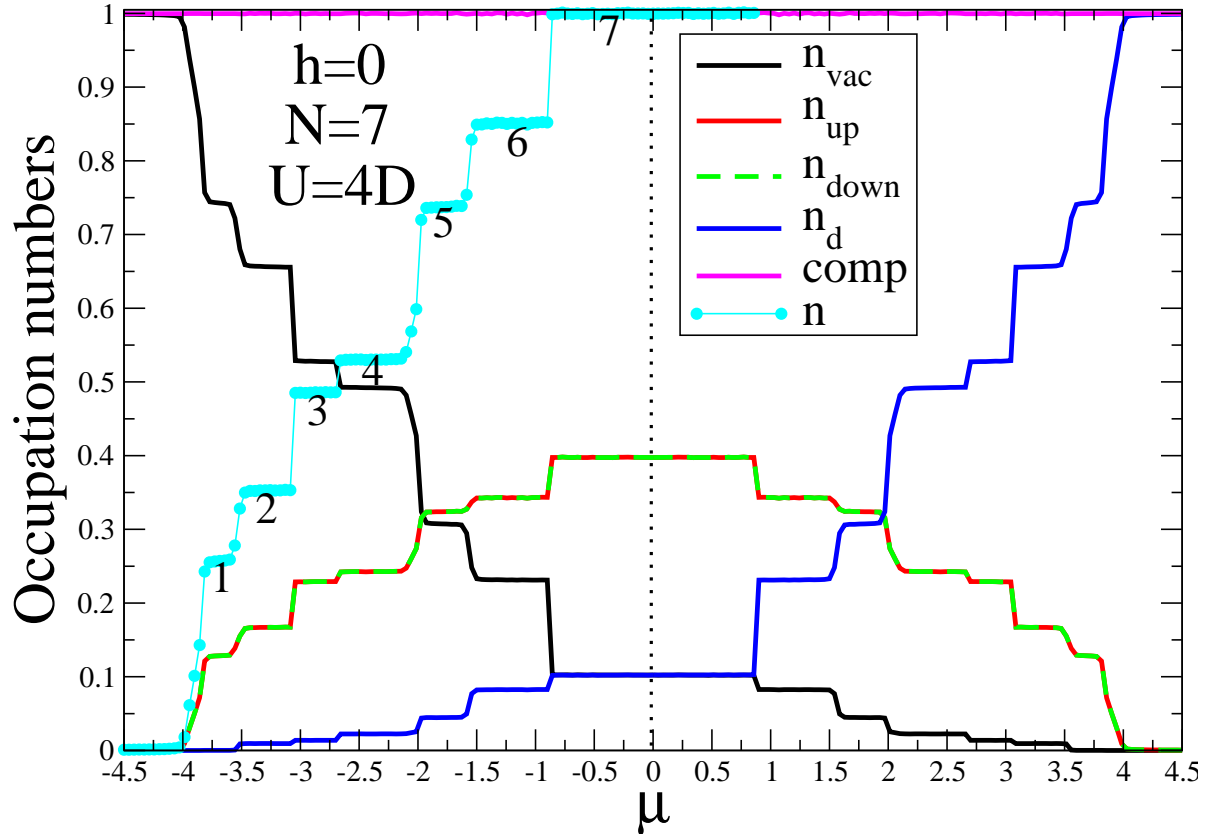


Figure 4.7: Occupation numbers as functions of the chemical potential μ for the CGFM with $U = 4D$, $N = 7$, magnetic field $h = 0$, and $T = 0.0001D$.

Table 4.2: Spin in the z direction S_z , and charge \mathcal{Q} of the atomic cluster ground-state in different regions as the chemical potential μ increases.

Region	μ	S_z	\mathcal{Q}
1	-3.70	$\pm 1/2$	1
2	-3.27	0	2
3	-2.90	$\pm 1/2$	3
4	-2.40	0	4
5	-1.75	$\pm 1/2$	5
6	-1.15	0	6
7	-0.40	$\pm 1/2$	7

Starting from the left of the figure, the vacuum occupation number per spin $n_{\text{vac}} = 1.0$, indicating that the system has no electrons, and as μ increases, it goes to zero on the right. The spin up and down occupation numbers n_{up} and n_{down} start at zero, go to a constant value at the center, and then decrease to zero as the system gets entirely doubly populated, $n_{\text{d}} = 1.0$. The discontinuous jumps in the curves are consequences of a strong finite-size effect associated with the discontinuous change of the ground-state of

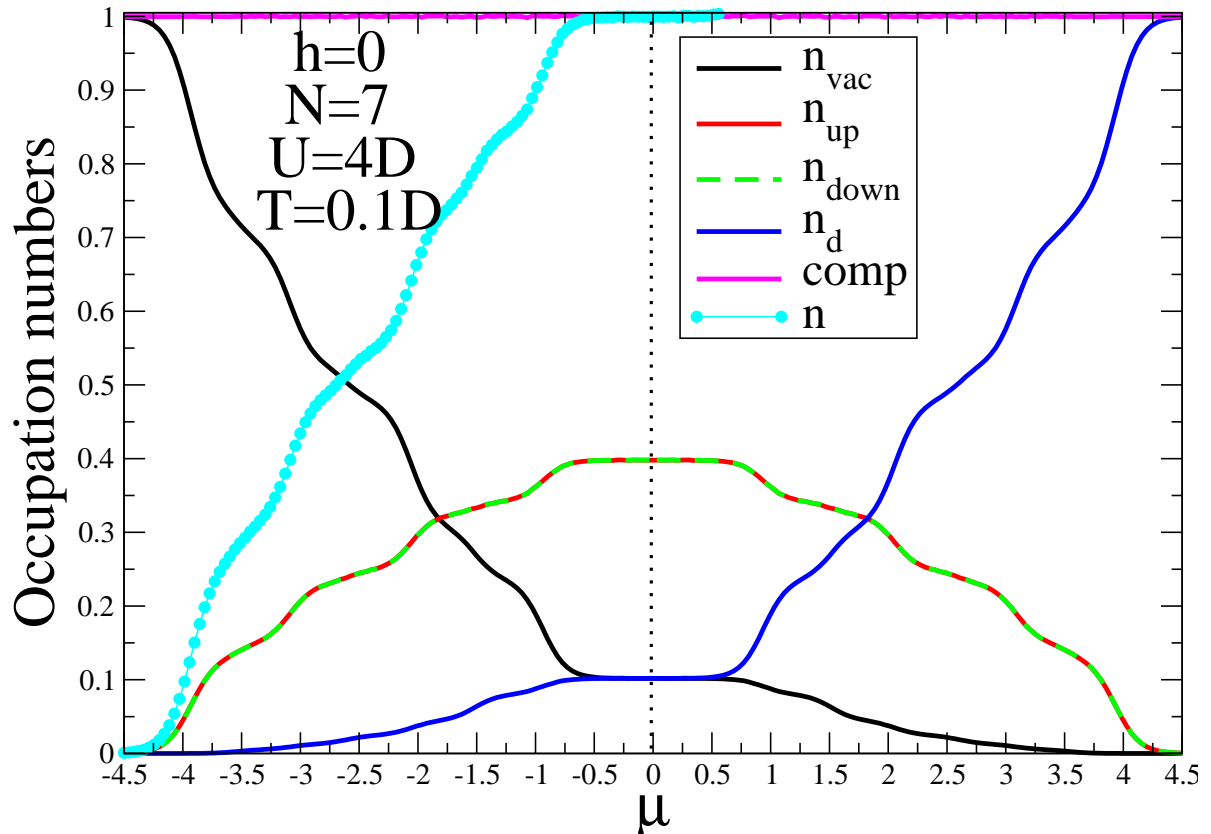


Figure 4.8: Occupation numbers as functions of the chemical potential μ for the CGFM with $U = 4D$, $N = 7$, magnetic field $h = 0$, and $T = 0.1D$.

the cluster which implies a discontinuous change of the cluster Green's functions and thus of the Green's functions for the lattice used to calculate the occupation numbers. In Table 4.2, we show the spin S_z and the charge Q of the cluster ground-state containing $N = 7$ for representative values of μ employed in the calculation of the occupation numbers of Fig. 4.7. The ground-state of the cluster alternates between states with $S_z = \pm 1/2$ and $S_z = 0$ with charge starting from $Q = 1$ on the left, increasing one unit in each jump, and reaching $Q = N = 7$ at the center of the figure (half-filled case). It is also possible to see several flat regions, numbered from 1 to 6, where the occupation numbers do not vary with μ , and the system behaves as an insulator. They constitute unphysical results and are consequences of the small cluster employed in the calculation. For larger clusters, those insulator regions tend to disappear [24]. The central region, labeled by the number 7 is a physical result that defines a Mott insulator [8, 16].

In Fig. 4.8 we plot the occupation numbers as functions of the chemical potential μ considering the atomic cluster with $N = 7$ correlated sites, the correlation energy $U = 4D$, and the temperature $T = 0.1D$. The general behaviour of the occupation numbers is the same as in figure 4.7. However, it can be seen that the curves are less step-like compared to the result for very low temperatures, where not every transition that satisfies the selection rules will happen, because some of them would require a large amount of energy to move the electron from the ground-state. As the temperature increases, the amount of thermal energy in the system facilitates transitions that would not be possible for low temperatures and the number of transitions increases significantly, smoothing the resulting occupation numbers.

4.2 Nonzero magnetic field

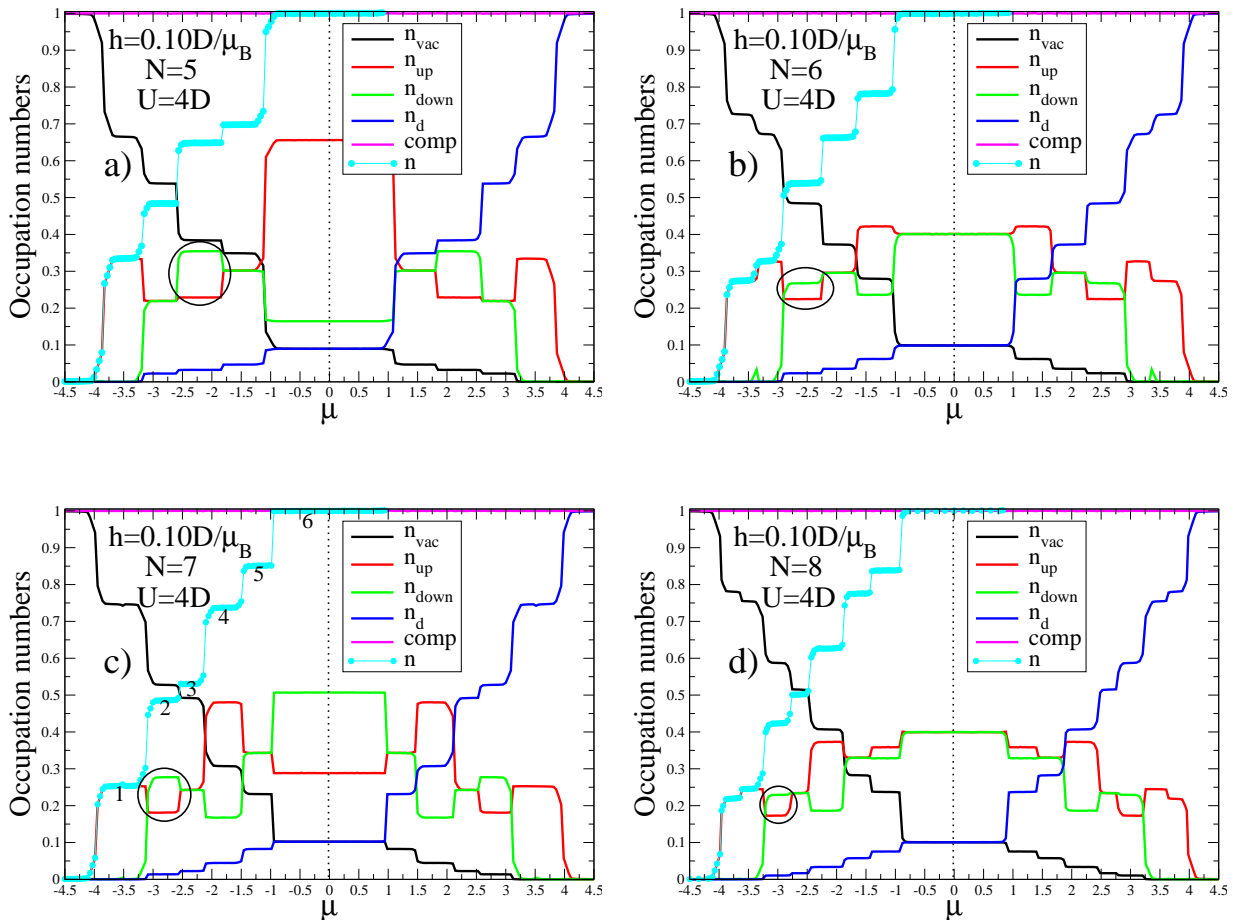


Figure 4.9: Occupation numbers as functions of the chemical potential μ for the CGFM with $U = 4D$; magnetic field $h = 0.10D/\mu_B$; and a) $N = 5$, b) $N = 6$, c) $N = 7$, d) $N = 8$.

In Figs. 4.9 a), b), c), d) we plot the occupation numbers as functions of the chemical potential μ for the CGFM with $U = 4D$; magnetic field $h = 0.10D/\mu_B$; and $N = 5, 6, 7, 8$. The discontinuous jumps in the curves are consequences of a strong finite-size effect, as discussed previously, but tend to disappear as the cluster size increases. The results for even and odd N are completely different near $\mu = 0$, and are associated with the total spin S_z of the ground-state of the cluster: for even N , $S_z = 0$, and for odd N , $S_z = \pm 1/2$. In the latter, a strong coupling between the spin of the cluster and the external magnetic field happens, but this does not happen for even N . As N increases, the solutions for both cases tend to the same result because the S_z of large odd size clusters tend to be shielded by the spin of other electrons present in the cluster, and the effective S_z decreases. The method reproduces all the phase transitions of the model, and the available computational resources establish the limit of the approximate solutions.

Fig. 4.9 c) also indicates regions where the ground-state of the cluster changes as a function of μ . Due to the action of the magnetic field h , there are regions where $S_z = \pm 1/2$ (regions 1, 2, 4, 6), and regions where $S_z = 0$ (regions 3, 5). In regions where $S_z = 0$, the n_{up} and n_{down} occupations are almost equal, but where $S_z = \pm 1/2$, in some regions $n_{up} > n_{down}$ and in others $n_{up} < n_{down}$. In regions 2, 6,

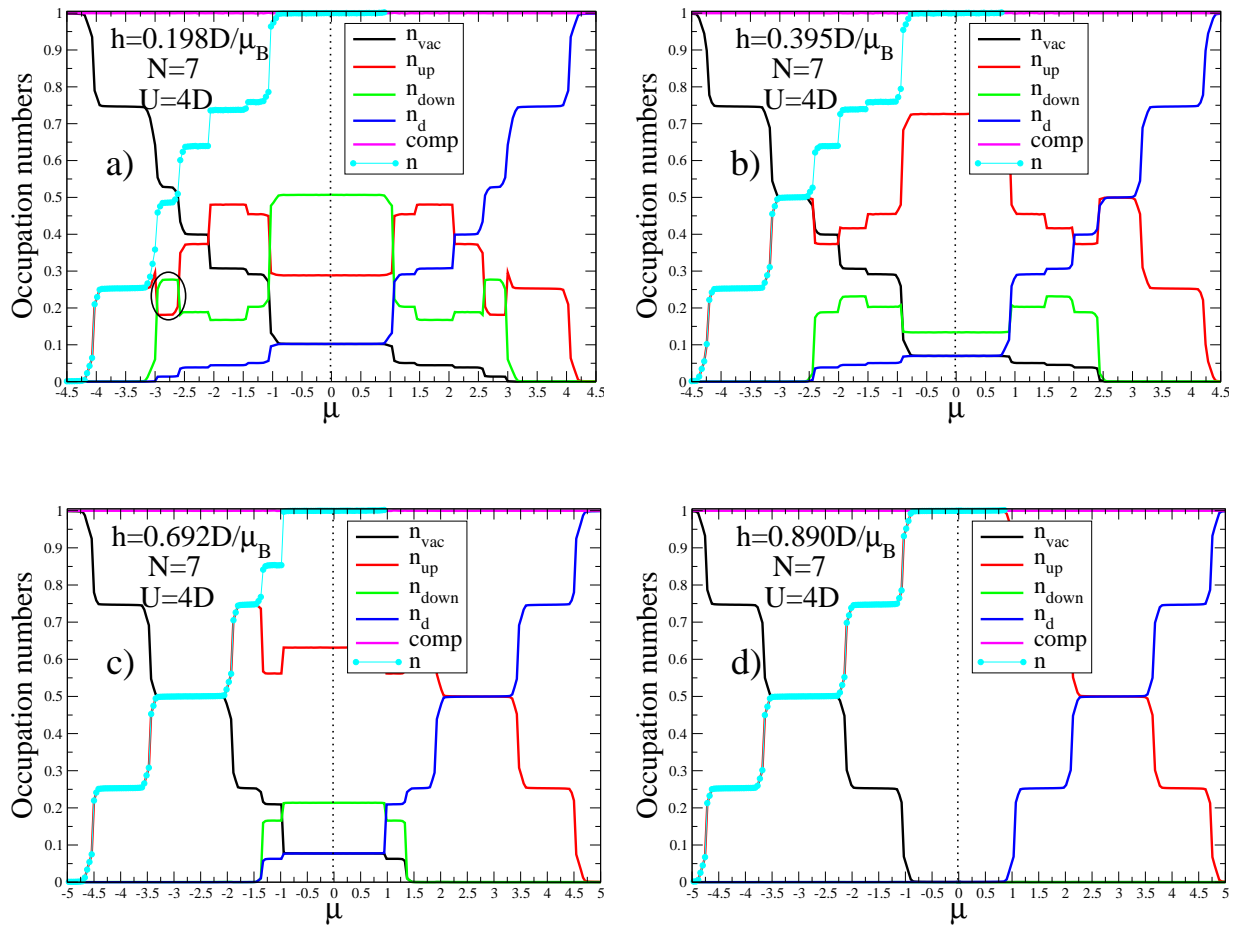


Figure 4.10: Occupation numbers as functions of the chemical potential μ for the CGFM with $U = 4D$; $N = 7$; and magnetic fields a) $h = 0.198D/\mu_B$, b) $h = 0.395D/\mu_B$, c) $h = 0.692D/\mu_B$, d) $h = 0.890D/\mu_B$.

$n_{up} < n_{down}$, which is an unexpected result once the magnetic field h tends to favour the n_{up} solution. In region 6, for $N = 5$, $n_{up} > n_{down}$; for $N = 7$, there is an inversion and $n_{up} < n_{down}$; and for $N = 9$ (we have calculated a single data point in this region, not shown), there is another inversion and $n_{up} > n_{down}$. Besides this, n_{up} and n_{down} become closer in region 6 as N increases for the odd cases. The low magnetic fields act in a non-uniform way as a function of the chemical potential, which leads to the generation of this new behaviour in the occupation numbers. We detect the same behaviour in all curves for $N = 5, 6, 7$. We associate to this behaviour a cluster phase that we call phase VI in the phase diagram that will be shown later, in which the band is partially filled and magnetized ($0 < n < 1$ and $m < 0$). However, this cluster phase should disappear for larger cluster sizes.

Figs. 4.10 a), b), c), d) show the occupation numbers as functions of the chemical potential μ for the CGFM with $U = 4D$; $N = 7$; and magnetic fields $h = 0.198D/\mu_B, 0.395D/\mu_B, 0.692D/\mu_B, 0.890D/\mu_B$. The cluster phase VI persists for $h = 0.198D/\mu_B$, in two regions: the small circled region and other large region at the center in Fig. 4.10 a). For intermediate to high magnetic fields, n_{up} is greater than n_{down} independently of μ . Other than that, the region where n_{down} is different from zero narrows and, eventually disappears, showing that the system goes under a transition.

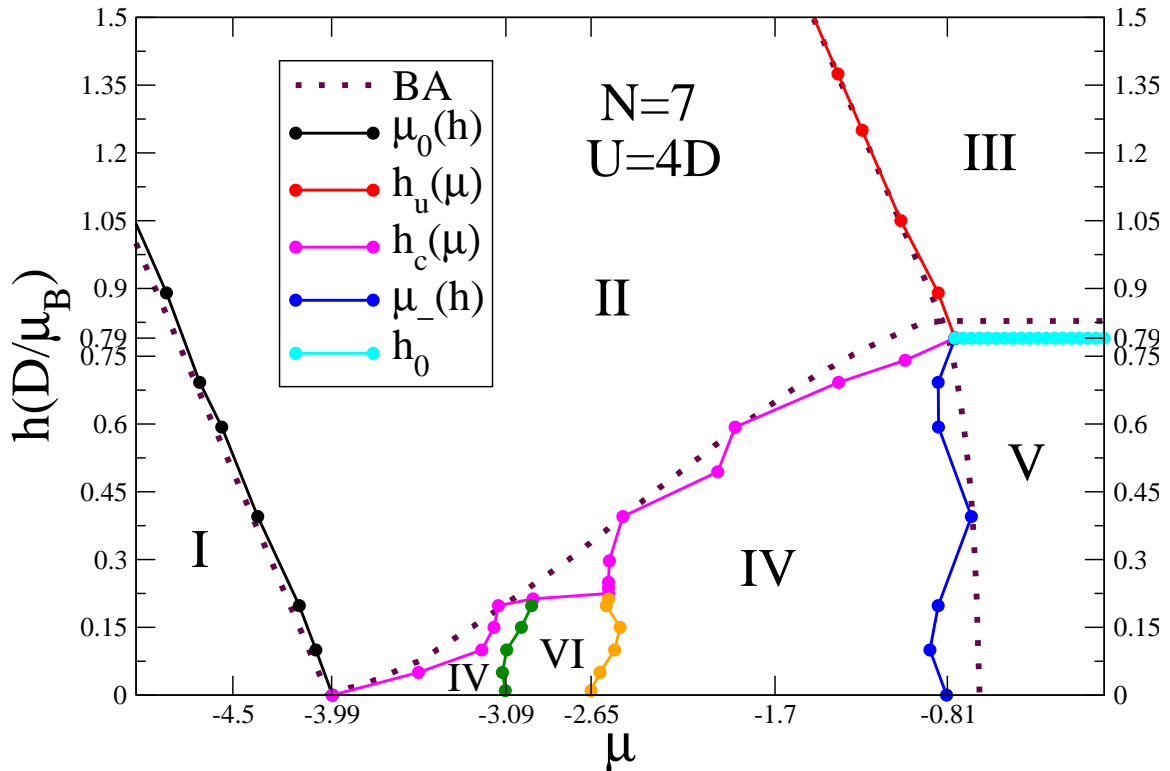


Figure 4.11: Ground-state phase diagram at low temperature in h vs. μ coordinates for the CGFM for $U = 4D$ and $N = 7$, and at zero temperature for the BA for $u = 1$. In terms of the densities and magnetization the six phases are characterized by I: $n = m = 0$; II: $n_{down} = 0, 0 < n_{up} < 1$; III: $n_{down} = 0, n_{up} = 1$; IV: $0 < n < 1, 0 \leq m \leq 1/2$; V: $n = 1, m \geq 0$; VI: $0 < n < 1, -1/2 \leq m \leq 0$.

The Hubbard model presents quantum phase transitions at zero temperature that were studied using the quantum transfer matrix formalism in reference [24]. The ground-state phase diagram in h vs. μ coordinates was studied in references [3,19,24] employing the thermodynamic Bethe ansatz and exhibits five phases that were discussed in section 2.3.2 of this thesis. Figs. 4.11 and 4.12 show the ground-state phase diagram in h vs. μ coordinates for $\mu < 0$ and $h > 0$ calculated by means of the CGFM for $U = 4D$, $N = 7$, and $N = 8$; and the TBA for $u = U/4t = 1$ (the cases for $\mu > 0$, $h < 0$, and other combinations are symmetrical). Regions I to VI are characterized by different values of the electron density per site n , partial occupation numbers n_{up} and n_{down} and magnetization m . The result of the boundary between phases I and II using the TBA is $\mu_0(h) = -2 - 2u - h$ [3,24]. For $h = 0$, $\mu_0(0) = -4.0$ and the results of the CGFM converge to this result as we increase the number of sites, being $\mu_0(0) = -3.99$ for $N = 7$, and $\mu_0(0) = -4.0$ for $N = 8$. In the same way, the result of the boundary between phases III and V using the TBA is $h_0 = 2(\sqrt{1+u^2}) - 2u = 0.828$ [3,24], and the corresponding results of the CGFM are, for $N = 7$, $h_0 = 0.79$ and, for $N = 8$, $h_0 = 0.8$. The boundary between phases IV and V using the TBA for $h = 0$ is given by $\mu_-(0) = -0.643$ [3,24], and the result of the CGFM for $N = 7$ is $\mu_-(0) = -0.81$ and for $N = 8$ is also $\mu_-(0) = -0.81$. The boundaries converge to the known results as we increase N and the phase diagrams exhibit the same shape, same phases, and agree well with the results obtained from methods such as the TBA and the QTM [3,21–25]. We can observe the following six different phases:

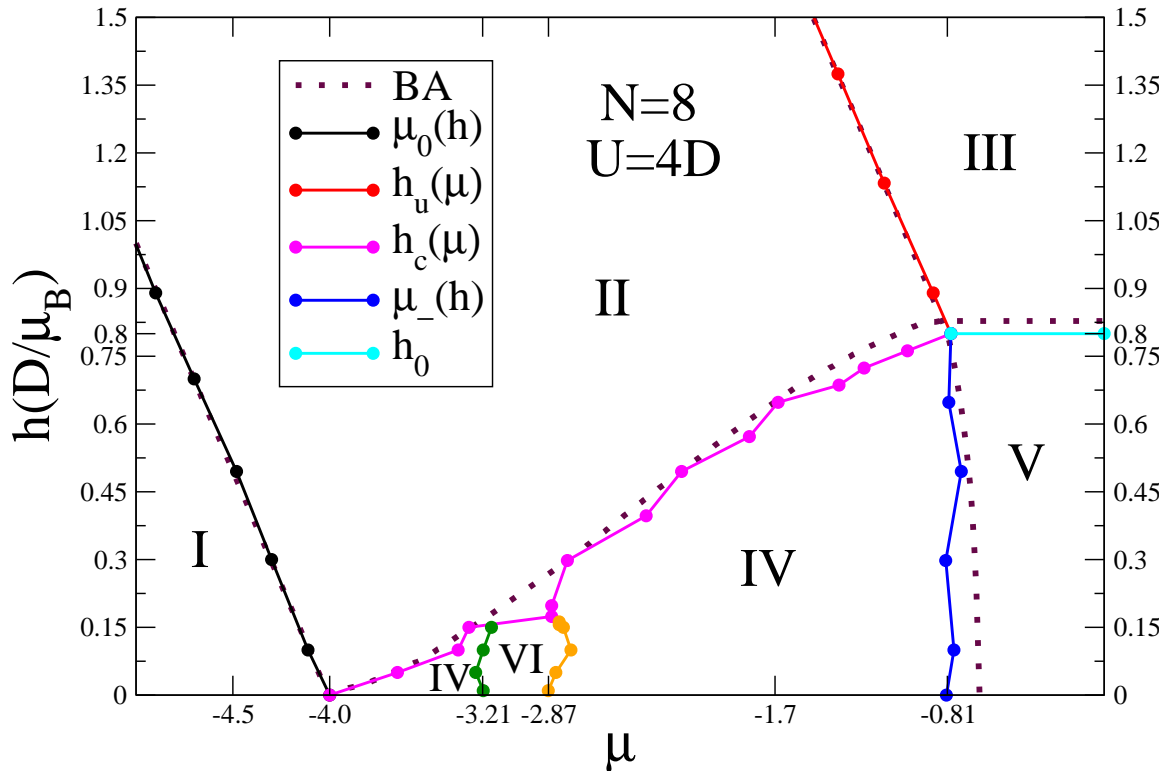


Figure 4.12: Ground-state phase diagram at low temperature in h vs. μ coordinates for the CGFM for $U = 4D$ and $N = 8$, and at zero temperature for the BA for $u = 1$. In terms of the densities and magnetization the six phases are characterized by I: $n = m = 0$; II: $n_{down} = 0, 0 < n_{up} < 1$; III: $n_{down} = 0, n_{up} = 1$; IV: $0 < n < 1, 0 \leq m \leq 1/2$; V: $n = 1, m \geq 0$; VI: $0 < n < 1, -1/2 \leq m \leq 0$.

- Phase I - Vacuum - $n = 0, n_{up} = 0, n_{down} = 0, m = 0$. This phase is characterized by zero occupation numbers. Both bands are empty and the ground-state is the empty lattice. Both electron density and magnetization are zero.
- Phase II - Partially filled and spin polarized band - $0 < n < 1, 0 < n_{up} < 1, n_{down} = 0, m = n/2$. The spin down band is empty and the spin up band is partially filled.
- Phase III - Half-filled and spin polarized band - $n = 1, n_{up} = 1, n_{down} = 0, m = 1/2$. The spin down band is empty and the spin up band is completely filled. The electron density is one and the magnetization is $1/2$.
- Phase IV - Partially filled and magnetized band - $0 < n < 1, 0 < n_{up} < 1, 0 < n_{down} < 1, 0 \leq m < n/2$. Both bands are partially filled. The electron density is between zero and one and the magnetization is between zero and $1/2$.
- Phase V - Half-filled and partially magnetized band - $n = 1, m \geq 0$. The system is half-filled. The electron density is one and the magnetization is greater than zero.
- Phase VI - Partially filled and magnetized band - $0 < n < 1, 0 < n_{up} < 1, 0 < n_{down} < 1, -n/2 \leq m < 0$. Both bands are partially filled. The electron density is between zero and one, and the magnetization is between $-1/2$ and zero. This phase is not present in the Bethe ansatz solution.

According to reference [24], the transitions from phases I to II, I to IV, II to IV, IV to V and III to V are quantum phase transitions and the boundaries between them can be associated with maxima of the grand-canonical specific heat c_v , but we can not study this aspect of the problem in this work. The main result obtained from the phase diagram is phase V, that, as discussed at the end of section 2.3.2 of this thesis, is the region where the one-dimensional Hubbard model reproduces the Mott insulator phase not present in the noninteracting case. Although the boundary between phases IV and V is not as close to the BA as the others and there is the anomalous region VI, which we believe is a cluster phase detected at low magnetic fields that should disappear for larger cluster sizes, the results agree very well with the phase diagram obtained using the TBA and we believe that it will improve even more for larger clusters or higher electronic correlation U .

4.3 A simple application

This section shows a simple application of the CGFM in spintronics. We study the electronic transport through a quantum wire [QW] described by correlated 3-site Hubbard rectangular conduction leads with an immersed correlated 3-site quantum dot [QD]. Fig. 4.13 shows a schematic view of of the setup [57]. When connected to Hubbard leads, the CGFM clusters can be used as correlated quantum dots to realize a single-electron transistor [SET]. The cluster can be viewed as a complex level structure that works as a QD. Using the gate voltage V_g we can tune the alignment of the different energy levels of the QD with the chemical potential μ to realize the polarization of the spin current that is established through the device by the voltage V_c . The coupling of the Hubbard leads to the QD is given by a hopping term V that transfers electrons from the leads in and out of the dot.

The local Green's function of the dot connected to the two 3-site Hubbard rectangular conduction leads is given by [58],

$$G_{\sigma}^{00}(\omega, T) = \frac{g_{QD}(\omega, T)}{1 - 2|V|^2 g_{QD}(\omega, T) G_{\sigma}(\omega, T)}, \quad (4.1)$$

where $g_{QD}(\omega, T)$ is given by eq. (3.7) and the leads Green's functions, $G_{\sigma}(\omega, T)$, by eqs. (3.19) and (3.24). The dimensionless conductance of the device can be calculated employing the standard relation [59]

$$G/G_0 = \int d\omega \left(-\frac{\partial f}{\partial \omega} \right) \mathcal{T}(\omega, T), \quad (4.2)$$

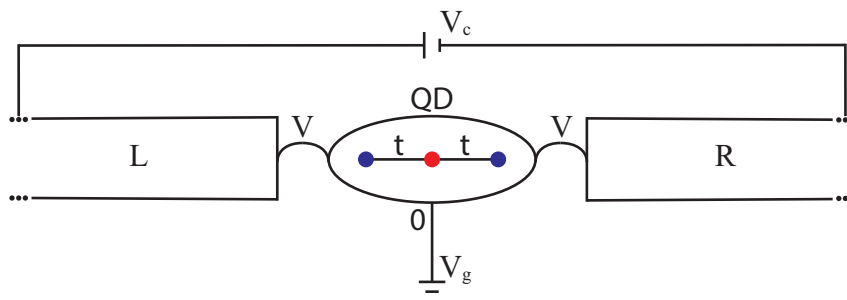


Figure 4.13: Schematic view of a correlated 3-site quantum dot immersed in left (L) and right (R) correlated 3-site Hubbard rectangular conduction bands.

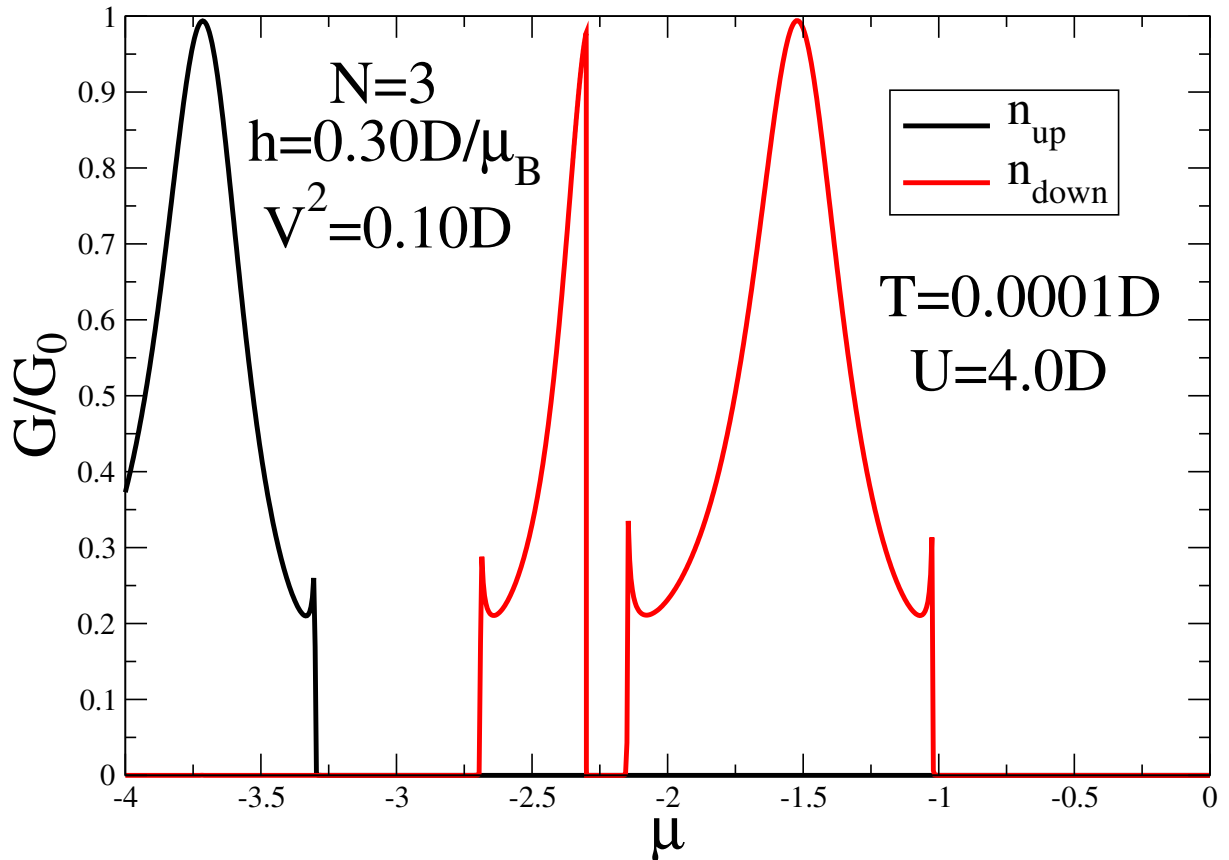


Figure 4.14: Electrical conductance G/G_0 vs. chemical potential μ .

where $G_0 = 2e^2/h$ is the quantum of conductance (taking spin into account), $f(\omega)$ is the Fermi-Dirac distribution and $\mathcal{T}(\omega, T) = \Gamma \text{Im}(G_\sigma^{00}(\omega, T))$ is the transmittance, with $\Gamma = 2|V|^2 \text{Im}(G_\sigma(\omega, T))$.

Fig. 4.14 shows the polarized G/G_0 vs. μ . For simplicity, we considered the trimer, $N = 3$, and the parameters employed in the calculation are: $T = 0.0001D$, $U = 4.0D$, $V^2 = 0.10D$, and the magnetic field $h = 0.30D/\mu_B$. There is a region, approximately in the interval $[0.29, 0.42]D/\mu_B$, where we have well-defined polarized spin currents; for other values of h , there are components of spin up and down currents corresponding to the same μ . Since these QDs interact strongly with an external magnetic field generating polarized spin regions as a function of μ , they can be valuable for applications in spintronics.

Chapter 5

Conclusions and Perspectives

We developed a method to solve the single-band Hubbard Hamiltonian employing cumulants to construct the Green's functions for the lattice, the CGFM. The method focuses on a cluster solution ("seed") employing exact diagonalization and can be extended to other strongly correlated systems: the Anderson, $t - J$, Kondo, and Coqblin-Schrieffer models. The method is sufficiently general to be applied to any parameter space of the model, and although the physics in this thesis did not go beyond known BA results, the method allows us to study problems in higher dimensions that BA can not tackle. One central point of the CGFM that differentiates it from other exact diagonalization approaches like the VCA [2, 44, 45] is the calculation of all atomic Green's functions employing the Lehmann representation. It constitutes the hard part of the method and allows the investigation of the relevant physical processes in each parameter space of the Hubbard model, providing clues to clarify the different ground-states present in the model.

The calculations of the method are direct and no self-consistent process is needed. We presented the mathematical derivation of the formalism and applied it to the single-band one-dimensional Hubbard Hamiltonian. We benchmarked the results from the CGFM against the results obtained with the thermodynamic Bethe ansatz and the quantum transfer matrix method [21–25]. We calculated the single-particle gap, ground-state energy, and occupation number density. Systematically, all results tend to be exact as the number of correlated sites N in the cluster increases. The precision of the approximations depends on the computational resources available. It is possible to run the CGFM code in a reasonable time for $N = 7$ or $N = 8$ using a good workstation, whereas more sites require heavy computation systems.

We recovered all five phases exhibited by the single-band one-dimensional Hubbard model in the presence of a magnetic field. We calculated the ground-state phase diagram in h vs. μ coordinates for $N = 7$ and $N = 8$ for $U = 4D$. Regions I to V are characterized by different electron density n , partial occupation numbers n_{up} and n_{down} and magnetization m , and agree well with the phase diagram obtained with the TBA. In addition to this, we identified a cluster phase (phase VI) that exists only for low magnetic fields and corresponds to a partially filled band $0 < n < 1$, but with $n_{down} > n_{up}$ and a negative magnetization $m < 0$. We identified the existence of this phase for $N = 5, 6, 7, 8$, but it must be a finite cluster size effect and should not survive for larger N . It deserves an additional check within other formalisms, like the TBA and QTM methods [21–25].

This work opens up a set of possibilities for future applications. In addition to a better understanding of the Hubbard model, its application in traditional systems where the model is believed to have a relevant role. As immediate applications of the method, we mention the use of the cluster solutions as a correlated quantum dot [QD] connected to Hubbard chains. This kind of setup can be used to study the Kondo effect [57] and different kinds of transport properties. We also presented a simple application of the CGFM in spintronics, where we studied the electronic transport through a 3-site cluster quantum dot [QD] immersed in correlated 3-site Hubbard rectangular conduction bands and obtained spin-polarized currents. The extension of the method to 2D and 3D opens the possibility of applying it to study high- T_C superconductivity [13] and the Mott transition. In applications to 2D or 3D systems, we must change the geometry of the correlated cluster to a closed one, as indicated in Fig. 3.2. Another promising application of the method is in the simulations of ultracold atoms in optical lattices. This research area has defined an ideal platform to verify and explore new physics associated with correlated electronic systems [35–37].

Bibliography

- [1] W. Metzner, “Linked-cluster expansion around the atomic limit of the hubbard model,” *Phys. Rev. B*, vol. 43, pp. 8549–8563, Apr 1991.
- [2] M. Balzer, W. Hanke, and M. Potthoff, “Mott transition in one dimension: Benchmarking dynamical cluster approaches,” *Phys. Rev. B*, vol. 77, p. 045133, Jan 2008.
- [3] F. H. L. Essler, H. Frahm, F. Gohmann, A. Klumper, and V. E. Korepin, *The One-Dimensional Hubbard Model*. Cambridge University Press, 2005.
- [4] M. C. Gutzwiller, “Effect of correlation on the ferromagnetism of transition metals,” *Phys. Rev. Lett.*, vol. 10, pp. 159–162, Mar 1963.
- [5] J. Kanamori, “Electron Correlation and Ferromagnetism of Transition Metals,” *Progress of Theoretical Physics*, vol. 30, pp. 275–289, 09 1963.
- [6] J. Hubbard, “Electron correlations in narrow energy bands,” *Proc. R. Soc. London, Ser. A*, vol. 276, no. 1365, pp. 238–257, 1963.
- [7] J. Hubbard, “Electron correlations in narrow energy bands. ii. the degenerate band case,” *Proc. R. Soc. London, Ser. A. Mathematical and Physical Sciences*, vol. 277, no. 1369, pp. 237–259, 1964.
- [8] J. Hubbard, “Electron correlations in narrow energy bands iii. an improved solution,” *Proc. R. Soc. London, Ser. A. Mathematical and Physical Sciences*, vol. 281, no. 1386, pp. 401–419, 1964.
- [9] J. Hubbard, “Electron correlations in narrow energy bands - iv. the atomic representation,” *Proc. R. Soc. London, Ser. A. Mathematical and Physical Sciences*, vol. 285, no. 1403, pp. 542–560, 1965.
- [10] J. Hubbard, “Electron correlations in narrow energy bands v. a perturbation expansion about the atomic limit,” *Proc. R. Soc. London, Ser. A. Mathematical and Physical Sciences*, vol. 296, no. 1444, pp. 82–99, 1967.
- [11] J. Hubbard, “Electron correlations in narrow energy bands vi. the connexion with many-body perturbation theory,” *Proc. R. Soc. London, Ser. A. Mathematical and Physical Sciences*, vol. 296, no. 1444, pp. 100–112, 1967.
- [12] D. P. Arovas, E. Berg, S. A. Kivelson, and S. Raghu, “The hubbard model,” *Annual Review of Condensed Matter Physics*, vol. 13, no. 1, p. null, 2022.

- [13] M. Qin, T. Schäfer, S. Andergassen, P. Corboz, and E. Gull, “The hubbard model: A computational perspective,” *Annual Review of Condensed Matter Physics*, vol. 13, no. 1, p. null, 2022.
- [14] E. H. Lieb and F. Y. Wu, “Absence of mott transition in an exact solution of the short-range, one-band model in one dimension,” *Phys. Rev. Lett.*, vol. 20, pp. 1445–1448, Jun 1968.
- [15] H. Bethe, “Zur theorie der metalle,” *Zeitschrift für Physik*, vol. 71, pp. 205–226, Mar 1931.
- [16] N. F. Mott, “The Basis of the Electron Theory of Metals, with Special Reference to the Transition Metals,” *Proceedings of the Physical Society A*, vol. 62, pp. 416–422, July 1949.
- [17] P. Schlottmann, “Metal-insulator transition in an one-dimensional hubbard-like model with degeneracy and crystalline field splitting,” *Journal of Magnetism and Magnetic Materials*, vol. 140-144, pp. 1615–1616, 1995. International Conference on Magnetism.
- [18] M. Takahashi, “One-Dimensional Hubbard Model at Finite Temperature: ,” *Progress of Theoretical Physics*, vol. 47, pp. 69–82, 01 1972.
- [19] M. Takahashi, “Low temperature specific heat of one dimensional hubbard model,” *Progress of Theoretical Physics*, vol. 52, pp. 103–114, 07 1974.
- [20] M. Takahashi, *Thermodynamics of One-Dimensional Solvable Models*. Cambridge University Press, 1999.
- [21] G. Juttner, A. Klumper, and J. Suzuki, “The hubbard chain at finite temperatures: ab initio calculations of tomonaga-luttinger liquid properties,” *Nuclear Physics B*, vol. 522, no. 3, p. 471, 1998.
- [22] M. Takahashi and M. Shiroishi, “Thermodynamic bethe ansatz equations of one-dimensional hubbard model and high-temperature expansion,” *Phys. Rev. B*, vol. 65, p. 165104, Apr 2002.
- [23] V. L. Campo, “Density-functional-theory approach to the thermodynamics of the harmonically confined one-dimensional hubbard model,” *Phys. Rev. A*, vol. 92, p. 013614, Jul 2015.
- [24] O. I. Pâțu, A. Klümper, and A. Foerster, “Quantum critical behavior and thermodynamics of the repulsive one-dimensional hubbard model in a magnetic field,” *Phys. Rev. B*, vol. 101, p. 035149, Jan 2020.
- [25] J. M. P. Carmelo, T. Čadež, and P. D. Sacramento, “One-particle spectral functions of the one-dimensional fermionic hubbard model with one fermion per site at zero and finite magnetic fields,” *Phys. Rev. B*, vol. 103, p. 195129, May 2021.
- [26] M. R. Hedayati and G. Vignale, “Ground-state energy of the one- and two-dimensional hubbard model calculated by the method of singwi, tosi, land, and sjölander,” *Phys. Rev. B*, vol. 40, pp. 9044–9051, Nov 1989.
- [27] M. Berciu and S. John, “Quantum dynamics of charged and neutral magnetic solitons: Spin-charge separation in the one-dimensional hubbard model,” *Phys. Rev. B*, vol. 61, p. 10015, Apr 2000.

- [28] A. Georges, G. Kotliar, W. Krauth, and M. J. Rozenberg, “Dynamical mean-field theory of strongly correlated fermion systems and the limit of infinite dimensions,” *Rev. Mod. Phys.*, vol. 68, pp. 13–125, Jan 1996.
- [29] G. Kotliar, S. Y. Savrasov, G. Pálsson, and G. Biroli, “Cellular dynamical mean field approach to strongly correlated systems,” *Phys. Rev. Lett.*, vol. 87, p. 186401, Oct 2001.
- [30] J. P. F. LeBlanc *et al.*, “Solutions of the two-dimensional hubbard model: Benchmarks and results from a wide range of numerical algorithms,” *Phys. Rev. X*, vol. 5, p. 041041, Dec 2015.
- [31] T. Maier, M. Jarrell, T. Pruschke, and M. H. Hettler, “Quantum cluster theories,” *Rev. Mod. Phys.*, vol. 77, pp. 1027–1080, Oct 2005.
- [32] T. Maier, M. Jarrell, T. Pruschke, and M. H. Hettler, “Quantum cluster theories,” *Reviews of Modern Physics*, vol. 77, pp. 1027–1080, oct 2005.
- [33] J. E. Hirsch and R. M. Fye, “Monte carlo method for magnetic impurities in metals,” *Phys. Rev. Lett.*, vol. 56, pp. 2521–2524, Jun 1986.
- [34] M. Jarrell, “Hubbard model in infinite dimensions: A quantum monte carlo study,” *Phys. Rev. Lett.*, vol. 69, pp. 168–171, Jul 1992.
- [35] T. Esslinger *Annu. Rev. Condens. Matter Phys.*, vol. 1, p. 129, 2010.
- [36] I. Bloch, J. Dalibard, and S. Nascimbéne *Nat. Phys.*, vol. 8, p. 267, 2012.
- [37] C. Gross and I. Bloch *Science*, vol. 357, p. 995, 2017.
- [38] R. Jördens, N. Strohmaier, K. Günter, H. Moritz, and T. Esslinger *Nature*, vol. 455, p. 204, 2008.
- [39] D. Greif, M. F. Parsons, A. Mazurenko, C. S. Chiu, S. Blatt, F. Huber, G. Ji, and M. Greiner *Science*, vol. 351, p. 953, 2016.
- [40] L. W. Cheuk, M. A. Nichols, K. R. Lawrence, M. Okan, H. Zhang, E. Khatami, N. Trivedi, T. Paiva, M. Rigol, and M. W. Zwierlein *Science*, vol. 353, p. 1260, 2016.
- [41] P. T. Brown, D. Mitra, E. Guardado-Sanchez, P. SchauSS, S. S. Kondov, E. Khatami, T. Paiva, N. Trivedi, D. A. Huse, and W. S. Bakr *Science*, vol. 357, p. 1385, 2017.
- [42] R. Senaratne, D. Cavazos-Cavazos, S. Wang, F. He, Y.-T. Chang, A. Kafle, H. Pu, X.-W. Guan, and R. G. Hulet *ArXiv:2111.11545*, 2021.
- [43] B. M. Spar, E. Guardado-Sanchez, S. Chi, Z. Z. Yan, and W. S. Bakr *ArXiv:2110.15398*, 2021.
- [44] E. V. Anda, G. Chiappe, C. A. Büsser, M. A. Davidovich, G. B. Martins, F. Heidrich-Meisner, and E. Dagotto, “Method to study highly correlated nanostructures: The logarithmic-discretization embedded-cluster approximation,” *Phys. Rev. B*, vol. 78, p. 085308, Aug 2008.

- [45] K. Seki, T. Shirakawa, and S. Yunoki, “Variational cluster approach to thermodynamic properties of interacting fermions at finite temperatures: A case study of the two-dimensional single-band hubbard model at half filling,” *Phys. Rev. B*, vol. 98, p. 205114, Nov 2018.
- [46] R. Lira, P. Riseborough, J. Silva-Valencia, and M. Figueira, “The cumulant Green’s functions method for the Hubbard model,” *arXiv:2205.01161*, 2022.
- [47] T. Lobo, M. S. Figueira, and M. E. Foglio, “The atomic approach to the Anderson model for the finite U case: application to a quantum dot,” *Nanotechnology*, vol. 21, p. 274007, jun 2010.
- [48] M. E. Foglio, T. Lobo, and M. S. Figueira, “Green’s Functions for the Anderson model: the Atomic Approximation,” 2010.
- [49] N. F. Mott, “The Basis of the Electron Theory of Metals, with Special Reference to the Transition Metals,” *Proceedings of the Physical Society A*, vol. 62, pp. 416–422, July 1949.
- [50] D. N. Zubarev, “Double-time Green functions in statistical physics,” *Soviet Physics Uspekhi*, vol. 3, pp. 320–345, mar 1960.
- [51] E. H. Lieb and F. Wu, “The one-dimensional hubbard model: a reminiscence,” *Physica A: Statistical Mechanics and its Applications*, vol. 321, no. 1, pp. 1–27, 2003. Statphys-Taiwan-2002: Lattice Models and Complex Systems.
- [52] A. A. Ovchinnikov, “Excitation Spectrum in the One-dimensional Hubbard Model,” *Soviet Journal of Experimental and Theoretical Physics*, vol. 30, p. 1160, Jan. 1969.
- [53] D. Baeriswyl and W. Von der Linden, “The hubbard model: From small to large u,” *International Journal of Modern Physics B*, vol. 05, no. 06n07, pp. 999–1014, 1991.
- [54] L. Craco and M. A. Gusmão, “From the atomic limit to a metal-insulator transition in the hubbard model,” *Phys. Rev. B*, vol. 52, pp. 17135–17142, Dec 1995.
- [55] M. R. Hedayati and G. Vignale, “Ground-state energy of the one- and two-dimensional Hubbard model calculated by the method of Singwi, Tosi, Land, and Sjölander,” *Phys. Rev. B*, vol. 40, pp. 9044–9051, Nov. 1989.
- [56] H. Tasaki, “The hubbard model - an introduction and selected rigorous results,” *Journal of Physics: Condensed Matter*, vol. 10, pp. 4353–4378, may 1998.
- [57] H. Bragança, M. F. Cavalcante, R. G. Pereira, and M. C. O. Aguiar, “Quench dynamics and relaxation of a spin coupled to interacting leads,” *Phys. Rev. B*, vol. 103, p. 125152, Mar 2021.
- [58] M. M. Odashima, B. G. Prado, and E. Vernek, “Pedagogical introduction to equilibrium Green’s functions: condensed-matter examples with numerical implementations,” *Rev. Bras. Ensino Física*, vol. 39, pp. 1–26, sep 2016.
- [59] B. Dong and X. L. Lei, “Effect of the kondo correlation on the thermopower in a quantum dot,” *Journal of Physics: Condensed Matter*, vol. 14, pp. 11747–11756, nov 2002.

Appendix A

Atomic Green's functions residues and transition energies for the dimer

Employing the spectral representation (Lehmann representation) [50], the Green's functions residues, given by equations (3.5) and (3.6) as

$$r_{i,\sigma} = [\exp(-\beta\varepsilon_{n-1,r}) + \exp(-\beta\varepsilon_{n,r'})] \times \langle n-1, r | c_{i\sigma} | n, r' \rangle \langle n, r' | c_{i\sigma}^\dagger | n-1, r \rangle, \quad (\text{A.1})$$

are, for the dimer:

$$\begin{aligned} r_1 &= \frac{1}{2}(e^{-\beta E_1} + e^{-\beta E_2}) + \frac{1}{2}(e^{-\beta E_1} + e^{-\beta E_3}) + \frac{1}{2}(e^{-\beta E_4} + e^{-\beta E_6}) + \frac{1}{4}(e^{-\beta E_4} + e^{-\beta E_8}) + \\ &\bullet \quad + \frac{1}{2}(e^{-\beta E_5} + e^{-\beta E_7}) + \frac{1}{4}(e^{-\beta E_5} + e^{-\beta E_8}) + \frac{1}{4}(e^{-\beta E_9} + e^{-\beta E_{14}}) + \frac{1}{4}(e^{-\beta E_9} + e^{-\beta E_{15}}); \\ r_2 &= \frac{1}{2}(e^{-\beta E_1} + e^{-\beta E_4}) + \frac{1}{2}(e^{-\beta E_1} + e^{-\beta E_5}) + \frac{1}{2}(e^{-\beta E_2} + e^{-\beta E_6}) + \frac{1}{4}(e^{-\beta E_2} + e^{-\beta E_8}) + \\ &\bullet \quad + \frac{1}{2}(e^{-\beta E_3} + e^{-\beta E_7}) + \frac{1}{4}(e^{-\beta E_3} + e^{-\beta E_8}) + \frac{1}{4}(e^{-\beta E_9} + e^{-\beta E_{12}}) + \frac{1}{4}(e^{-\beta E_9} + e^{-\beta E_{13}}); \\ r_3 &= \frac{1}{4}(e^{-\beta E_4} + e^{-\beta E_9}) + \frac{1}{4}(e^{-\beta E_5} + e^{-\beta E_9}) + \frac{1}{2}(e^{-\beta E_6} + e^{-\beta E_{14}}) + \frac{1}{2}(e^{-\beta E_7} + e^{-\beta E_{15}}) + \\ &\bullet \quad + \frac{1}{4}(e^{-\beta E_8} + e^{-\beta E_{14}}) + \frac{1}{4}(e^{-\beta E_8} + e^{-\beta E_{15}}) + \frac{1}{2}(e^{-\beta E_{12}} + e^{-\beta E_{16}}) + \frac{1}{2}(e^{-\beta E_{13}} + e^{-\beta E_{16}}); \\ r_4 &= \frac{1}{4}(e^{-\beta E_2} + e^{-\beta E_9}) + \frac{1}{4}(e^{-\beta E_3} + e^{-\beta E_9}) + \frac{1}{2}(e^{-\beta E_6} + e^{-\beta E_{12}}) + \frac{1}{2}(e^{-\beta E_7} + e^{-\beta E_{13}}) + \\ &\bullet \quad + \frac{1}{4}(e^{-\beta E_8} + e^{-\beta E_{12}}) + \frac{1}{4}(e^{-\beta E_8} + e^{-\beta E_{13}}) + \frac{1}{2}(e^{-\beta E_{14}} + e^{-\beta E_{16}}) + \frac{1}{2}(e^{-\beta E_{15}} + e^{-\beta E_{16}}); \\ r_5 &= 2 \left(\frac{1}{b\sqrt{2}} \right)^2 (e^{-\beta E_5} + e^{-\beta E_{10}}) + 2 \left(\frac{1}{b\sqrt{2}} \right)^2 (e^{-\beta E_4} + e^{-\beta E_{10}}) + \\ &\bullet \quad + 2 \left(\frac{4t}{b(c+U)\sqrt{2}} \right)^2 (e^{-\beta E_5} + e^{-\beta E_{10}}) + 2 \left(\frac{4t}{b(c+U)\sqrt{2}} \right)^2 (e^{-\beta E_4} + e^{-\beta E_{10}}) + \\ &\quad - 2 \left(\frac{1}{b\sqrt{2}} \frac{4t}{b(c+U)\sqrt{2}} \right) (e^{-\beta E_5} + e^{-\beta E_{10}}) + 2 \left(\frac{1}{b\sqrt{2}} \frac{4t}{b(c+U)\sqrt{2}} \right) (e^{-\beta E_4} + e^{-\beta E_{10}}); \end{aligned}$$

$$\begin{aligned}
r_6 &= 2 \left(\frac{1}{a\sqrt{2}} \right)^2 (e^{-\beta E_5} + e^{-\beta E_{11}}) + 2 \left(\frac{1}{a\sqrt{2}} \right)^2 (e^{-\beta E_4} + e^{-\beta E_{11}}) + \\
\bullet &+ 2 \left(\frac{4t}{a(c-U)\sqrt{2}} \right)^2 (e^{-\beta E_5} + e^{-\beta E_{11}}) + 2 \left(\frac{4t}{a(c-U)\sqrt{2}} \right)^2 (e^{-\beta E_4} + e^{-\beta E_{11}}) + \\
&+ 2 \left(\frac{1}{a\sqrt{2}} \frac{4t}{a(c-U)\sqrt{2}} \right) (e^{-\beta E_5} + e^{-\beta E_{11}}) - 2 \left(\frac{1}{a\sqrt{2}} \frac{4t}{a(c-U)\sqrt{2}} \right) (e^{-\beta E_4} + e^{-\beta E_{11}}); \\
r_7 &= 2 \left(\frac{1}{b\sqrt{2}} \right)^2 (e^{-\beta E_3} + e^{-\beta E_{10}}) + 2 \left(\frac{1}{b\sqrt{2}} \right)^2 (e^{-\beta E_2} + e^{-\beta E_{10}}) + \\
\bullet &+ 2 \left(\frac{4t}{b(c+U)\sqrt{2}} \right)^2 (e^{-\beta E_3} + e^{-\beta E_{10}}) + 2 \left(\frac{4t}{b(c+U)\sqrt{2}} \right)^2 (e^{-\beta E_2} + e^{-\beta E_{10}}) + \\
&+ 2 \left(\frac{1}{b\sqrt{2}} \frac{4t}{b(c+U)\sqrt{2}} \right) (e^{-\beta E_3} + e^{-\beta E_{10}}) - 2 \left(\frac{1}{b\sqrt{2}} \frac{4t}{b(c+U)\sqrt{2}} \right) (e^{-\beta E_2} + e^{-\beta E_{10}}); \\
r_8 &= 2 \left(\frac{1}{a\sqrt{2}} \right)^2 (e^{-\beta E_3} + e^{-\beta E_{11}}) + 2 \left(\frac{1}{a\sqrt{2}} \right)^2 (e^{-\beta E_2} + e^{-\beta E_{11}}) + \\
\bullet &+ 2 \left(\frac{4t}{a(c-U)\sqrt{2}} \right)^2 (e^{-\beta E_3} + e^{-\beta E_{11}}) + 2 \left(\frac{4t}{a(c-U)\sqrt{2}} \right)^2 (e^{-\beta E_2} + e^{-\beta E_{11}}) + \\
&- 2 \left(\frac{1}{a\sqrt{2}} \frac{4t}{a(c-U)\sqrt{2}} \right) (e^{-\beta E_3} + e^{-\beta E_{11}}) + 2 \left(\frac{1}{a\sqrt{2}} \frac{4t}{a(c-U)\sqrt{2}} \right) (e^{-\beta E_2} + e^{-\beta E_{11}}); \\
r_9 &= 2 \left(\frac{1}{b\sqrt{2}} \right)^2 (e^{-\beta E_{10}} + e^{-\beta E_{15}}) + 2 \left(\frac{1}{b\sqrt{2}} \right)^2 (e^{-\beta E_{10}} + e^{-\beta E_{14}}) + \\
\bullet &+ 2 \left(\frac{4t}{b(c+U)\sqrt{2}} \right)^2 (e^{-\beta E_{10}} + e^{-\beta E_{15}}) + 2 \left(\frac{4t}{b(c+U)\sqrt{2}} \right)^2 (e^{-\beta E_{10}} + e^{-\beta E_{14}}) + \\
&+ 2 \left(\frac{1}{b\sqrt{2}} \frac{4t}{b(c+U)\sqrt{2}} \right) (e^{-\beta E_{10}} + e^{-\beta E_{15}}) - 2 \left(\frac{1}{b\sqrt{2}} \frac{4t}{b(c+U)\sqrt{2}} \right) (e^{-\beta E_{10}} + e^{-\beta E_{14}}); \\
r_{10} &= 2 \left(\frac{1}{a\sqrt{2}} \right)^2 (e^{-\beta E_{11}} + e^{-\beta E_{15}}) + 2 \left(\frac{1}{a\sqrt{2}} \right)^2 (e^{-\beta E_{11}} + e^{-\beta E_{14}}) + \\
\bullet &+ 2 \left(\frac{4t}{a(c-U)\sqrt{2}} \right)^2 (e^{-\beta E_{11}} + e^{-\beta E_{15}}) + 2 \left(\frac{4t}{a(c-U)\sqrt{2}} \right)^2 (e^{-\beta E_{11}} + e^{-\beta E_{14}}) + \\
&- 2 \left(\frac{1}{a\sqrt{2}} \frac{4t}{a(c-U)\sqrt{2}} \right) (e^{-\beta E_{11}} + e^{-\beta E_{15}}) + 2 \left(\frac{1}{a\sqrt{2}} \frac{4t}{a(c-U)\sqrt{2}} \right) (e^{-\beta E_{11}} + e^{-\beta E_{14}}); \\
r_{11} &= 2 \left(\frac{1}{b\sqrt{2}} \right)^2 (e^{-\beta E_{10}} + e^{-\beta E_{13}}) + 2 \left(\frac{1}{b\sqrt{2}} \right)^2 (e^{-\beta E_{10}} + e^{-\beta E_{12}}) + \\
\bullet &+ 2 \left(\frac{4t}{b(c+U)\sqrt{2}} \right)^2 (e^{-\beta E_{10}} + e^{-\beta E_{13}}) + 2 \left(\frac{4t}{b(c+U)\sqrt{2}} \right)^2 (e^{-\beta E_{10}} + e^{-\beta E_{12}}) + \\
&- 2 \left(\frac{1}{b\sqrt{2}} \frac{4t}{b(c+U)\sqrt{2}} \right) (e^{-\beta E_{10}} + e^{-\beta E_{13}}) + 2 \left(\frac{1}{b\sqrt{2}} \frac{4t}{b(c+U)\sqrt{2}} \right) (e^{-\beta E_{10}} + e^{-\beta E_{12}}); \\
r_{12} &= 2 \left(\frac{1}{a\sqrt{2}} \right)^2 (e^{-\beta E_{11}} + e^{-\beta E_{13}}) + 2 \left(\frac{1}{a\sqrt{2}} \right)^2 (e^{-\beta E_{11}} + e^{-\beta E_{12}}) + \\
\bullet &+ 2 \left(\frac{4t}{a(c-U)\sqrt{2}} \right)^2 (e^{-\beta E_{11}} + e^{-\beta E_{13}}) + 2 \left(\frac{4t}{a(c-U)\sqrt{2}} \right)^2 (e^{-\beta E_{11}} + e^{-\beta E_{12}}) + \\
&+ 2 \left(\frac{1}{a\sqrt{2}} \frac{4t}{a(c-U)\sqrt{2}} \right) (e^{-\beta E_{11}} + e^{-\beta E_{13}}) - 2 \left(\frac{1}{a\sqrt{2}} \frac{4t}{a(c-U)\sqrt{2}} \right) (e^{-\beta E_{11}} + e^{-\beta E_{12}}).
\end{aligned}$$

Table A.1: Energy differences of the possible transitions of the Hubbard dimer.

Energy differences	Transitions
$u_1 = \epsilon_0 + t$	$E_{1,2} = E_{1,3} = E_{4,6} = E_{4,8} = E_{5,7} = E_{5,8} = E_{9,14} = E_{9,15}$
$u_2 = \epsilon_0 - t$	$E_{1,4} = E_{1,5} = E_{2,6} = E_{2,8} = E_{3,7} = E_{3,8} = E_{9,12} = E_{9,13}$
$u_3 = \epsilon_0 + t + U$	$E_{4,9} = E_{5,9} = E_{6,14} = E_{7,15} = E_{8,14} = E_{8,15} = E_{12,16} = E_{13,16}$
$u_4 = \epsilon_0 - t + U$	$E_{2,9} = E_{3,9} = E_{6,12} = E_{7,13} = E_{8,12} = E_{8,13} = E_{14,16} = E_{15,16}$
$u_5 = \epsilon_0 + t + \frac{U+c}{2}$	$E_{4,10} = E_{5,10}$
$u_6 = \epsilon_0 + t + \frac{U-c}{2}$	$E_{4,11} = E_{5,11}$
$u_7 = \epsilon_0 - t + \frac{U+c}{2}$	$E_{2,10} = E_{3,10}$
$u_8 = \epsilon_0 - t + \frac{U-c}{2}$	$E_{2,11} = E_{3,11}$
$u_9 = \epsilon_0 + t + U - \frac{U+c}{2}$	$E_{10,14} = E_{10,15}$
$u_{10} = \epsilon_0 + t + U - \frac{U-c}{2}$	$E_{11,14} = E_{11,15}$
$u_{11} = \epsilon_0 - t + U - \frac{U+c}{2}$	$E_{10,12} = E_{10,13}$
$u_{12} = \epsilon_0 - t + U - \frac{U-c}{2}$	$E_{11,12} = E_{11,13}$

Energy differences of possible transitions in the Hubbard dimer, where $E_{i,j}$ represents the transition from the state i to the state j .

Also using equations (3.5) and (3.6), the energy differences for the possible transitions, given as

$$u_{i,\sigma} = \varepsilon_{n-1,r} - \varepsilon_{n,r'}, \quad (\text{A.2})$$

are, for the dimer, the results presented in table A.1.